

Characterizing and Identifying single Molecules by Scanning Probe Microscopy using Functionalized Tips



Dissertation

zur Erlangung des Doktorgrades
der Naturwissenschaften (Dr. rer. nat.)
der Fakultät für Physik
der Universität Regensburg

vorgelegt von
Bruno Schuler
aus Lachen (CH)

2015

Promotionsgesuch eingereicht am 25. März 2015. Die Arbeit wurde angeleitet von Dr. Leo Gross, Dr. Gerhard Meyer und Prof. Dr. Jascha Repp.

Prüfungsausschuss:

Vorsitzender:	Prof. Dr. Klaus Richter
1. Gutachter:	Prof. Dr. Jascha Repp
2. Gutachter:	Prof. Dr. Dominique Bougeard
Weiterer Prüfer:	Prof. Dr. Christian Schüller

Termin Promotionskolloquium: 9. Juli 2015

Abstract

Scanning probe microscopy techniques offer the unique possibility to characterize and manipulate atomic-scale objects atom-by-atom. In this thesis, we study structural and electronic properties of single molecules, defects and atoms on two-monolayer thick NaCl islands on Cu(111) by a combination of low-temperature scanning tunneling microscopy (STM), atomic force microscopy (AFM) and Kelvin probe force microscopy (KPFM). Specifically, we exploit the enhanced resolution obtained with functionalized tips; a deterministic chemical modification of the last atoms of the scanning probe tip.

First, the performance of different tip functionalizations is assessed and based on these findings, the underlying contrast mechanisms in AFM and KPFM could be identified. Next, different molecular model systems are examined to describe how important molecular properties such as chemical structure, bond order, adsorption geometry and intramolecular charge distribution can be measured by AFM. Thereby, current understanding of the qualitative and quantitative AFM and KPFM contrast is pushed forward.

Then, we apply atomic-resolution AFM and molecular orbital imaging by STM to identify and characterize synthetic products, purified natural compounds and complex mixtures. Finally, atomic manipulation is used to trigger chemical reactions on single molecules, to generate defect structures on the surface, to control the charge state of adatoms and mechanically actuate an atomic switch implemented by an embedded adatom.

Contents

Abstract	iii
Introduction	1
I. Fundamentals of Scanning Probe Microscopy	4
1. Brief historical outline	5
2. Scanning tunneling microscopy (STM)	8
2.1. Theory	10
3. Noncontact atomic force microscopy (NC-AFM)	14
3.1. Theory	16
3.1.1. Force contributions and their effect on Δf	18
3.2. Kelvin probe force microscopy (KPFM)	21
II. Experimental Details and Methods	23
4. UHV chamber and low-temperature STM/AFM	24
4.1. qPlus sensor	26
4.2. Scan parameters and methods	28
5. Sample system NaCl(2ML)/Cu(111)	30
5.1. Sample and tip preparation	30
III. Results	33
6. Effects of tip functionalization in SPM	34
6.1. Tip functionalization by controlled vertical manipulation . . .	35
6.2. Performance of different tips for STM and AFM	38
6.3. AFM and KPFM contrast on ionic surfaces with different tips	41

7. Molecular properties measured by AFM	46
7.1. Bond-order discrimination	46
7.2. Tilting of the CO tip molecule and effect of fluorination . . .	54
7.3. Adsorption geometry determination	61
7.4. Contrast formation in KPFM on molecules	71
8. Chemical structure identification	85
8.1. TNP: Giant nanographene	86
8.2. Breitfussin A: Single molecule case study	89
8.3. Asphaltenes: Unraveling the chemical structure of a complex mixture	93
9. Atomic manipulation on insulators	101
9.1. Single-molecule chemistry	101
9.1.1. Aryne: Catching the elusive intermediate	102
9.1.2. DBA: Retro-Bergman cyclization	108
9.2. Cl vacancy chains: Effect of electron–phonon interaction on the formation of one-dimensional electronic states	114
9.3. Au atoms on NaCl(2ML)/Cu(111)	122
9.3.1. Au^- , Au^0 & Au^+ : Charge state tristability	122
9.3.2. Au^+ : Toggling the local electric field	124
9.3.3. Au incorporation in NaCl with atomic precision	131
10. Conclusions	135
 IV. Appendix	 138
A. Density functional theory calculations	139
A.1. Charge-transfer complexes	139
A.2. Asphaltenes	141
Bibliography	145
List of Abbreviations	166
Contributions to this work	169
Acknowledgments	171
Curriculum Vitae	172

Introduction

The invention of the scanning tunneling microscope (STM) by Binnig *et al.*¹ is often considered as the birth of experimental nanoscience. They realized the dream of visualizing individual atoms as expressed by Richard Feynman, a conceptual pioneer of nanotechnology, in one of his famous lectures². Subsequently, the STM triggered the development of a myriad of other probe-based techniques, particularly atomic force microscopy (AFM)³. STM and AFM constitute truly groundbreaking developments for surface science as they render the determination of the atomic structure of virtually any material possible. Many functionalities of materials are directly associated with their structure, specifically in the case of molecules. Francis Crick, the discoverer of the structure of DNA, phrased this appropriately: “If you want to understand function, study structure”. One of the underlying motivation of this thesis is to explore the atomic and electronic structure of atomic-scale objects such as molecules, defects and atoms and to push the limits of qualitative and quantitative information that can be obtained by AFM. In the following we will highlight milestone experiments of recent years that lay the foundation for the work presented in this thesis.

Besides the extraordinary resolution demonstrated by STM⁴, the public and scientific fascination for STM was quickened by atomic manipulation; the deterministic placement of individual atoms^{5,6}. This technique allowed constructing artificial nanostructures^{7,8} and triggering chemical reactions on the surface^{9–12}. STM was also used to study electron transport through single-molecule junctions^{13–15} and vibrational spectroscopy^{16,17} of single molecules based on inelastic electron tunneling spectroscopy (IETS). Further, molecules could be coupled to light, for measuring vibronically resolved fluorescence^{18,19} and plasmon-enhanced Raman spectroscopy²⁰. The introduction of a few atomic-layers thick insulators in STM studies²¹ marks a significant conceptual change. The electronic decoupling renders possible to probe adsorbates close to their native state. It facilitates to study spin excitations²² and spin dynamics²³ in single atoms and nanostructures^{24,25}, direct imaging of frontier orbitals of molecules²⁶, providing insights into the formation of chemical bonds^{12,27} and tautomerization reactions of molecules^{28,29}. In addition, insulating films can stabilize

different charge states of atoms^{30,31}.

In recent years, enormous progress has been made in AFM too, initiated by the introduction of the frequency modulation mode³² in noncontact AFM (NC-AFM) and demonstration of true atomic-resolution³³. For example, the force required to move an atom³⁴ or operate a molecular switch³⁵ was determined, surface atoms could be chemically identified³⁶, or the magnetic exchange force measured with spin-polarized tips³⁷. Most relevant for this thesis, the chemical structure of a single molecule³⁸ could be imaged, which was used for the identification of an organic compound³⁹, and the charge distribution of a molecule could be measured by Kelvin probe force microscopy (KPFM)⁴⁰. Another important trend is the use of functionalized tips, which provides a controlled way to enhance the resolution in STM⁴¹ and AFM³⁸ and is an important concept to understand the imaging mechanism experimentally⁴² and theoretically⁴³. The development of the qPlus sensor⁴⁴, which allows for simultaneous STM and AFM operation with a simple detection scheme, has made a significant contribution to the dissemination of NC-AFM in the scanning probe community.

This thesis is devoted to study structural and electronic properties of single molecules, defects, and atoms on two-monolayer thick NaCl islands on copper using a combination of STM, AFM and KPFM with functionalized tips and thereby examine the relevant imaging mechanisms of the respective technique. The objective is to find out which properties of molecules, defects and atoms can be measured and to apply these findings to relevant questions in chemistry and surface science.

In part I, a brief introduction to the basic principles of STM, AFM and KPFM is given, prefaced by a short description of the historic evolution of STM and AFM. In part II, the low-temperature STM/AFM setup is described with a special focus on the working principle of the qPlus sensor in section 4.1. This part is completed by section 5.1, describing the sample and tip preparation.

The main results of the thesis are presented in part III. First, in chapter 6, methods are described how tips terminated by individual Cl, Br, I, Xe and Kr atoms and CO and NO molecules can be created and their performance for STM and AFM operation on molecules is assessed. Additionally, a single Cl vacancy is used to explain the contrast formation in AFM and KPFM on ionic surfaces by means of different tip functionalizations. In chapter 7 we choose different molecular model systems to demonstrate how

one can gain information about bond order (section 7.1), adsorption geometry (section 7.3) and charge distribution (section 7.4) of a single molecule and discuss the influence of CO tip tilting (section 7.2).

In chapter 8, we apply the method of high-resolution AFM discussed in the preceding chapters for the identification and characterization of synthetic products and unknown natural compounds. First, in section 8.1, the atomic structure of a synthetic hydrocarbon is verified. Then the elucidation of the molecule Breitfussin A is described and general conclusions are drawn how and when AFM-assisted structure elucidation is suited (section 8.2). Thereafter, in section 8.3, we analyze one of the most complex and intriguing molecular mixtures existing: the solid component in petroleum, the asphaltenes.

In chapter 9 we use atomic manipulation to trigger chemical reactions of molecules, to generate defects on the surface, to control the charge state of adatoms, to mechanically actuate an atomic switch and to incorporate single metal atoms in an insulator. First, two examples of single-molecule reactions and the analysis of reaction products by atomic-resolution AFM imaging are presented in section 9.1. We report the generation and characterization of aryne, a very reactive intermediate, caught for the first time (section 9.1.1). In section 9.1.2, we dehalogenate a dibromoanthracene molecule to a dehydroanthracene biradical and induce a retro-Bergman cyclization reaction to form diyne. The Bergman reaction can be reversed, and thus we demonstrate reversible breaking and making of covalent intramolecular bonds. Then, in section 9.2, short arrays of Cl vacancies are created to investigate the formation of one dimensional electronic states in the presence of strong electron-phonon interaction. Finally, the adsorption characteristics of Au atoms in different charge states are discussed in section 9.3. Here, we look in detail how Au cations can be mechanically switched between two adsorption sites and how this affects the local electric field (section 9.3.2). In section 9.3.3, the atomic-precise implantation of Au atoms in NaCl films is reported, templated by Cl vacancies. The thesis is summarized in the conclusions chapter 10.

Part I.

**Fundamentals of Scanning Probe
Microscopy**

CHAPTER 1

Brief historical outline

In 1981, Binnig and Rohrer established the field of nanotechnology by their invention of the scanning tunneling microscope (STM) at the IBM Zurich Research Laboratory¹. It was the first instrument capable of imaging the surface of a material in real-space with atomic precision⁴⁵. Shortly after its invention, the STM solved the adatom structure of the 7×7 surface reconstruction of the Si(111) surface⁴, one of the most intriguing problems in surface science at that time. Already a few years after, in 1986, Binnig and Rohrer were awarded with the Nobel Prize in Physics for their invention, which was in the meantime very well received as an invaluable tool in surface science.

Apart from the brilliant simplicity of its concept, the STM suffers from several severe limitations and challenges. The STM detects the current that can flow between two electrodes, a tip and a sample surface, hence it is restricted to conductive materials. As a result of their high surface reactivity, metals and semiconductors permanently adsorb and desorb molecules from their environment. This usually requires to conduct STM experiments in ultra-high vacuum (UHV), making high demands on the technical implementation of the STM. The close proximity (typically less than one nm) of the tip to the sample requires extreme stability and proper vibrational isolation of the microscope.

Early on it was noticed that there act significant forces between the microscope tip and sample. Based on these forces, Binnig, Quate and Gerber developed the atomic force microscope (AFM)³. The promising concept of using forces instead of the current as the imaging signal, enabled to study virtually any surface. However, in contrast to the STM, it took almost a decade for the AFM to achieve true atomic resolution³³.

In AFM, a tip is mounted on a flexible beam, called cantilever, which bends upon a force acting on the tip. Initially the deflection was measured by a STM mounted on the metalized backside of the cantilever. Later, optical⁴⁶ and piezoelectric⁴⁴ detection schemes have prevailed. Depending

1. Brief historical outline

on the application, several operation modes are used in AFM that can be classified into contact (or static) and noncontact (or dynamic) modes. In the contact mode, the tip is in contact with the surface. The force on the tip leads to a proportional static deflection of the cantilever. In the noncontact mode, the cantilever is actuated close to its eigenfrequency. The restoring force of the oscillation enables stable operation (avoiding the jump-to-contact problem) at close tip-sample distances without making physical contact. The force between tip and surface upon approach changes this eigenfrequency of the cantilever. This frequency change is the basis for the amplitude- and frequency-modulation mode in noncontact AFM, discussed in detail in chapter 3.

The first AFMs were contact AFMs and atomic resolution was achieved on a graphite surface⁴⁷ under ambient conditions and on NaCl in UHV⁴⁶ among others. However, in these measurements no atomic defects could be observed because the normal load for typical contact AFM measurements considerably exceeded the load limit of a single atom⁴⁸. Only several years after, Giessibl³³ and Kitamura and Iwatsuki⁴⁹ finally achieved true atomic resolution using noncontact AFM in UHV on the Si(111)- 7×7 surface.

In the course of the aim to achieve atomic resolution with AFM one has encountered several problems that significantly prolonged the achievement of this goal in contrast to STM. First, because of the large contact area, true atomic resolution could not be achieved by contact AFM. The jump-to-contact problem in noncontact AFM that causes soft cantilevers to snap to the surface required large oscillation amplitudes. However, large amplitude operation is less sensitive to short-range forces (causing atomic corrugation), that are convoluted with long-range forces. Stiffer cantilevers could circumvent this problem. The non-exponential and non-monotonic force-distance dependence further impeded the quest for atomic resolution. In addition, NC-AFM needs several feedback circuits and therefore requires more complex feedback electronics than STM.

Nevertheless, NC-AFM succeeded in achieving atomic-resolution on metals, semiconductors and insulators. Finally, NC-AFM could even surpass the lateral resolution of STM that is fundamentally limited by the distributed electronic states at the Fermi level.

After the STM and AFM, a large number of different probe based techniques, subsumed under the term scanning probe microscopy, have been developed. Many of these tools are widely used for scientific research and industrial applications alike. To name some of them: Electrostatic force

microscopy⁵⁰ measures the electrostatic interaction, Kelvin probe force microscopy⁵¹ the local work function difference and scanning capacitance microscopy⁵² the local capacitance between the tip and the sample. Near-field optical microscopy⁵³ measures optical properties with high spatial and temporal resolution and scanning thermal microscopy⁵⁴ maps the local temperature and thermal conductivity of the sample. Furthermore, magnetic force microscopy⁵⁵ and spin-polarized STM⁵⁶ are used to probe magnetic properties.

CHAPTER 2

Scanning tunneling microscopy (STM)

In this chapter we will discuss the fundamental principles of STM. First, the function principle of STM is explained, followed by a qualitative argument for its high resolution. In section 2.1 a quantitative expression for the tunneling current is derived.

The STM is based on the quantum mechanical tunneling effect⁵⁷. Hereby, a particle with a certain kinetic energy has a finite probability to pass a potential barrier that it could classically not surmount. This is a general physical phenomenon and plays an essential role in nuclear fusion/fission, quantum tunneling-induced mutations in biology or modern electronic devices such as tunnel diodes. In STM, the tunneling particle is an electron and the potential barrier the vacuum gap between a conductive sample and a conductive tip. The STM tip acts as a local probe that is scanned laterally over the sample surface.

In Fig. 2.1a a scheme of a basic STM set-up is depicted. The set-up consists of a conductive tip positioned typically a few Ångströms above a conductive sample with a low roughness. The tip can be moved in all spatial directions by a piezo scanner that allows an accurate positioning of the tip by a few picometers within a typical scan range of 1 – 100 μm . These piezoelectric translators expand or contract in certain crystal directions when a voltage is applied across the material due to a change in its crystal structure. Between the tip and sample electrodes, a bias voltage up to a few volts is applied. Due to the tunneling effect, a small current typically in the range between pA and nA can be detected. The tip is scanned over the surface in a raster-like fashion line-by-line. Two scanning modes are usually differentiated: Constant current mode and constant height mode. In the commonly used constant current mode, the tip-sample distance z is controlled to maintain a certain tunneling current, which can be set as an input for the z feedback loop. The topographic displacements by the z piezos represent the imaging signal.

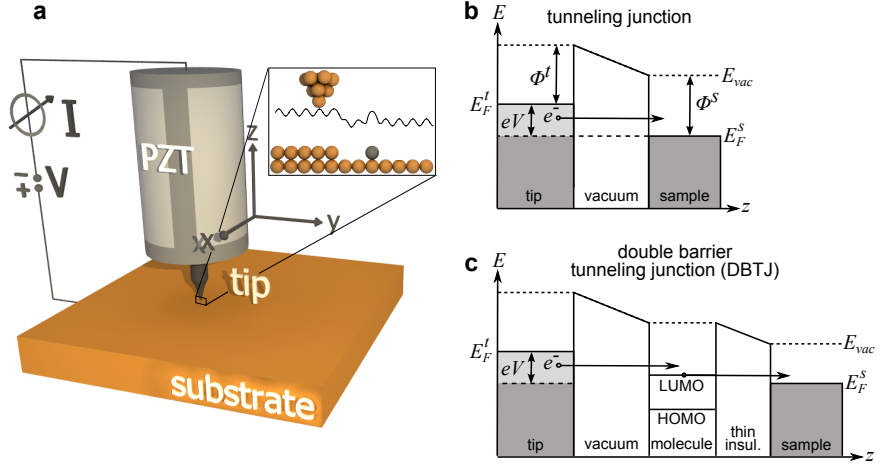


Figure 2.1.: **Functional principles of STM.** **a** Illustration of the main components of a STM: A conductive tip in close proximity to a conductive substrate. The tunneling current I is measured upon applying the bias voltage V . The tunneling current is a function of the tip-sample distance, applied voltage and local density of states (LDOS). The lateral and vertical tip position is controlled by a piezo scanner [usually lead zirconate titanate (PZT)]. Usually, the STM is operated in the constant current mode where the tip-sample distance is controlled by feedback electronics to maintain a constant tunneling current (see inset). **b** Energy diagram of the tunneling junction. At zero temperature all electronic states of the tip and sample up to their Fermi energy E_F^t and E_F^s are occupied. At negative tip bias electrons tunnel from the tip to the substrate through the vacuum gap. Φ_t and Φ_s denote the tip and sample work function. **c** Energy diagram of a double barrier tunneling junction that applies to molecules on thin insulating films. The highest occupied molecular orbital (HOMO) and lowest unoccupied molecular orbital (LUMO) give rise to positive and negative ion resonances.

In the constant height mode, the tip is scanned on a plane parallel to the surface without adjusting z . The imaging signal is then the tunneling current itself. The constant height mode allows higher scan speeds but requires utmost stability of the tip-sample junction. This is achieved by excellent vibrational damping, low drift rates and an atomically flat surface.

An energy diagram of the tip-vacuum-sample junction is displayed in Fig. 2.1b. Classically it would not be possible for an electron in the tip with an energy $E \leq E_F^t$ to overcome an energy barrier with energy $E_F^t + \Phi_t > E$, where Φ_t is the tip work function. From the solution of the Schrödinger equation for an electron near a metal interface, however, it is known that the electron wavefunction exponentially decays in the

2. Scanning tunneling microscopy (STM)

vacuum region. That is, the electron has a finite probability to be in the other electrode and hence it has a nonzero transmittance. The exponential decay of the electron wavefunction results in an exponential decay of the tunneling current as a function of the tip-sample separation, which finally facilitates the atomic resolution achieved with STM.

In this thesis, we are often interested in intrinsic properties of adsorbates, unaffected by their substrate. When adsorbed on metal surfaces, adsorbates electronic states are often heavily perturbed by metal states. To prevent hybridization of adsorbate states an insulating layer between the adsorbate and the metal substrate is introduced^{17,22,26,30,58}. To maintain the tunneling capability, this layer has to be ultrathin (in our case two atomic layers). The introduction of an additional potential barrier changes the tip-sample geometry to a double-barrier tunneling junction, schematically shown in Fig. 2.1c. In this geometry the electron tunnels sequentially from a tip state to an adsorbate state within the bias window (if available) and subsequently to a substrate state⁵⁹. Accordingly, the adsorbate electronic states near the Fermi energy can be probed.

2.1. Theory

To find a quantitative expression of the tunneling current we follow the formalism introduced by Bardeen⁶⁰ in 1961, who originally considered metal-insulator-metal junctions when working in the field of superconductivity. In this approach, the tip and sample are treated as separate entities such that the system becomes separable. The proximity of both electrodes are treated as a perturbation potential for the unperturbed states of the counter-electrode. The Schrödinger equation of the combined system with the Hamiltonian H is given by

$$i\hbar \frac{\partial \Psi}{\partial t} = \left(-\frac{\hbar^2}{2m} \nabla^2 + U_t + U_s \right) \Psi \quad (2.1)$$

where U_t and U_s are the tip and sample potential, respectively. If we assume that the sample and tip states are zero in the respective counter-electrode, we can approximate the total wavefunction by the eigenstates of the isolated sample and isolated tip within the respective electrode

$$\Psi(\mathbf{r}) = \begin{cases} \psi_\mu(\mathbf{r}) & , \text{ if } \mathbf{r} \in \text{sample} \\ \chi_\nu(\mathbf{r}) & , \text{ if } \mathbf{r} \in \text{tip} \\ \tilde{\Psi}(\mathbf{r}) & , \text{ otherwise} \end{cases}$$

where the indices μ and ν denote the different states. The electronic states ψ_μ and χ_ν of sample and tip may be obtained by solving the time-independent Schrödinger equations of the two subsystems individually. An electron that is initially in the state ψ_μ of the sample can be transferred to the state χ_ν of the tip. Using time-dependent perturbation theory (Fermi's Golden rule) one can get the probability w of an electron in the state ψ_μ at E_μ to tunnel into a state χ_ν at E_ν

$$w = \frac{2\pi}{\hbar} |M_{\mu\nu}|^2 \delta(E_\mu - E_\nu) \quad (2.2)$$

where the tunneling matrix element $M_{\mu\nu} = \langle \psi_\mu | H | \chi_\nu \rangle$ is according to Bardeen⁶⁰ given by

$$M_{\mu\nu} = \frac{\hbar^2}{2m} \int_{\Omega} (\psi_\mu^* \nabla \chi_\nu - \chi_\nu \nabla \psi_\mu^*) d\mathbf{S}. \quad (2.3)$$

This equation corresponds to the probability current integrated over an arbitrary surface Ω between the tip and the sample. By considering only sample and tip states with $E_\mu = E_\nu$ in eq. (2.2), only transitions are allowed that conserve energy (elastic tunneling). To obtain the tunneling current I at the bias voltage V we require in addition that electrons can only tunnel from an occupied into an unoccupied state in the counter-electrode. Further, we need also to subtract the transmission rate in the opposed direction. From these considerations one gets that

$$I = \frac{4\pi e}{\hbar} \sum_{\mu,\nu} \{f(E_\mu)[1 - f(E_\nu + eV)] - f(E_\nu + eV)[1 - f(E_\mu)]\} \times |M_{\mu\nu}|^2 \delta(E_\mu - (E_\nu + eV)) \quad (2.4)$$

where $f(E)$ is the Fermi–Dirac distribution describing the mean occupation probability of the state at energy E . A factor of two is included to account for the spin degeneracy. This equation can be rewritten in an energy integral ^a

^aHere we implicitly assume that the mean transition rate $|M(\epsilon, V)|^2$ per state in a given energy interval $\delta\epsilon$ add up on both sides of the tunneling barrier. That is, *s*-, *p*- or *d*-like states contribute equally to the tunneling current (which is not necessarily the case).

2. Scanning tunneling microscopy (STM)

$$I = \frac{4\pi e}{\hbar} \int_{-\infty}^{\infty} [f(E_F - eV + \epsilon) - f(E_F + \epsilon)] \times \rho_t(E_F - eV + \epsilon) \rho_s(E_F + \epsilon) |M(\epsilon, V)|^2 d\epsilon, \quad (2.5)$$

where ρ_t and ρ_s are the tip and sample density of states, respectively, given by

$$\rho_t(E) = \frac{1}{\text{vol}} \int \left(\sum_{\nu} |\chi_{\nu}(\mathbf{r})|^2 \delta(E_{\nu} - E) \right) d\mathbf{r}. \quad (2.6)$$

In the low temperature limit^a ($T \rightarrow 0$), the Fermi–Dirac distribution becomes a step function and eq. (2.5) simplifies to

$$I = \frac{4\pi e}{\hbar} \int_{E_F}^{E_F + eV} \rho_t(\epsilon - eV) \rho_s(\epsilon) |M(\epsilon, V)|^2 d\epsilon. \quad (2.7)$$

It should be noted that this equation only holds for small biases ($eV \ll \Phi$). Otherwise, an energy and bias dependent transmission factor has to be considered that respects for the higher tunneling probability of higher energy electrons because of the lower effective barrier height. To solve eq. (2.7) one has to approximate the tunneling matrix element M , because the exact tip and sample wavefunctions are unknown. In the approximation developed by Tersoff and Hamann^{61,62} an explicit form of the tip wavefunctions χ_{ν} is assumed that is spherical symmetric (s-wave). Therefore, they modeled the tip as locally spherical symmetric with radius R centered at \mathbf{r}_0 . Inserting this assumption in eq. (2.7) one obtains

$$I = \frac{32\pi^3 e^2 V \Phi_s^2 \rho_t(E_F) R^2}{\hbar \kappa^4} e^{2\kappa R} \underbrace{\sum_{\nu} |\psi_{\nu}(\mathbf{r}_0)|^2 \delta(E_{\nu} - E_F)}_{\rho_s(\mathbf{r}_0, E_F)} \quad (2.8)$$

where $\kappa = \sqrt{2m\Phi_s/\hbar^2}$, Φ_s is the sample work function and $\rho_s(\mathbf{r}_0, E_F)$ is the local density of states (LDOS) of the sample at the Fermi level. Most important, the tunneling current in the Tersoff–Hamann approximation is proportional to the LDOS of the sample at the Fermi level and position

^aa good approximation for room temperature or below

of the tip. Consequently, the STM tip operated in constant current mode traces a contour of the sample LDOS that decays exponentially in the vacuum and thus

$$I \propto V \rho_s(\mathbf{r}_0, E_F) \propto e^{-2\kappa z}. \quad (2.9)$$

With $\Phi_s = 5 \text{ eV}$ as a typical example for a metal work function, a change of 1 \AA in distance causes a change of one order of magnitude in the tunneling current. The exponential dependence of the tunneling current on the tip height facilitates the high vertical resolution in STM.

CHAPTER 3

Noncontact atomic force microscopy (NC-AFM)

In this chapter we will discuss the fundamental principles of noncontact AFM (NC-AFM) and frequency-modulation AFM (FM-AFM) in specific. First, the function principle of NC-AFM is explained. In section 3.1 the conversion between frequency shift and force is derived.

In NC-AFM a tip is connected to a driven oscillator. Mostly micromachined Si cantilevers are used as an oscillator. Recently, however, quartz crystal resonators such as the qPlus⁴⁴ or Colibri⁶⁴ sensor became more popular due to their greater stiffness. The greater stiffness allows stable operation of the resonator with small amplitudes, which enhance the sensitivity towards short-range forces (see below) and increase the compatibility with combined STM operation.

The cantilever can be characterized by its spring constant k , eigenfrequency f_0 and quality factor Q . When the tip is approached to the surface, the attractive interaction will cause a shift in the eigenfrequency towards lower frequencies. Very close to the surface the tip-sample interaction turns repulsive, leading to a positive frequency shift. This eigenfrequency change is schematically shown in Fig. 3.1a. There are mainly two methods to track the frequency shift: Amplitude-modulation AFM (AM-AFM)³ and frequency-modulation AFM (FM-AFM)³². In AM-AFM the resonator is excited with a fixed, off-resonant drive frequency f_{drive} and fixed excitation amplitude. Changes in the force are detected by changes in the amplitude of the response signal. In FM-AFM the resonator is driven always on-resonance by a feedback loop. Changes in force are directly measured by the frequency shift Δf . A second feedback loop adjusts the drive amplitude to keep the oscillation amplitude A fixed. Because non-conservative forces cause extra dissipation in the motion of the cantilever, the drive amplitude in FM-AFM provides a measure for this dissipation. Under UHV conditions AM-AFM operation is very slow due to the high Q factors and FM-AFM is almost exclusively used.

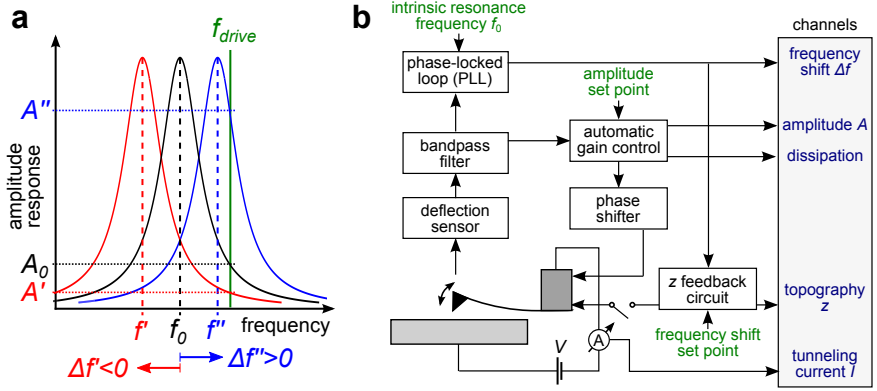


Figure 3.1.: **Functional principles of FM-AFM.** **a** Comparison of amplitude-modulation (AM) and frequency modulation (FM)-AFM. The oscillator has an intrinsic resonance frequency f_0 . Attractive forces decrease this resonance frequency (red curve) such that $\Delta f' = f' - f_0 < 0$ and repulsive forces increase the resonance frequency (blue curve). AM-AFM: Resonator is excited with a fixed, off-resonant drive frequency f_{drive} . Changes in the force are detected by changes in the amplitude A . FM-AFM: Resonator is driven on-resonance by a feedback loop. Changes in force are directly measured by the frequency shift Δf . **b** Schematic diagram of the measured signals and the three feedback loops in FM-AFM: (i) Phase/frequency loop, (ii) amplitude loop and (iii) topography (z) loop. Figure **b** is adapted from Ref. 63.

In Fig. 3.1**b** a feedback scheme for FM-AFM is illustrated. First, the deflection signal of the mechanically actuated cantilever is detected. Here, either optical methods such as beam deflection or fiber interferometry or self-sensing AFM sensors using piezo-electric/-resistive effects are employed. The deflection signal is then routed through a bandpass filter centered around f_0 , which cuts off the noise from unwanted frequency bands. A phase-locked loop (PLL) extracts the frequency shift by matching the phase ϕ of the drive frequency such that the phase difference to the deflection signal is $\phi = \pi/2$. In this case, the driving signal required for establishing the desired oscillation amplitude is minimal. The amplitude loop controls the drive amplitude to keep the oscillation amplitude constant. The adjusted excitation signal is then fed back to mechanically actuate the cantilever at its resonance frequency. If desired an additional feedback loop can be enabled that adjusts the tip height z to achieve a certain Δf set-point. Throughout this thesis, all AFM images are FM-AFM measurements with opened z feedback loop. z feedback was disabled because the non-monotonic $\Delta f(z)$ curve in the distance regime of interest

3. Noncontact atomic force microscopy (NC-AFM)

prevented stable control of Δf .

As output signals one obtains the frequency shift Δf , oscillation amplitude A , drive amplitude (dissipation), topography z and the tunneling current I (if a tip electrode is implemented).

As pointed out by Giessibl⁶⁵, the oscillation amplitude is crucial for the sensitivity towards specific force components. Ideally, the oscillation amplitude should be adjusted to be on the order of the characteristic length scale of the force that should be probed. Here, we are interested in the short-range forces that are responsible for the atomic-scale contrast and vary on the scale of Ångströms. In the measurements presented in this thesis, we use a qPlus sensor (see section 4.1) that is capable of stable operation with sub-Ångström oscillation amplitudes.

3.1. Theory

In this section we derive an approximate expression for the force $F(z)$ as a function of the frequency shift $\Delta f(z)$, the main measurement signal in FM-AFM. Thereafter, we strip down the total force into its different components and discuss their effect on Δf .

The cantilever motion can be treated as a damped harmonic oscillator that is driven externally. Without external forces, the cantilever oscillates at its eigenfrequency $f_0 = (2\pi)^{-1}\sqrt{k_0/m^*}$, where k_0 is its spring constant and m^* its effective mass. An external force F on the cantilever results in a frequency change, commonly called frequency shift Δf . For small oscillation amplitudes^a the external force can be treated in a linear response model, which adds an additional spring with stiffness k_{ts} to k_0 . This changes the resonance frequency of the cantilever to

$$\Delta f = f - f_0 \tag{3.1a}$$

$$\approx \frac{1}{2\pi} \left(\sqrt{\frac{k_{ts} + k_0}{m^*}} - \sqrt{\frac{k_0}{m^*}} \right) \approx \frac{1}{4\pi} \frac{k_{ts}}{\sqrt{k_0 m^*}}. \tag{3.1b}$$

In the last step, the square-root has been approximated in the

^aOne talks about small amplitudes when $\partial F/\partial z$ is about constant within the oscillation cycle. This holds if the amplitude is smaller than the typical interaction length (which is on the order of 1 Å for short-range forces)

limit where $k_{ts} \ll k_0$. By using $\sqrt{m^*} = \sqrt{k_0}/(2\pi f_0)$ it follows that

$$\Delta f \approx \frac{f_0}{2k_0} k_{ts}. \quad (3.2)$$

By definition one obtains $\delta F_{ts} = -k_{ts}\delta z$ for a harmonic potential. Hence, it follows that the frequency shift Δf is proportional to the vertical force gradient

$$\Delta f \approx -\frac{f_0}{2k_0} \frac{\partial F_{ts}}{\partial z}. \quad (3.3)$$

Eq. (3.3) is called the small amplitude limit, which is in good approximation valid for the scan parameters used in this thesis.

For arbitrary amplitudes the relation between the frequency shift and force becomes more complex. One has to consider that the force gradient during the oscillation cycle is not constant but varies depending on the effective tip-sample distance z . A general expression for Δf can be found by using first-order perturbation theory in the Hamilton-Jacobi approach⁶⁶

$$\Delta f = -\frac{f_0^2}{k_0 A} \int_0^{1/f_0} F(z + A[1 + \cos(2\pi f_0 t)]) \cos(2\pi f_0 t) dt \quad (3.4a)$$

$$= -\frac{f_0}{\pi k_0 A} \int_{-1}^1 \left\{ F(z + A[1 + u]) \frac{u}{\sqrt{1 + u^2}} \right\} du \quad (3.4b)$$

This gives us $\Delta f(z)$ as a function of $F(z)$. Since in FM-AFM the measurement signal is the frequency shift and not the force, we need an inversion of eq. (3.4b). An analytic inversion is, however, not known. But there are approximative inversion procedures. Among others, the Sader and Jarvis method^{67,68} is the most commonly used. They described the force as a function of frequency shift using Laplace transformations and obtained

$$F(z) = \frac{2k_0}{f_0} \int_z^\infty \left\{ \left[1 + \frac{\sqrt{A}}{8\sqrt{\pi(t-z)}} \right] \Delta f(z) - \frac{A^{3/2}}{\sqrt{2(t-z)}} \frac{\partial[\Delta f(t)]}{\partial t} \right\}. \quad (3.5)$$

3. Noncontact atomic force microscopy (NC-AFM)

That is, to obtain the force at a specific height z one has to integrate the whole $\Delta f(z)$ spectrum from far away to that specific height. In the experimental part III, we apply a discretized version of eq. (3.5), adapted to our discrete data set $(z_i, \Delta f(z_i)) \equiv (z_i, \Delta f_i)$ recorded at certain equidistant tip heights $z_i = z_1 + (i - 1)\Delta z$, $i = 1 \dots N$ to extract the force $F_i \equiv F(z_i)$.

$$F_i = \frac{2k_0}{f_0} \sum_{j=i+1}^N \left\{ \left[1 + \frac{\sqrt{A}}{8\sqrt{\pi(z_j - z_i)}} \right] \Delta f_j - \frac{A^{3/2}(\Delta f_{j+1} - \Delta f_j)}{\sqrt{2}(z_j - z_i)\Delta z} \right\} \Delta z \quad (3.6)$$

For the force analysis in part III, eq. (3.6) is used instead of the small amplitude limit, which yields a force accuracy of about 1%⁶⁷.

3.1.1. Force contributions and their effect on Δf

As detailed in the previous sections, there is no one-to-one correspondence between the measured frequency shift in FM-AFM and the forces acting between the tip and sample. The total force is a sum of different force components, which are long-ranged and short-ranged. Depending on the scan parameters that are used in FM-AFM, the contributions of force components with a certain range can be increased or decreased. In this section we discuss the major tip-sample interactions that are relevant for measurements in UHV and estimate their relative strength for the scan parameters used in this thesis.

Inter-molecular van der Waals forces: The inter-molecular van der Waals (vdW) forces stem from electrostatic interactions between dipole moments of nearby atoms (in different molecules). The term vdW forces is ambiguously used in literature but usually combines the force between permanent dipoles (Keesom force), a permanent dipole and a corresponding induced dipole (Debye force) and the force between fluctuating dipoles and the corresponding induced dipoles (London dispersion force). The latter is always attractive, isotropic and present between all atoms. In general, the vdW forces are anisotropic and can have attractive and repulsive contributions. However, the dispersion force represents normally the main contribution to the vdW forces and is exclusively considered in the following. For two atoms separated by a distance z , the vdW forces are proportional to $-z^{-6}$.

The vdW forces between the macroscopic tip and sample surface can be obtained by modeling the tip as a paraboloid and adding up all diatomic vdW forces. This approach yields⁶⁹

$$U_{\text{vdW}} = -\frac{HR}{6z} \quad (3.7a)$$

$$F_{\text{vdW}} = -\frac{\partial U_{\text{vdW}}}{\partial z} = -\frac{HR}{6z^2} \quad (3.7b)$$

for the vdW potential and the resulting vertical force between the tip and sample. H denotes the material-dependent Hamaker constant and R the tip radius. To give a rough estimate, a Hamaker constant of $H = 1 \text{ eV}$ and a tip with $R = 100 \text{ nm}$ results in a force of 10 nN at a distance of 5 \AA .

The vdW forces are considered long-ranged because they do not vary significantly on the atomic scale. From eq. (3.7) it is evident that a sharper tip reduces the vdW forces.

Electrostatic force: The electrostatic force arises from the potential difference between tip and sample. On the atomic scale, this originates from local charges, as for example on ionic surfaces, that may lead to atomic contrast⁷⁰. On the macroscopic scale, the conductive tip and sample form a capacitor with a distance-dependent capacitance $C(z)$. The potential electric energy and force is then

$$U_{\text{el}} = -\frac{1}{2}C(V - V^*)^2 \quad (3.8a)$$

$$F_{\text{el}} = \frac{1}{2}\frac{\partial C}{\partial z}(V - V^*)^2 \quad (3.8b)$$

where V^* is the contact potential difference. This force is long-ranged and always attractive. The contact potential difference can also be employed for Kelvin probe force microscopy (see section 3.2).

Chemical force: Chemical forces are responsible for bond formation between atomic species on the length scale of Ångströms. The chemical interaction between two neutral atoms is composed of a short-ranged repulsive term and an attractive term from vdW forces discussed above. The repulsive interaction describes the Pauli repulsion due to overlapping of electron orbitals. One model pair-potential that describes this interaction is the Lennard-Jones potential

3. Noncontact atomic force microscopy (NC-AFM)

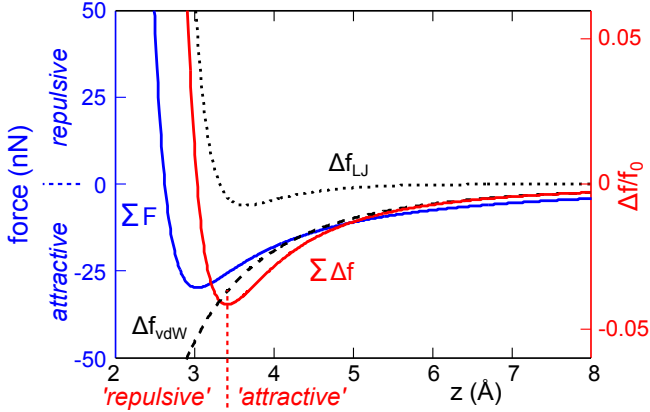


Figure 3.2.: **Force and Δf .** Distance dependence of the force F and frequency shift Δf from a Lennard-Jones (LJ) and van der Waals (vdW) potential. For the LJ and vdW potential the following parameters have been used: $E_{\text{bond}} = 2 \text{ eV}$, $z_0 = 3 \text{ \AA}$, $H = 1 \text{ eV}$ and $R = 100 \text{ nm}$. The LJ (black dotted line) and vdW contributions (black dashed line) to the total Δf (red line) are indicated. The blue curve corresponds to the total force. In NC-AFM it is common to distinguish between 'attractive' and 'repulsive' branch based on the minimum in $\Delta f(z)$ instead of the sign in $F(z)$.

$$U_{\text{LJ}} = E_{\text{bond}} \left(\left(\frac{z_0}{z} \right)^{12} - 2 \left(\frac{z_0}{z} \right)^6 \right) \quad (3.9a)$$

$$F_{\text{LJ}} = \frac{12E_{\text{bond}}}{z_0} \left(\left(\frac{z_0}{z} \right)^{13} - \left(\frac{z_0}{z} \right)^7 \right) \quad (3.9b)$$

where E_{bond} is the depth of the potential (binding energy) and z_0 the equilibrium distance. The functional form of the repulsive term z^{-12} has no clear physical justification but is empirically a good approximation and efficiently to compute.

In Fig. 3.2 the total force resulting from the sum of vdW and chemical forces is plotted using typical parameters. The individual contributions to the frequency shift that result from these forces are indicated as well.

Since the exact tip shape and chemical composition is usually unknown, one cannot separate the different force contributions in experiment or from theory. Our experimental approach of using an atomically defined tip termination on a small metal apex cluster (see section 6), however, allows us

3.2. Kelvin probe force microscopy (KPFM)

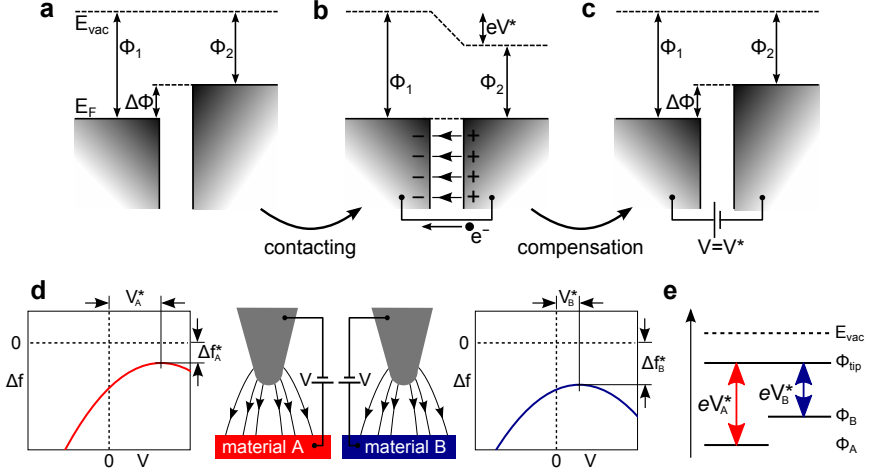


Figure 3.3.: **KPFM Scheme.** **a** Two isolated metals with work functions Φ_1 and Φ_2 share the same vacuum level E_F . Their Fermi levels differ by $\Delta\Phi$. **b** When the two materials are brought into electrical contact, the Fermi levels align by an exchange of electric charge. The surface charges build up an electric field and a corresponding voltage drop of $V^* = \Delta\Phi/e$ across the vacuum gap. **c** A bias voltage of $V = V^*$ can compensate the contact potential difference. **d** Exemplary $\Delta f(V)$ curves measured on two materials with different work functions. At the vertex point $(V^*, \Delta f^*)$ of the parabola, the electrostatic force is minimized. **e** Energy diagram of the different work functions with the quantity V^* that is measured by KPFM indicated.

to minimize the influence of long-ranged forces and enhance and control the short-range interaction that vary on the atomic scale.

3.2. Kelvin probe force microscopy (KPFM)

Kelvin Probe force microscopy (KPFM) is an AFM-derivative that combines a Kelvin probe with an AFM. The Kelvin principle was originally developed by Lord Kelvin in 1898 to measure the work function of materials⁷¹. The basic principle of the Kelvin method is shown in Fig. 3.3a-c. When two metals with different work functions Φ_1 and Φ_2 are brought into electrical contact, electrons flow from the metal with the higher Fermi level to the metal with the lower one until the Fermi levels are aligned. As a result from this compensation current an electric field and a contact potential $V^* = (\Phi_1 - \Phi_2)/e$ builds up. By applying a compensation voltage of the same amount, the contact potential can be determined.

3. Noncontact atomic force microscopy (NC-AFM)

In KPFM the high lateral resolution of AFM is combined with the Kelvin method to measure local variations of the work function difference. One possibility to implement the Kelvin principle in AFM is by force-bias spectroscopy⁵¹. Thereby, the frequency shift is recorded when sweeping the bias voltage with disabled z feedback (see Fig. 3.3d). As discussed in the previous section, the electrostatic force and therewith Δf , quadratically depends on the applied voltage [eq. (3.8)]. To compensate for the electrostatic field in the tip-sample junction, a matching external field with opposite polarity has to be applied. This is the case at the vertex point (V^* , Δf^*) of the $\Delta f(V)$ parabola where the electrostatic force between tip and sample is minimized. The quantity V^* is called local contact potential difference (LCPD). Due to the inhomogeneity of the tip-sample junction, the electrostatic field can only be minimized but not nullified (like for parallel plate capacitors). Besides geometric inhomogeneities, materials^a with different work functions in the junction can contribute, giving rise to so-called averaging effects. Since the mesoscopic tip shape considerably influences the tip work function, it is not possible to quantitatively recover the sample work function by KPFM on the atomic scale. However, work function differences between different surfaces of sufficient area can be determined as illustrated in Fig. 3.3e. In this thesis, V^* maps are often referred to as LCPD maps, which is common parlance in the community.

^aDepending on the junction size the meaning can range from extended surfaces to individual atoms.

Part II.

Experimental Details and Methods

CHAPTER 4

UHV chamber and low-temperature STM/AFM

All presented measurements in this thesis are conducted with a low-temperature, ultrahigh vacuum (UHV) STM/AFM system that was developed and improved by Gerhard Meyer⁷² and later commercialized by Sven Zöphel. The apparatus is a modified version of a commercial system from CreaTec Fischer & Co GmbH. A very similar system design is extensively described in Ref. 73.

In the following the individual components of the system are described, highlighting the crucial prerequisites to enable high-resolution STM and AFM operation.

A photograph of our STM/AFM system is shown in Fig. 4.1a. It consists of three UHV chambers: A chamber housing the microscope, which is separated by a gate valve from the preparation chamber and load-lock connected to the preparation chamber. The load-lock is pumped by a turbomolecular pump that allows introducing samples and tools to be transferred without breaking the vacuum. The two main chambers are pumped by an ion getter pump and a titanium sublimation pump where pressures around 10^{-10} mbar are routinely achieved. The preparation chamber is equipped with different crucibles (e.g. for alkali halides), a sputter gun and neon gas inlet, a mass spectrometer for rest gas analysis, and a storage for samples, evaporators (e.g. for metals) and other tools. The rotatable manipulator is used during sample preparation and for the sample transfer to the microscope chamber and can be cooled to liquid nitrogen or helium temperatures. The samples can either be heated indirectly by a resistive button heater on the sample holder or by direct current heating for low-conductive samples. A NiCr/Ni thermocouple monitors the sample temperature. This allows preparing and transferring the samples in a large temperature range, which is of vital importance for material growth.

The bath cryostat is mounted on the microscope chamber with a capacity of 15 l liquid nitrogen and 4 l liquid helium with refill cycles of 42 h and 72 h,

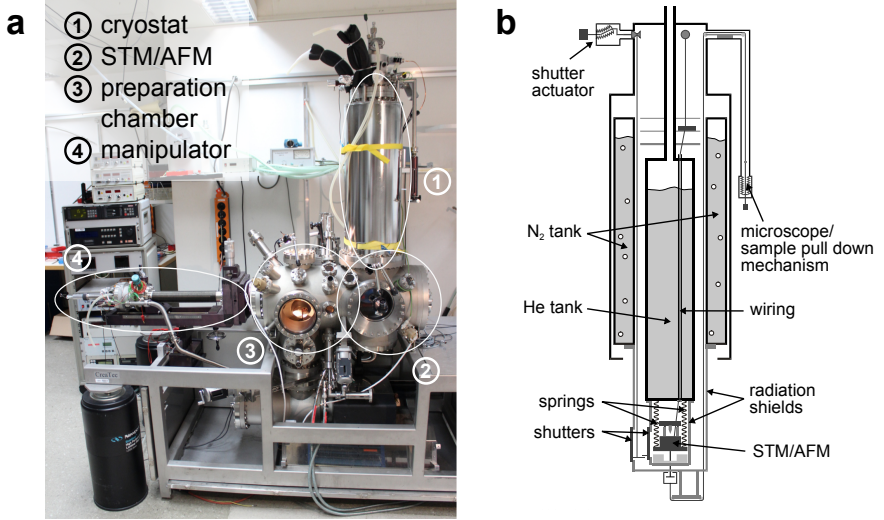


Figure 4.1.: **Experimental setup.** **a** Photograph of the UHV preparation and microscope chamber and the bath cryostat. **b** Cross-section of the bath cryostat and STM/AFM (after Ref. 74).

respectively. It affords SPM operation temperatures of 5 K. As the chilled radiation shields act additionally as efficient cryogenic pumps, the residual gas pressure within the helium cooled shields is even several orders of magnitude lower than the base pressure in the preparation chamber, keeping the samples clean for months. The microscope stage itself is suspended by soft springs from the cryostat base at liquid He temperature. To further achieve adequate vibrational isolation, the setup is constructed in the basement of the building and the frame that supports the vacuum chambers is mounted on active pneumatic vibration dampers. In addition, there is an eddy current damping for the suspended microscope. The scanner is based on a Besocke beetle-type design that includes a ramp ring with slightly inclined planes. In the center of this ramp ring the sensor is mounted on a small (lead zirconate titanate) piezo tube that drives the tip oscillation. The ring itself is resting on three outer piezo tubes with sapphire balls on top. Based on inertial movement of the ramp ring on the sapphire balls, coarse motion of the tip can be performed (slip-stick motion). Displacing all piezos in the same direction results in lateral movement (x, y), while tangential displacement (i.e. circular motion of the ramp ring) results in vertical motion (z). Both, coarse motion and (x, y, z) scanning is performed with these outer

4. UHV chamber and low-temperature STM/AFM

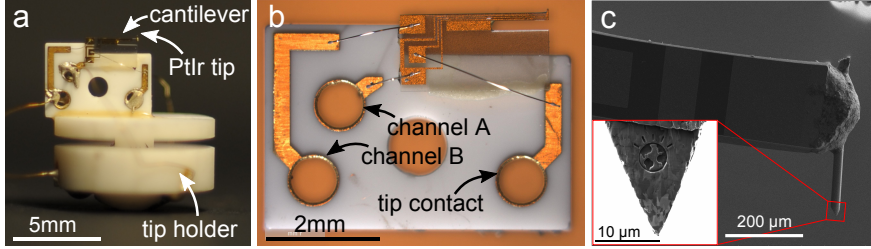


Figure 4.2.: **qPlus sensor.** **a** Photograph of the qPlus sensor. The quartz cantilever is glued on a square ceramic substrate, which is glued onto the transferable tip holder. **b** Optical microscope image of the qPlus sensor without tip holder and tip wire. On the quartz cantilever there are several Au electrodes applied to collect the induced charges due to the strain caused by the vertical deflection of the beam (channels A/B) and one central service electrode to provide electrical contact to the conductive tip⁷⁵. **c** Scanning electron microscope (SEM) image of the cantilever after shortening and sharpening the PtIr tip by focused ion beam (FIB). The inset shows a close-up FIB image of the tip apex with the IBM smarter planet logo engraved.

piezos.

4.1. qPlus sensor

As a sensor, a quartz cantilever is used, which is a modification⁷⁵ of the original design of a quartz tuning fork glued to a substrate introduced by Franz J. Giessibl⁴⁴ that is commonly called qPlus sensor. Different qPlus sensors, all designed and provided by Franz J. Giessibl have been used. Quartz tuning forks are highly optimized devices to clock watches and are produced in huge numbers by the watch industry. The piezoelectricity of quartz provides a simple self-sensing detection scheme that translates the mechanical oscillation of the quartz fork into an electrical signal. The mechanical properties of this material have been optimized to show small variations with temperature, which reduces thermally induced frequency noise. As a consequence of its high stiffness, the qPlus sensor can be stably operated with sub-Ångström oscillation amplitudes. As discussed in chapter 3, small amplitudes increase the sensitivity to short-range forces, hence, the qPlus sensor is favored over conventional micro-machined Si cantilevers for high-resolution imaging. In addition, a separate tip electrode that is integrated in the cantilever enables combined STM and AFM operation.

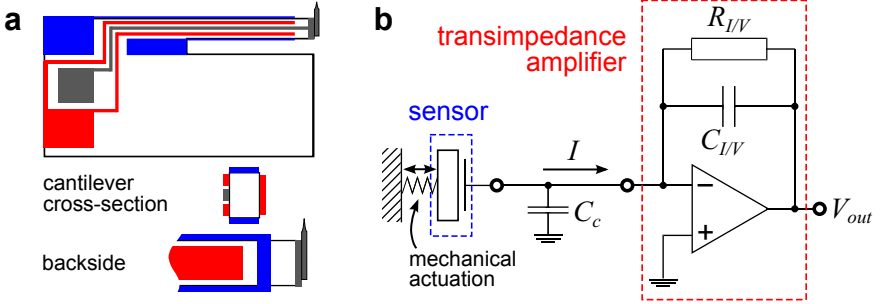


Figure 4.3.: **qPlus deflection sensing.** **a** Schematic of the qPlus sensor contacts. **b** Sensor and current-to-voltage (I/V) converter circuit elements that is used to amplify the deflection signal.

In Fig. 4.2a one of the employed qPlus sensors is shown. For the measurements shown in part III two different cantilever designs were used with the following characteristics: (i) $k \approx 1800 \text{ Nm}^{-1}$, $f_0 \approx 30 \text{ kHz}$ and (ii) $k \approx 1800 \text{ Nm}^{-1}$, $f_0 \approx 73 \text{ kHz}$, and Q factors differed between 10 000 and 300 000. To assemble the sensor, the cantilever is glued onto an insulating ceramic substrate. On the cantilever several metal electrodes are attached for the deflection sensing of the piezoelectric material (channel A/B in Fig. 4.2b) and one service electrode in the center for conducting the tunneling current. Due to mechanical stress caused by the beam deflection, charge accumulates on the electrodes. The resulting compensating current is amplified and converted by a transimpedance amplifier to sense the cantilever oscillation as an ac-voltage. A possible cross-talk of the deflection onto the current electrode or vice versa is minimized by its central location on the cantilever. As the STM/AFM tip, a piece of a $25 \mu\text{m}$ thin PtIr wire is glued to the free prong. The sensor is then mounted on a MACOR tip holder that can be transferred *in situ* as a whole.

Transimpedance amplifiers are used to convert and amplify the current (gain 10^{10}) and deflection signal (gain $10^6 - 10^8$). Both amplifiers are installed in close proximity to the microscope stage on the radiation shield at liquid nitrogen temperature to reduce noise (by reducing the cable capacitance C_c in Fig. 4.3b). The deflection signal is further enhanced by an external Stanford Research System amplifier with gain $2 \cdot 10^1$ and filtered by a band-pass filter (10 – 100 kHz). Alternatively to the internal fixed-gain current amplifier, an external Femto amplifier (gain $10^6 - 10^9$) can be used if higher currents or higher bandwidth are required.

4. UHV chamber and low-temperature STM/AFM

The microscope is controlled by homebuilt electronics and software. The analog electronic components are connected to a digital signal processing unit (DSP) by 18bit analog-to-digital and 20bit digital-to-analog converters. The phase-locked-loop (PLL) (see chapter 3) is entirely software-based and runs on a separate DSP board. According to Giessibl^{65,76}, the main sources for frequency noise are thermal noise and detector noise. Both noise sources scale with bandwidth and can be therefore significantly reduced by slower scan speeds. In the high-resolution AFM measurements discussed in part III the scan speed is smaller than 12 \AA s^{-1} . Note however, that the initial sample characterization and tip preparation are done in STM mode with much higher scan speeds. Typically stable AFM operation could be maintained with oscillation amplitudes down to about 0.1 \AA with a noise floor of 20 mHz and constant current STM feedback operation with tunneling currents of about 1 pA . The oscillation amplitude was chosen to be $0.4 - 0.5 \text{ \AA}$, which is a trade-off between sensitivity to short-range forces and increasing noise with smaller amplitude.

To calibrate the oscillation amplitude of the sensor, it was oscillated with a large amplitude and with enabled STM constant current feedback. For large amplitudes, the average tunneling current will be dominated by the contributions when the tip is in the lower turning point of the oscillation, because of the exponential decay of the tunneling current with distance. Therefore a change in the AFM amplitude set point will linearly change the STM tip height, which directly reflects the change in the real oscillation amplitude. The slope of the fitted line to the measured change in tip height yields the desired conversion factor between the amplitude set point (in arbitrary units) and the real oscillation amplitude.

4.2. Scan parameters and methods

All STM images, shown throughout this thesis, were acquired in constant current mode using a constant voltage V applied to the sample electrode and the tip on (virtual) ground. The STM image corresponds then to the tip height to maintain a predefined current I . The AFM is operated in frequency modulation mode³² at constant height. If not stated otherwise, the AFM images were acquired with an oscillation amplitude of $A = 0.5 \text{ \AA}$ at $V = 0 \text{ V}$. To ensure low noise operation in the Δf signal even at sub-Ångström amplitudes, the PLL is set to very small bandwidths ($\lesssim 10 \text{ Hz}$) and accordingly the tip has to be scanned

very slowly during AFM operation (typically about $5 - 12 \text{ \AA s}^{-1}$). The scan height is usually defined as an offset z with respect to the constant current set-point (I, V) and positive offsets correspond to a distance decrease. In sections 7.1, 7.2, 7.3 and 9.1.2 different conventions for z were used to enable a quantitative comparison of the absolute tip height with theory and other experimental methods. In these sections z directly reflects the distance between the last tip atom and the molecular plane (sections 7.1, 7.2 and 9.1.2) or the distance to the Δf minimum above the substrate plane (section 7.3). Thus z decreases with decreasing distance.

KPFM maps are obtained by recording $\Delta f(V)$ spectra on a lateral grid point-by-point on a plane parallel to the surface⁴⁰. After each spectrum, the tip moved back to a reference point where the constant-current feedback is switched on again for a couple of seconds to compensate for vertical drift. Lateral drift was compensated for maps taking longer than one hour by cross-correlating a STM image with a reference image. Three-dimensional (3D) forcemaps were acquired in an analogous manner to KPFM maps but recording the $\Delta f(z)$ instead of the $\Delta f(V)$ dependence⁷⁷.

CHAPTER 5

Sample system NaCl(2ML)/Cu(111)

In recent years, ultrathin insulating films on metal substrates have gained appreciable attention as templates for the study of individual adsorbates^{17,22,26,30,58}. This attention stems from both the decoupling of the adsorbate electronic states from the metal substrate and the chemically inert adsorbate–film interaction, which makes it possible to study single molecules and atoms close to their native state. For all measurements presented in this thesis we used a Cu(111) single crystal with a submonolayer coverage of bilayer NaCl to study single adsorbates and defects on a metal and thin insulating film.

5.1. Sample and tip preparation

First, the Cu(111) crystal is cleaned by several cycles of Ne⁺ sputtering (20 min at 1 keV) and short annealing periods at 870 K. Next, the Cu sample is cooled to 270 K (using the manipulator) and submonolayer coverage of NaCl are deposited from a Ta crucible at a rate of ≈ 2 ML/min monitored with quartz crystal microbalance. These growth conditions lead to the formation of (100)-oriented μm -sized islands of NaCl, with a thickness of predominately two atomic layers^{78,79}. The sample is then transferred into the liquid Helium cooled microscope. The adsorbates to be studied are thermally evaporated *in situ* through small holes in the radiation shields onto the sample at 10 K. In this way, desorption or thermal diffusion is suppressed and the adsorbates will remain at their initial adsorption sites. To deposit organic molecules (that are in solid phase under ambient conditions), a two-step process is usually used. The molecules are first sublimed onto a piece of Si wafer in the load-lock chamber and the deposition rate monitored by a quartz crystal microbalance. Then, the Si wafer is flash-heated by direct, resistive heating to about 900 K in front of small holes in the radiation shields in the microscope chamber. The advantage of this approach is twofold: The deposition quantity can be accurately controlled and the preparation is very clean because one

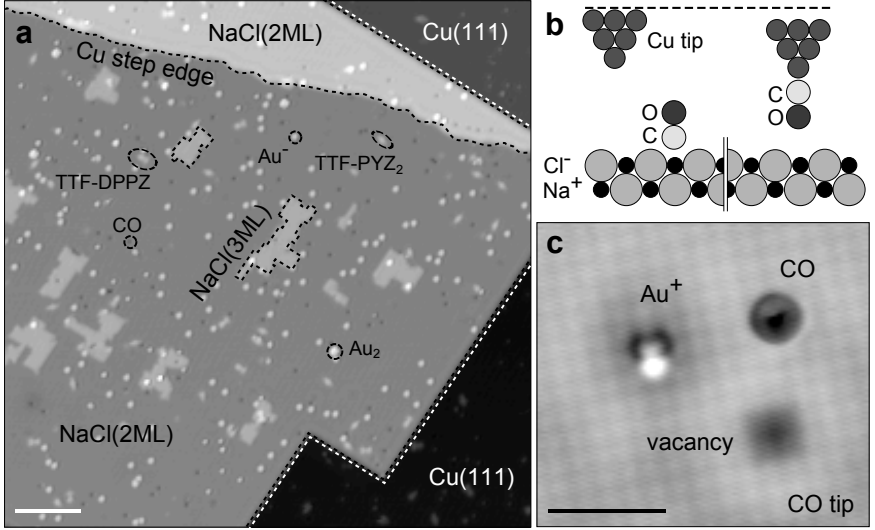


Figure 5.1.: **NaCl(2ML)/Cu(111)**. **a** Constant-current STM overview image ($I = 2 \text{ pA}$, $V = 0.2 \text{ V}$) of a (100)-oriented NaCl bilayer island (with patches of third layer on top) grown on a Cu(111) single crystal. Several adatoms and molecules have been deposited *in situ* on the sample at 10 K. The different adsorbates can be distinguished by their characteristic appearance in the STM topography. **b** Schematic of a Cu tip above the NaCl surface (left) and after picking up the CO (right). To maintain a certain tunneling set point the CO terminated tip has to approach the surface, indicated by the dashed line. **c** Typical STM topography ($I = 2 \text{ pA}$, $V = 0.2 \text{ V}$) recorded with a CO tip. Here, a Au^+ adatom, CO molecule and Na vacancy on NaCl(2ML)/Cu(111) are shown. The STM resolution and appearance is characteristically dependent on the tip termination (see chapter 6). Scale bars: 100 \AA in **a** and 20 \AA in **c**.

selectively removes contaminants with higher or lower sublimation temperature. If the available substance amount is very low ($\sim \mu\text{g}$), the substance can also be directly spread on the Si wafer and flash-heated. To deposit gaseous compounds (such as CO or Xe) on the surface, small pressures ($\sim 10^{-8} \text{ mbar}$) of the gas are admitted to the UHV chamber and the shutters to the sample are opened for a few seconds. This procedure is then repeated until a sufficient amount is deposited. Metal adatoms (such as Au) are prepared by heating a Ta spiral surrounding a piece of the metal until it becomes liquid and a small amount of atoms are evaporated through the holes in the radiation shields. In Fig. 5.1a a typical STM overview image of a bilayer NaCl island on Cu(111) [NaCl(2ML)/Cu(111)] is shown with several adsorbates on top.

5. Sample system NaCl(2ML)/Cu(111)

As a tip we use a $25\,\mu\text{m}$ thin PtIr wire, which is glued to the quartz cantilever. *Ex situ* the tip is shortened and sharpened by focused-ion-beam (FIB) (see Fig. 4.2c). After mounting the tip in the microscope, it is repeatedly indented into the Cu substrate until a sharp and stable tip is formed. The quality of the tip can be checked by several criteria: (i) Small negative frequency shift ($\Delta f \approx -2\text{Hz}$ at a tunnel set point of $I = 2\text{pA}$ at $V = 0.2\text{V}$), (ii) circular and high STM contrast of adsorbates and (iii) no instabilities or unidentifiable features in the $I(V)$ spectrum. We selectively choose tips that comply with all these criteria. The resulting sharp metal tip is most likely covered with Cu and in the following referred to as Cu tip. Starting from such a Cu tip, the tip can be functionalized by controlled modifications of the tip apex (frontmost atom/molecule). The functionalization is achieved by picking up (vertically manipulating) the desired tip termination from the surface⁶. Depending on the specific species this can require some intermediate steps (see chapter 6). In Fig. 5.1b the tip functionalization is schematically depicted for CO. The tip above the CO on NaCl(2ML)/Cu(111) is approached by 2.5\AA from the STM set-point ($I = 2\text{pA}, V = 0.2\text{V}$). The transfer is noted by a sudden decrease in the tunneling current, resulting in smaller scan height when the STM feedback is switched on again (dashed line in Fig. 5.1b). The CO tip exhibits a characteristic contrast of adsorbates along with an increase in resolution compared to metal tips as seen in Fig. 5.1c. For further details on different tip functionalizations and their performance for STM, AFM and KPFM, please see chapter 6.

If not explicitly stated, STM images and KPFM maps were obtained with Cu tips and AFM images and three-dimensional forcemaps with CO tips.

Part III.

Results

CHAPTER 6

Effects of tip functionalization in SPM

Most of the content presented in this chapter has been published in Applied Physical Letters ^a80. Text excerpts and figures are reproduced by permission of AIP Publishing.

The fundamental importance of the geometrical structure and composition of the tip apex on the contrast in scanning probe microscopy is a commonly known fact. Specifically in STM many different approaches have been developed to modify, control and identify the tip apex. The tips are often modified by applying voltage pulses, scanning at small tip-sample distances, or even crashing the tip deliberately into the sample. These preparation procedures are effective but the outcome is based on chance, often not reproducible and the resulting atomic structure of the tip is usually not known exactly. Since the demonstration of controlled vertical manipulation by Eigler *et al.*⁶ it is possible to terminate the tip with individual atoms or molecules picked up from the sample surface in a defined way, referred to as tip functionalization. Early on it was noticed that picking up single Xe atoms^{6,81,82} or CO molecules^{9,83} from a metal substrate enhance the resolution in STM imaging of surfaces and adsorbates. More recently, it was found that ultrahigh resolution of the geometrical structure of ad-molecules can be achieved with STM by bringing molecular hydrogen into the tunneling junction⁸⁴, and the method was then also extended towards other tip terminations⁸⁵ (Xe, CO, and CH₄). In AFM, the preparation and characterization of the tip are even more difficult than in STM, and consequently, the structure and chemical composition of the tip can often only be inferred indirectly by comparison with density functional theory (DFT) simulations^{36,86} or from symmetry arguments^{42,87}. Low-temperature scanning probe systems that offer the possibility of simultaneous STM and AFM operation enable the use of the established STM tip preparation techniques

^aMohn, F., Schuler, B., Gross, L. & Meyer, G. Different tips for high-resolution atomic force microscopy and scanning tunneling microscopy of single molecules. *Appl. Phys. Lett.* **102**, 073109 (2013)

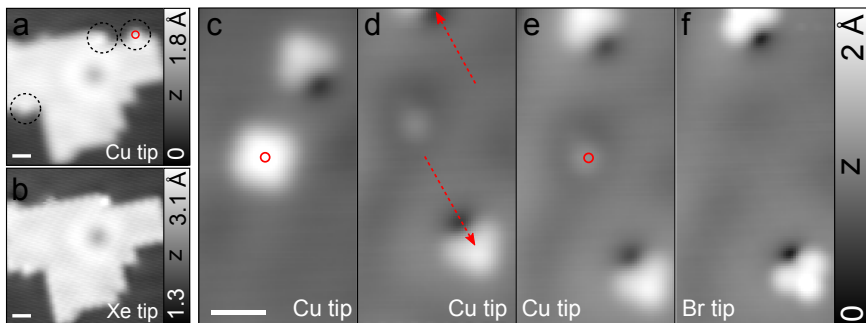


Figure 6.1.: **Tip functionalization with Xe or Br.** **a,b** STM topographies ($I = 2$ pA, $V = 0.2$ V) of a small patch of NaCl(3ML)/Cu(111). Individual Xe atoms (indicated by dashed circles) at the island edge can be picked up by approaching the tip by 3 Å. **b** After picking up a Xe atom (position of the red circle in **a**) the resolution is increased. **c,d** STM topographies ($I = 2$ pA, $V = 0.2$ V) of DBA on NaCl(2ML)/Cu(111) before (**c**) and after (**d**) applying a voltage pulse of 1.65 V at the position indicated by the red circle. **e,f** STM topographies ($I = 2$ pA, $V = 0.2$ V) before (**e**) and after (**f**) pick up of a Br atom by approaching the tip by 4 Å at the position indicated by the red circle. Scale bars: 10 Å.

in AFM experiments on conducting substrates. In the following it is described how tips terminated with single Cl, Br, I, Xe or Kr atoms or with a single CO or NO molecule can be created in experiments on thin insulating films, and we explore the usefulness of these tips for STM and AFM imaging of single molecules. In section 6.3, the AFM and KPFM contrast of a Cl vacancy is examined by means of different tip terminations. Thereby, the underlying contrast mechanisms of AFM and KPFM on ionic surfaces could be resolved.

6.1. Tip functionalization by controlled vertical manipulation

Adsorbate pick-up from the surface. To terminate the tip with Xe, Kr, CO and NO, low coverages (≈ 0.01 nm $^{-2}$) of the compounds are deposited on the surface at $T \approx 10$ K by admitting these gases into the UHV chamber ($p \approx 5 \times 10^{-8}$ mbar) and opening a shutter to the microscope stage for a few seconds. Prior to the tip functionalization the tip is repeatedly indented into the Cu substrate until a stable and sharp tip has formed as described in section 5.1. Thereafter, the tip is positioned on an adatom or admolecule on the NaCl(2ML) film and approached at about 10 mV by a

6. Effects of tip functionalization in SPM

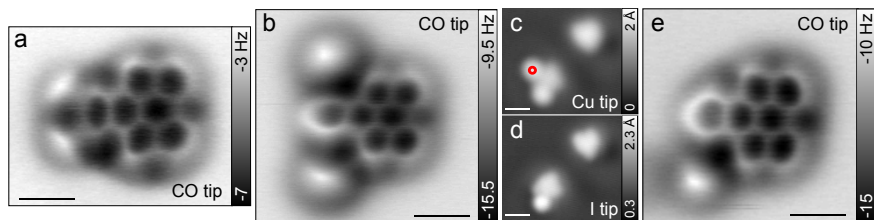


Figure 6.2: **Tip functionalization with I.** **a,b** AFM maps of DINP before (**a**), and after (**b**) dissociating the two iodine atoms by a voltage pulse of 1.7 V imaged with a CO tip. **c,d** STM image before (**c**) and after (**d**) picking up one I atom next to the arylene molecule at the position of the red circle. At the upper right there is another arylene molecule without I next to it. **e** AFM image with a CO tip after the I was picked up. Scale bars: 5 Å in **a,b,e** and 10 Å in **c,d**.

few Ångströms from a STM set point of 2 pA at 0.2 V. The transfer of the adsorbate to the tip is noticed by a sudden jump in the tunneling current and frequency shift. The successful tip termination and quality of the tip (like its spherical symmetry) can be verified by the characteristic contrast change of different adsorbates in STM. This procedure is illustrated for Xe in Fig. 6.1a,b. In Fig. 6.1a several protrusions at the edge of a 3ML NaCl island can be distinguished (black dashed circles), which can be attributed to single Xe atoms. After picking up one of them by approaching the tip by 3 Å at the position indicated by the red circle, the STM imaging contrast is significantly enhanced (Fig. 6.1b), similarly to when a Xe atom is picked up from a Cu step edge⁶. It should be noted that between panels **a** and **b** of Fig. 6.1, the tip height corresponding to the STM set point above the substrate changed by about 1.3 Å: That is, the tip appeared to be longer by that length after pick up of the Xe atom, which is reflected in the different topography scales of the two images.

Tip functionalization by means of vertical manipulation is very powerful because the imaging capabilities on the atomic scale strongly depend on the terminating atom and only to a minor extent on the uncontrollable metallic tip apex behind the frontmost atom.

Molecule precursor dissociation and extraction from the crystalline substrate. Functionalizing the tip by directly adsorbing the desired termination on the surface and subsequent pick up is appealing by its simplicity. Though, there might be circumstances where this procedure is impractical; For example if the desired species is difficult to prepare because it is hazardous or corrosive. This is for example the case for

halogenides. In such cases, an alternative approach is desirable. One alternative way is the extraction of atoms from a crystalline surface such as Cl from a NaCl film³⁸. This can be achieved by either bringing the tip in controlled contact with the NaCl surface, thereby transferring a Cl atom to the tip apex and generating a Cl vacancy (see also section 6.3). Or a Cl tip can be produced by picking up a Au adatom with negative sample voltage applied, which often results in a transfer of a Au-Cl complex to the tip⁸⁸. A more versatile method is the dissociation of the target tip termination from a molecule precursor. In Fig. 6.1c-f, the creation of a Br-terminated tip is shown. Because of its low sublimation temperature and its highly corrosive properties, Br cannot be easily deposited onto the sample surface. Therefore, we evaporated suitable brominated molecules such as dibromoanthracene (DBA) onto the NaCl(2ML)/Cu(111) surface. By STM manipulation it was possible to dissociate single Br atoms from these molecules, which could then be picked up with the tip to create a Br-terminated tip. Fig. 6.1c shows two DBA molecules, from one of which a Br atom has already been dissociated. The tip was positioned above the intact molecule, and a sample bias voltage of 1.65 V was applied. This led to a dissociation of one of the Br atoms from the molecule: The subsequent STM image (Fig. 6.1d) shows a small circularly shaped unit at the former location of the intact DBA molecule. The remainder of the molecule as well as the other nearby molecule both changed their position during the dissociation, as indicated by the red dashed arrows. High-resolution AFM imaging (e.g., with a CO-terminated tip) of dissociated molecules confirmed that the small circular protrusion is a single Br atom dissociated from the molecule (see section 9.1.2). The molecule now shows a dark depression at the former position of the dissociated Br atom. Also the second Br atom could be detached in a similar fashion. The dissociated Br atom could easily be picked up from the surface by approaching the tip by 4 Å from the STM set point height, as shown in Fig. 6.1e,f. As can be seen in Fig. 6.1f, the transfer of the Br atom to the tip apex is immediately recognized by an enhancement of the STM contrast.

As bromine also iodine is in its elemental form toxic and corrosive and hence one tries to circumvent its usage in UVH chambers if possible. Analogously to a Br tip, an iodine terminated tip could be created by dissociating I from diiodonaphtho-erylene (DINP), presented in Fig. 6.2. In Fig. 6.2a an intact DINP precursor molecule is imaged with a CO tip. After applying a voltage pulse of 1.7 V both I atoms were dissociated from the molecule and adsorbed in its direct vicinity as seen in Fig. 6.2b and c. The dissociation

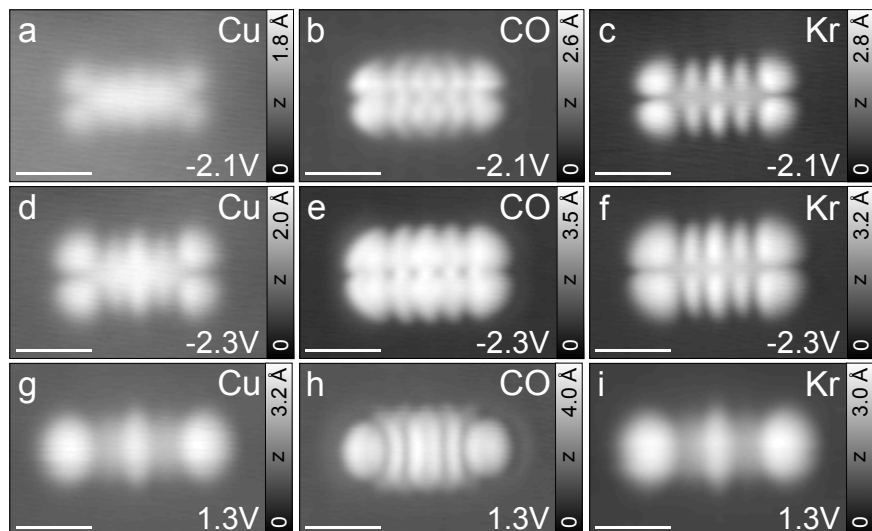


Figure 6.3.: **STM performance.** **a-i** STM topographies of the HOMO (**a-f**) and LUMO (**g-i**) resonance of a pentacene molecule on NaCl(2ML)/Cu(111) recorded with a Cu tip (**a,d,g**), CO tip (**b,e,h**) and Kr tip (**c,f,i**). Scale bars: 10 Å.

product aryne will be discussed in detail in section 9.1.1. The I atoms could be easily picked up to terminate the Cu tip. The I tip as well enhanced the STM resolution greatly and appeared to elongate the tip by about 0.2–1 Å. The vertical manipulation of an I atom next to the molecule did not affect the remainder molecule next to it as seen in Fig. 6.2e.

6.2. Performance of different tips for STM and AFM

In this section we assess the performance of Cl, Br, I, Xe, Kr, CO and NO tips for high-resolution STM and AFM imaging of molecules. Generally, Cl/Br/I or Xe/Kr tips have very similar imaging characteristics in both STM and AFM. Though, Br and Xe tips turn out to be more stable than their halogen and noble gas counterparts. Interestingly, the NO tip behaves quite differently from the CO tip, confirming the influence of the second-frontmost tip atom on the imaging contrast predicted by Guo *et al.*⁸⁹. The NO tip is usually less stable and atomic-resolution AFM images of molecules appear less distorted than with a CO tip.

In Fig. 6.3 the negative and positive ion resonance corresponding to the frontier molecular orbitals of pentacene recorded with a Cu, CO and Kr tip are depicted. In comparison to the metal tip (Fig. 6.3d), both CO (Fig. 6.3e) and Kr tips (Fig. 6.3f) increase the spatial resolution. In particular, the observed contrast differences between the tips and even for the same tip depend on the applied bias. The CO tip has considerable contribution from electrons tunneling through the $2\pi^*$ orbitals of the CO tip molecule that have p -wave symmetry⁴¹. According to Chen’s derivative rule⁹⁰ such a p -wave tip in resonance with a sample molecule orbital correspond to the modulus squared of the lateral gradient of that orbital. The contribution of these p -wave electrons to the tunneling current is bias dependent. At the onset of the sample molecular orbital, the orbital image is dominated by these p -wave contributions due to the symmetry dependence of vibration-assisted tunneling⁹¹. Consequently, at the onset of the pentacene HOMO (Fig. 6.3b) the orbital image with a CO tip resemble the lateral derivative of the HOMO with enhanced tunneling at HOMO nodal planes. On the resonance maximum (Fig. 6.3e), however, s -wave electrons contribute and the HOMO topography has mixed s - and p -wave portions. Metal and noble gas tips are predominately s -wave tips, since these states expand further into the vacuum^{61,62}, hence these tips directly reflect the real-space structure of the molecular orbital.

For AFM molecular structure imaging the CO tip excels with its high lateral resolution mainly as a consequence of the sideways tilting of the CO tip molecule that will be discussed in detail in sections 7.1 and 7.2. Monoatomic tips such as Cl, Br or Xe yield a lower resolution, but the images of polyaromatic hydrocarbons are less distorted compared to images recorded with a CO tip^{38a}. In Fig. 6.4 AFM images of DBA and dibenzonaphthoperylene (DBNP)⁹² obtained with a Br, Cl, Xe or CO tip are shown. The Cl and Br terminated tips yield an identical contrast on the DBA molecule (Fig. 6.4a,b) despite the larger covalent radius of Br. Irrespective of this similarity, the Br tip has the advantage that it is easier to prepare, because the Br atom lying atop the NaCl surface does not need to be extracted from the crystalline NaCl like the previously used Cl tip. As an interesting side note, Br and I tips were also found to be well suited for lateral manipulation of single molecules on NaCl(2ML)/Cu(111) in the pulling mode, which is usually difficult to achieve on this substrate⁹³.

^aRecent results with Xe tips obtained in the group of Ingmar Swart, however, indicated also strong distortions at close distance. Note that these measurements were taken on a different substrate.

6. Effects of tip functionalization in SPM

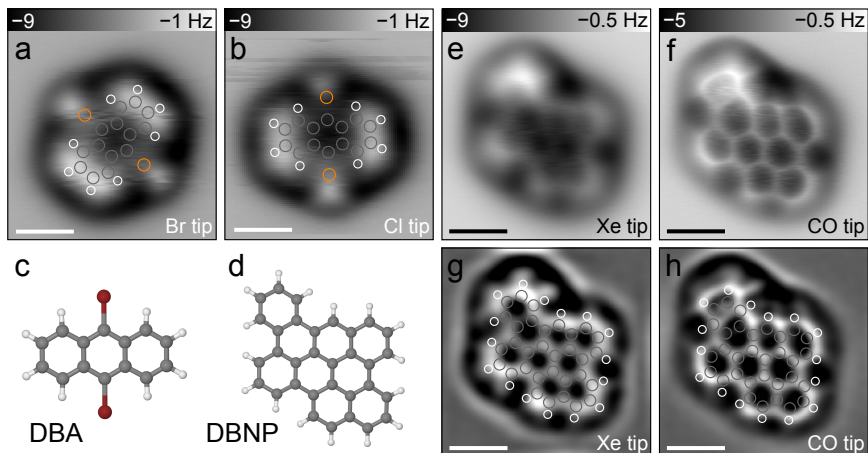


Figure 6.4.: **AFM performance.** **a,b** AFM image of DBA on NaCl(2ML)/Cu(111) recorded with a Br tip (**a**) and Cl tip (**b**). **c,d** Molecule model of DBA (**c**) and DBNP (**d**). **e,f** AFM image of DBNP on NaCl(2ML)/Cu(111) recorded with a Xe tip (**e**) and CO tip (**f**). **g,h** Laplace and low-pass filtered versions of **e** and **f** with atomic positions overlaid. Scale bars: 5 Å.

The Xe tip used in Fig. 6.4e exhibits a faint atomic resolution, but the chemical structure of the molecule is more obvious in the CO tip image (Fig. 6.4f). On the other hand, the Xe tip image is much less distorted, as can be seen in the Laplace and low-pass filtered images shown in Fig. 6.4g,h.

In conclusion, we have found that a number of different tip terminations can be prepared by picking up single adsorbates from NaCl(2ML)/Cu(111), which were either directly adsorbed, extracted from the substrate or dissociated from a molecule precursor. The performance of these tips in STM and AFM imaging of single molecules were assessed. We found the Br tip to be particularly useful for undistorted AFM imaging of single molecules and lateral manipulation (along with I), and the Xe tip for STM orbital imaging. The combined information from images recorded with different tips could in the future facilitate the extraction of information about the chemical composition of the imaged molecules.

6.3. AFM and KPFM contrast on ionic surfaces with different tips

Most of the content presented in this section has been published in Physical Review B^{a94}. Text excerpts and figures are reproduced by permission of the American Physical Society.

In the previous sections, empirical recipes for different tip functionalizations were given and their performance for STM and AFM on molecules was evaluated. Despite AFM and KPFM have evolved into important tools for nanotechnology, their contrast mechanisms on the atomic scale are not entirely understood. Next we try to understand the atomic contrast on Cl vacancies in NaCl as a function of bias voltage, tip height, and tip functionalization. It is demonstrated that the AFM contrast qualitatively depends on both tip termination and sample voltage, and with the aid of density functional theory we reveal the underlying contrast mechanisms. LCPD maps acquired with KPFM showed the same qualitative contrast for all tip terminations investigated, resembling the electrostatic field of the sample.

With force-voltage spectroscopy, which represents a method of KPFM, charge states of single atoms³¹, defects⁹⁵, and molecules⁹⁶ were determined, and the charge distribution in a molecule was imaged⁷⁷. The atomic contrast observed with KPFM^{87,97–100} triggered efforts to explain the underlying contrast mechanism theoretically^{101,102}. The most important open questions are: What are the physical properties mapped by AFM and KPFM on the atomic scale, and how can we take advantage of this information?

The (100) surfaces of alkali halides are often used as model systems to investigate atomic contrast on insulators by AFM^{103–107}, and theory predicted that the polarity of the tip apex determines whether the largest attractive forces are measured above anions or cations¹⁰⁸. Here we used Cl vacancies in the top layer of a bilayer of NaCl(100) on Cu(111) as model systems¹⁰⁹ to study the atomic contrast of AFM and KPFM on ionic systems employing five different tips terminated with individual Cu, Au,

^aGross, L., Schuler B., Mohn, F., Moll, N., Pavliček, N., Steurer, W., Scivetti., I., Kotsis, K., Persson, M. & Meyer, G. Investigating atomic contrast in atomic force microscopy and Kelvin probe force microscopy on ionic systems using functionalized tips. *Phys. Rev. B* **90**, 155455 (2014).

6. Effects of tip functionalization in SPM

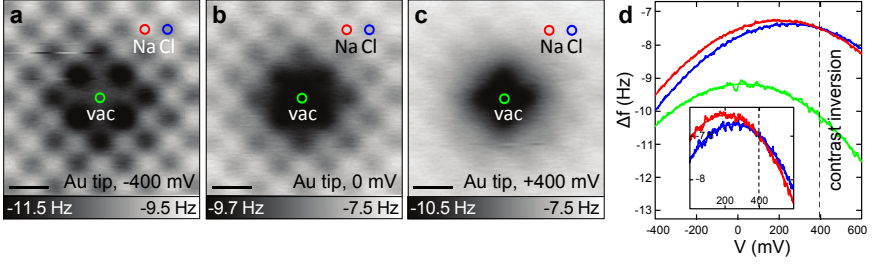


Figure 6.5.: **AFM contrast inversion on NaCl with Au tips.** **a-c** AFM images of a Cl vacancy at different voltages V with a Au tip. **d** $\Delta f(V)$ spectra at the locations indicated by the circles in **a-c** measured with another Au tip. Red: Na site, Blue: Cl site, Green: Vacancy site. For $V > 400$ mV the Δf contrast between Na and Cl sites is inverted. The inset shows a close-up of the cross-over region. Scale bars: 5 Å.

Cl, I and Xe atoms. We demonstrate true atomic resolution with AFM and KPFM for all five tip functionalizations investigated. We found that the AFM contrast does depend crucially on the sample bias and the tip termination, whereas the LCPD does not. The AFM contrast arises mainly from electrostatic interactions but it cannot always be explained by the tip polarity alone.

The vacancies were created by bringing the Cu tip into controlled contact with the NaCl surface. Thereby a Cl atom is transferred to the tip apex, as evidenced by a characteristic contrast change in STM images (as the Cl atom remains on the tip apex) and a remaining depression at the predefined Cl site. Alternatively, Cl vacancies can be produced by field-emission from the tip or picking-up a Au adatom with negative sample voltage applied, which often leads to an individual Cl vacancy being created¹⁰⁹.

AFM images with an Au-terminated tip (Au tip) at different sample voltages V are shown in Fig. 6.5. Note that the Cl vacancy unambiguously indicates the location of the Na and Cl sites. It can be observed that the Cl sites exhibit a smaller (more negative) frequency shift Δf than the Na sites. This corresponds to a larger attraction above the Cl sites than above the Na sites, in agreement with an investigation by Teobaldi *et al.* using metal tips¹¹⁰. We observed that the atomic contrast crucially depended on V : With increasing V , the contrast between Cl and Na sites decreased and the vacancy site appeared darker (more attractive) than the Na and Cl sites. At $V = -400$ mV (Fig. 6.5a), the sites exhibiting the smallest Δf

6.3. AFM and KPFM contrast on ionic surfaces with different tips

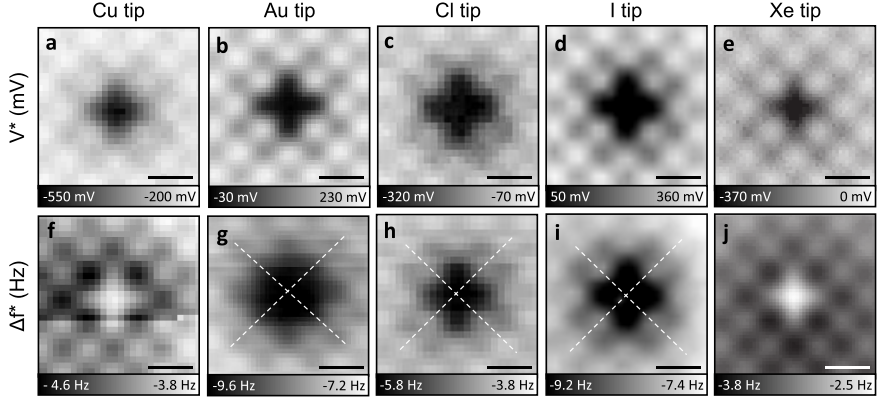


Figure 6.6.: **KPFM contrast of the Cl vacancy for different tips.** **a-e** LCPD maps of a Cl vacancy using different tips: Cu tip (**a**), Au tip (**b**), Cl tip (**c**), I tip (**d**) and Xe tip (**e**). **f-j** Corresponding Δf^* maps. The white dashed lines indicate Cl rows. The contrast change in **f** is probably caused by a slight rearrangement of the Cu tip atoms. Note that this had little effect on the simultaneously measured V^* map (**a**). Scale bars: 5 Å.

are the four neighboring Cl sites of the vacancy, whereas at $V = +400$ mV (Fig. 6.5c) the vacancy site itself and its four neighboring Na sites exhibit the smallest Δf . Using another Au tip we even observed a Δf contrast inversion between Na and Cl sites at around +400 mV (see Fig. 6.5d). This demonstrates the importance of taking into account the V -dependence, in addition to the tip termination and the z -dependence in AFM images.

In the following we investigate the effect of different tip terminations on the Δf contrast at the LCPD compensated voltage V^* , which minimizes the electrostatic force contribution. To this end, we measured maps of V^* and Δf^* by acquiring $\Delta f(V)$ spectra on a grid (as described in section 3.2), shown in Fig. 6.6. For all tips we obtained atomic resolution in both the V^* and the Δf^* channel. The V^* maps of all tips (Fig. 6.6a-e) appear very similar. Not only is the V^* contrast of the Na, Cl and vacancy (vac) sites similar, but also the shift of V^* towards greater negative values above the four neighboring Na sites of the vacancy is exhibited by all tips. As a result the vacancy appears in the shape of a dark cross in all V^* maps. The absolute V^* level is different in each image because of the influence of the mesoscopic tip shape (cf. section 3.2). On the other hand, the Δf^* maps (Fig. 6.6f-j) show qualitatively different contrasts.

6. Effects of tip functionalization in SPM

All measured V^* maps are in qualitative agreement with the z -component of the electrostatic field (E_z) above the sample (for further details see Ref. 94). This relation can be understood as follows: To compensate for the electrostatic field at the tip position, a matching external field with opposing polarity has to be applied. However, also the mesoscopic parts of tip and sample contribute to the electrostatic field and thus to V^* . Because of the aforementioned averaging effects (see section 3.2) we cannot quantitatively recover the electrostatic field from V^* .

The atomic tip termination obviously plays an important role for the explanation of the Δf^* contrast. As Fig. 6.6 was obtained in the attractive branch of Δf and we also see no contrast inversions as a function of z , we can rule out significant contributions of Pauli repulsive forces here. Van der Waals forces will contribute, but cannot be responsible for the tip-dependent contrast inversions we observed, in particular not for the large attraction above the vacancy for the Au, Cl and I tip.

As detailed in Ref. 94, a thorough analysis of the $\Delta f(V, x, y, z)$ data reveals which electrostatic force contribution is responsible for the V^* and Δf^* contrast: The horizontal shift of the $\Delta f(V)$ parabola, and hence the V^* contrast, is caused by the interaction between localized (V independent) charges at the sample and the homogeneous charge distribution in the tip in response to the applied bias and different work functions. This interaction exhibits a linear V dependence. The Δf^* contrast on the other hand results mainly from the interaction between the localized charges of the tip and sample that are V independent. Localized charges of the sample stem from the ions and the vacancy. The localized charges at the tip, in particular, a tip dipole, arise from the tip shape because of the Smoluchowski effect^{110,111} and, additionally, from the tip functionalization. We modeled tips as Cu clusters with different atomic tip functionalizations and obtained dipole moments of $p_{\text{Cu}} \approx +0.5 \text{ D}$, $p_{\text{Au}} \approx -1 \text{ D}$, $p_{\text{Cl}} \approx -7 \text{ D}$, and $p_{\text{Xe}} \approx +3 \text{ D}$, with positive p corresponding to a positive partial charge at the tip apex. The I tip can be assumed to show the same sign for p as the Cl tip. The measured Δf^* contrast of the Cu, Cl, I and Xe tips can be understood from their respective dipole moments: The attraction is increased above sample charges of opposite sign with respect to the tip apex for these four tips.

The Au tip demonstrates that the Δf^* contrast in general cannot be

6.3. AFM and KPFM contrast on ionic surfaces with different tips

explained by the dipole moment of the isolated tip. The Au tip exhibits a larger attraction on both the Cl and the vacancy site than on the Na site, although Cl is charged negatively and the vacancy is charged more positively as compared to Na. Two effects could play a role here: First, the uncompensated positive charge of the vacancy will induce a negative image charge in the tip, thus changing the tip dipole with the tip position. Second, the charge distributions of tip and sample are more complex than the simple picture of point charges or dipoles. In particular, the lateral charge distribution at the tip due to the tip functionalization and the Smoluchowski effect should be taken into account.

Using tip functionalization by atomic manipulation we clarified the properties and the origin of AFM and KPFM contrast on the atomic scale: We found almost no tip dependence of the relative contrast in the V^* (LCPD) measured with KPFM, but a very pronounced tip- and voltage-dependence for AFM. Remarkably, electrostatic forces are the main contributions in all cases. The V^* channel reflects E_z above the sample. The AFM contrast at compensated LCPD depends crucially on the tip because of the direct electrostatic interaction of localized, voltage independent tip and sample charges.

CHAPTER 7

Molecular properties measured by AFM

For any interpretation of AFM data, understanding of the contrast mechanism is crucial. At first glance, the atomically resolved AFM images as the one shown in Fig. 6.4f being similar to the molecular structure, suggest that the contrast simply reflects the geometry of the molecule. However, the imaging mechanism is far from being simple. First, the AFM signal is composed of several different types of interactions, such as electrostatic forces, van der Waals attraction, chemical bond formation, and Pauli repulsion. Additionally, as these forces act on very different length scales, different parts of the tip and sample structure may contribute to the imaging process. In this chapter we will discuss how the different aforementioned contributions can be used to gain qualitative and quantitative information about important molecular properties. In section 7.1, we investigate the AFM contrast associated with Pauli repulsion that comprises information about the bond order of single bonds. Then, image distortions stemming from CO tip relaxations are analyzed in detail and its main source is uncovered. In section 7.3, we present a method to quantify the adsorption geometry of molecules. In the last section of this chapter, electrostatic force contributions are extracted by KPFM to study the charge distribution of molecules.

7.1. Bond-order discrimination

Most of the content presented in this section has been published in Science^{a112}. Text excerpts and figures are reproduced by permission of the American Association for the Advancement of Science.

Bond order is an important concept to predict geometry, stability, aromaticity, reactivity, and electronic structure of covalently bonded

^aGross, L., Mohn, F., Moll, N., Schuler, B., Criado, A., Guitián, E., Peña, D., Gourdon, A. & Meyer, G. Bond-order discrimination by atomic force microscopy. *Science* **337**, 1326-1329 (2012)

molecules. The bond order is closely related to the bond length, which, in general, decreases with increasing Pauling bond order^{113,114}. If single crystals are available, the bond length can be determined experimentally with high accuracy using diffraction methods, which – for instance, in the case of fullerenes (C_{60}), as predicted by Clar’s sextet theory – showed two kinds of bonds of different lengths^{115–118}. In contrast to diffraction based techniques, which yield values averaged over large ensembles of molecules, scanning probe microscopy offers the possibility of studying single bonds in individual molecules. For molecules, not only the chemical species of their constituent atoms can differ, but also the coordination number of atoms, the bond angles, bond order, and bond length. In polycyclic aromatic hydrocarbons (PAHs), the differences in bond order and length are subtle due to the delocalized π -electrons that render the number of electrons participating in a bond non-quantized. However, detecting these small differences is useful for rationalizing aromaticity and reactivity of such molecules¹¹⁹. AFM offers the possibility of studying systems in which single crystals needed for diffraction methods cannot be grown. Moreover, bond-order determination within individual molecules is desirable for chemical structure determination³⁹, the investigation of isomerization reactions where bond order changes^{120,121}, and the characterization of structural relaxations around atomic defects in graphene^{122–124}.

Here, an AFM method to differentiate bond orders and lengths of individual bonds for C_{60} and large PAHs is demonstrated and C-C bonds parallel to the sample surface are investigated. Hence, differences in contrast arising from the chemical species of the atoms^{39,89}, polarity of the bonds or variations of the tip-sample separation (nonplanar adsorption geometries, see section 7.3)^{125,126} can be neglected. In a C_{60} molecule, the bonds fusing two hexagons (h) are electron-rich compared with the bonds fusing a pentagon and a hexagon (p) (Fig. 7.1e). The Pauling bond order P_b of a bond b in a conjugated molecule is found by counting the number of Kekulé structures (classical resonance formulas) that show b as a double bond divided by the total number of different Kekulé structures of the molecule^{113,114}. Thus, P_b can take values between 0 (single bond) and 1 (double bond); in the case of C_{60} , the Pauling bond orders are $P_h = 0.44$ and $P_p = 0.28$, respectively¹²⁷. Correspondingly, theoretical¹²⁸ and experimental investigations using neutron diffraction¹¹⁵, electron diffraction¹¹⁶, and x-ray diffraction^{117,118} have shown that the bond h is shorter than the bond p by $\sim 5\%$. The measured bond lengths are $L_h = 1.38(2) \text{ \AA}$ and $L_p = 1.454(12) \text{ \AA}$, respectively. The exact molecular adsorption orientation of C_{60} on Cu(111) was determined

7. Molecular properties measured by AFM

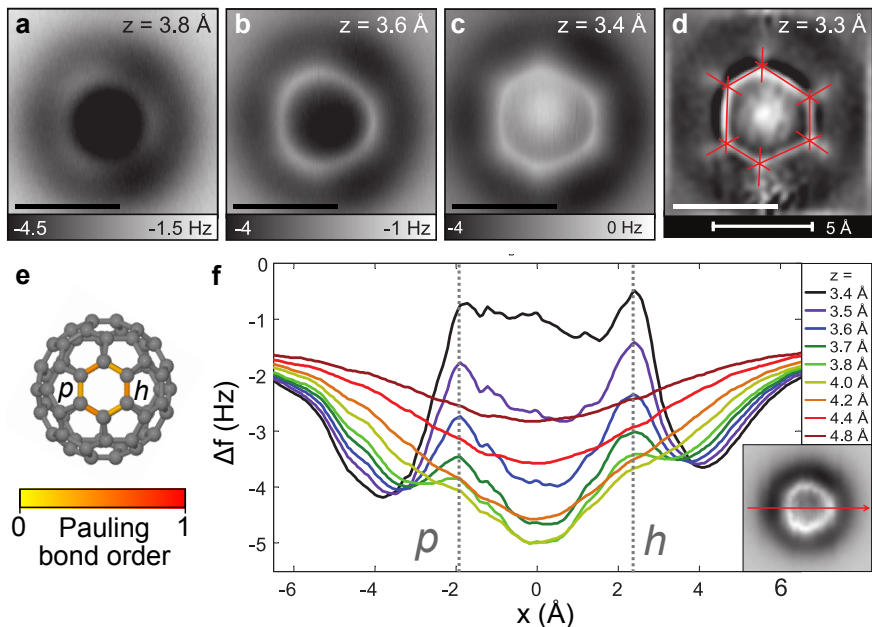


Figure 7.1.: **Effects of bond order, C_{60} .** **a-c.** AFM maps of C_{60} on Cu(111) at different heights z with a CO tip. **d** Laplace and low pass filtered image to measure the apparent bond length L' . **e** Molecule model of C_{60} with the Pauling bond order of the p and h bond indicated at the top most ring. **f** Line profiles $\Delta f(x)$ across a p and h bond extracted from a 3D force map. The position of the line profiles is indicated in the inset showing a map of Δf at $z = 3.6 \text{ \AA}$ extracted from the same 3D force map. The apparent positions of the p and h bond are indicated by the dotted lines. The $x = 0$ corresponds to the molecular center determined by the minimum in $\Delta f(x)$ at $z = 4.8 \text{ \AA}$. Note that p is located at a smaller absolute value of x than h and that $\Delta f(x_p)$ is smaller than $\Delta f(x_h)$ for all plotted values of z . Scale bars: 5 \AA .

by STM^{129,130}. The molecule shown in Fig. 7.1 exhibited a hexagonal tile and is oriented as depicted in Fig. 7.1e. Using AFM, the frequency shift Δf at constant tip height z^a was recorded, as shown in Fig. 7.1a-c.

^aIn the calculations, d denotes the distance between the O atom of the unrelaxed tip and the plane of the imaged atoms. In experiment, the tip height was measured with respect to the STM set point; therefore, there is an offset with respect to d . Comparison with theory^{38,43} shows that the minimum of $\Delta f(d)$ above a carbon ring is usually found at $d = 3.9 \text{ \AA}$. By measuring the tip height that yielded the minimum of $\Delta f(z)$ in the experiment and by setting this height to $z = 3.9 \text{ \AA}$, we determined the offset. Therefore, the experimental z values correspond to the theoretical d values and approximately reflect the atomic tip-sample separation.

To obtain atomic contrast, z had to be decreased, usually until $\Delta f(z)$ reached its minimum above the molecule (in general, at $z \approx 3.9 \text{ \AA}$), and the contrast increased as z was further decreased. The smallest tip height where stable imaging conditions could still be maintained was $z \approx 3.3 \text{ \AA}$. The origin of the atomic contrast is Pauli repulsion, which increases with the local electron density, giving rise to the bright features corresponding to the atomic structure of the imaged molecule. The dark halo surrounding the molecules in the AFM images stems mainly from the attractive van der Waals (vdW) force, which shows no corrugation on the atomic scale^{38,43}.

Two important observations can be made from the AFM images in Fig. 7.1. On one hand, Δf is increased above the h bonds with respect to the p bonds. This effect was best observed for moderate tip heights (Fig. 7.1a). As can be read off in Fig. 7.1f by comparing the two local maxima of a line profile $\Delta f(x)$ across both bonds. The largest Δf difference of $\sim 0.4 \text{ Hz}$ was observed for $z = 3.7 \text{ \AA}$. Moreover, in images with atomic resolution, the h bonds appear shorter compared with the p bonds; this was best observed for the smallest accessible tip heights (Fig. 7.1c). Fig. 7.1d shows a Laplace filtered image that was used to determine the apparent position of the bonds and measure the apparent bond length, $L'_h = 2.0(2) \text{ \AA}$ and $L'_p = 2.7(2) \text{ \AA}$, respectively. Notably, the apparent bond lengths L' measured by AFM qualitatively correctly reflect that the h bond is shorter than the p bond. However, both bonds appear to be substantially longer than they really are, and the difference in the apparent bond lengths of $\sim 30\%$ is much greater than the real difference of $\sim 5\%$.

To understand the contrast mechanisms, DFT calculations were performed by Nikolaj Moll. Fig. 7.2c shows an image of the calculated interaction energy for a CO tip at a tip height of $d = 2.9 \text{ \AA}$, which can be qualitatively compared to the Δf image at $z = 3.8 \text{ \AA}$ (Fig. 7.2e)⁴⁰. The brighter appearance of the h bonds with respect to the p bonds is well reproduced. The contrast is related to the electron density (shown in Fig. 7.2e), which increases with bond order. The higher electron density leads to stronger Pauli repulsion; consequently, Δf is increased above bonds with greater bond order. To account for tip relaxations, especially tilting of the CO molecule at the tip apex^{42,131,132}, the tip was modeled as a Cu_2 cluster with a CO molecule attached, as shown schematically in Fig. 7.2a. Calculated $\Delta f(x)$ line profiles (Fig. 7.2d) without relaxations of the tip structure (dashed lines) show the $\Delta f(x)$ maxima above the bond positions (vertical gray lines), reflecting the corrugation of the C_{60} electron density. Calcula-

7. Molecular properties measured by AFM

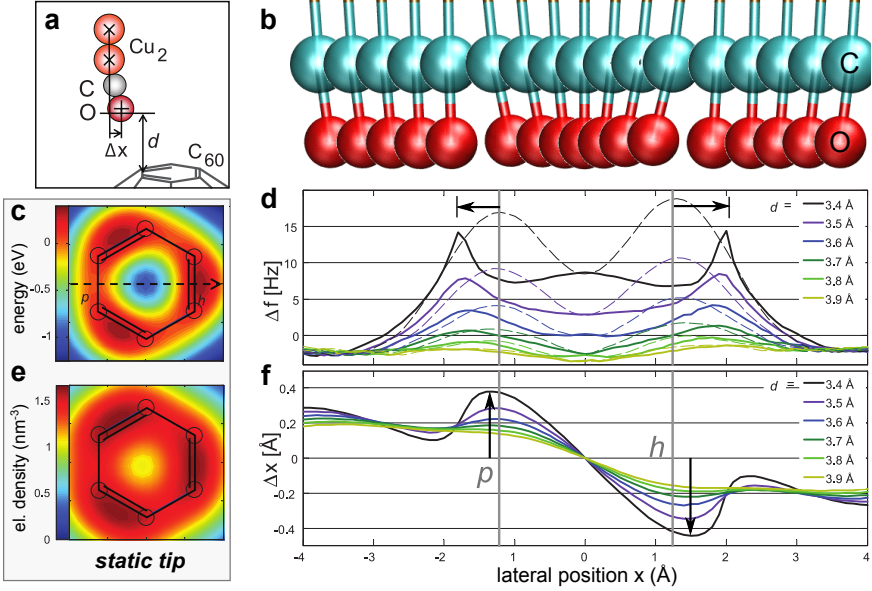


Figure 7.2.: **DFT calculations, C₆₀.** **a** Tip model of a CO tip on a Cu₂ cluster. **b** CO tip relaxation when the tip is scanned over the p and h bond (same x scale as in **d,f**), irrespective of the scan direction. **c,e** Calculated interaction energy (**c**) and electron density (**e**) at $d = 2.9$ Å above the molecule (image size: 4×4 Å). **d,f** Line profiles of Δf (**d**) and tip displacement $\Delta x(x)$ (**f**) calculated with a static tip (dashed lines) and relaxed tip (solid lines). The vertical gray lines in **d** and **f** indicate the positions of the p and h bonds as expected from the atomic model. The horizontal black arrows mark the shift of the bond positions in response to the tip relaxation (vertical arrows in **f**). This shift is bigger for the h bond.

tions including tip relaxations (solid lines) show a lateral shift of the $\Delta f(x)$ maxima positions (arrows in Fig. 7.2d) toward greater absolute values of x , leading to an expansion of the molecule in the image. Moreover, this lateral shift is greater above the h bond compared with the p bond, in agreement with the experiment. The important tip relaxation for the imaging process is the lateral displacement $\Delta x(x)$ of the oxygen atom at the tip apex (Fig. 7.2f) caused by tilting of the CO toward the molecular center because of lateral forces. As this oxygen atom defines the position of our probe, a falling slope of $\Delta x(x)$ results in an expansion, whereas a rising slope of $\Delta x(x)$ results in a compression along the x direction in the particular region of the image. The absolute value of Δx is greater above the h bond compared with the p bond (arrows in Fig. 7.2f). Hence, the h bond appears

to be shifted further away from the molecular center than the p bond, resulting in a decrease of L'_h with respect to L'_p as observed in the experiment.

Thus, tilting of the CO is responsible for the amplification of the differences in apparent bond length with respect to the real differences in bond length. Note that, only because of this amplification, differences in apparent bond length can be measured within the accuracy of the AFM instrument. Furthermore, right above the apparent positions of the bonds (that is, when the regions of maximal electron density are probed), $\Delta x(x)$ takes a rising slope, leading to a local lateral compression that gives rise to the very sharp appearance of the bonds at small tip heights. Notably, the calculations with a relaxed CO tip for $d = 3.4 \text{ \AA}$ also reflect several other details of the experiment, such as the appearance of a local maximum in the molecular center and the vanishing Δf contrast between p and h bonds observed for very small tip heights due to the tip relaxations.

Next, the PAHs hexabenzocoronene (HBC) on Cu(111) and dibenzonaphthoperylene (DBNP)⁹² (see structure models in Fig. 7.3a) on bilayer NaCl on Cu(111)^a were investigated. In general, the bonds at the periphery of a planar molecule show an increased frequency shift Δf corresponding to greater repulsive forces compared with bonds in the central region⁴³. In part, this effect is related to the delocalization of electrons in a π -conjugated system leading to increased electron density at the boundary. In addition, the smaller attractive vdW background at the periphery of the molecule leads to an increased Δf compared with the central molecular region. Because these effects are not easily deconvolved from contrast related to bond order differences, we focused on bonds in the central region of the molecules (see colored bonds in Fig. 7.3a). Note that bond order differences are obscured by the vdW background in the case of pentacene^{38,43}, where all bonds are near the periphery of the molecule. For HBC, the bonds i and j are not connected to the periphery, and the bonds within the central ring i are of greater bond order than the bonds j connecting the central ring to the outside rings¹³³. The qualitative contrast related to the bond order that was described above for C₆₀ is corroborated for HBC. In particular, it is observed that bonds with increased bond order appear brighter for moderate tip heights, and the differences in bond length were

^aC₆₀ and HBC could not be stably imaged by AFM on NaCl films with atomic resolution because they were laterally manipulated when using small tip heights. In contrast, DBNP could be imaged on bilayer NaCl on Cu(111) and was investigated on this surface to demonstrate that bond order discrimination is possible on different substrates.

7. Molecular properties measured by AFM

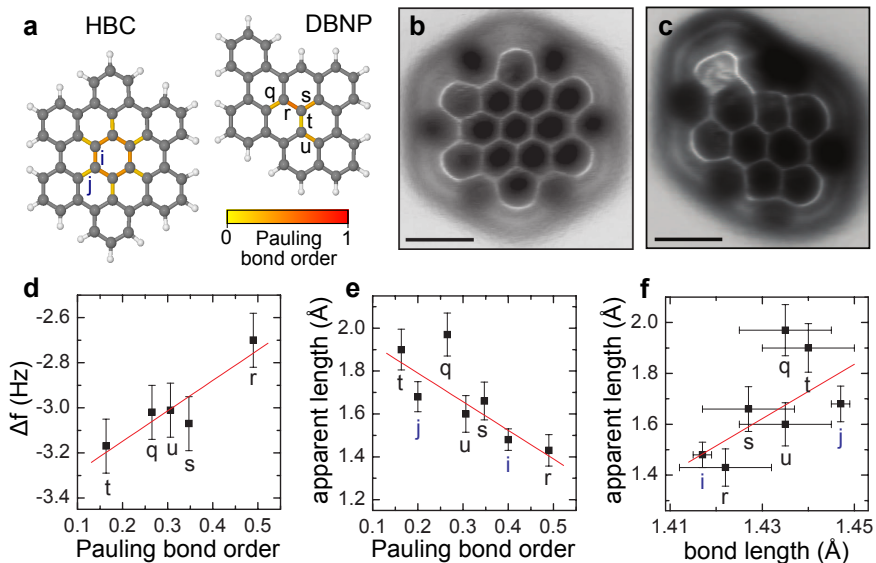


Figure 7.3.: **Effects of bond order, HBC and DBNP.** **a.** Molecule model of HBC and DBNP with the Pauling bond order of their inner bonds indicated. **b,c** Pseudo 3D image of an AFM map of HBC (**b**) on Cu(111) and DBNP (**c**) on NaCl(2ML)/Cu(111). **d,e** Measured Δf values (**d**) and the apparent bond length L' (**e**) for indicated bonds, including HBC in **e**, are plotted as a function of the Pauling bond order. **f** Apparent bond length as a function of the realistic bond length obtained by DFT calculations (for DBNP) and from diffraction data (for HBC). Linear regressions are drawn as a guide to the eye. Scale bars: 5 Å.

qualitatively reflected and amplified in the regime of minimal tip heights (Fig. 7.3b). The two different bonds i ($P_i = 0.4$, $L_i = 1.417(2)$ Å) and j ($P_j = 0.2$, $L_j = 1.447(2)$ Å)¹³³ were differentiated in the Δf contrast at constant height, measured as $\Delta f_i = -5.34(4)$ Hz, and $\Delta f_j = -5.46(6)$ Hz, respectively. The differences in apparent length could be observed in Fig. 7.3b and were measured as $L'_i = 1.48(4)$ Å and $L'_j = 1.68(7)$ Å, with the errors corresponding to the standard deviation measured for all six equivalent bonds. As described above, the contrast can be related to the different electron densities of the bonds, which qualitatively reproduces the measured differences in Δf . Notably, individual i and j bonds can be distinguished, although they differ only by 0.03 Å in length.

Finally, DBNP, a PAH that contains bonds of several different bond orders

was investigated. The five bonds in the central molecular region (labeled q , r , s , t , and u in Fig. 7.3a) have Pauling bond orders ranging from $P_t = 0.163$ to $P_r = 0.49$. Using both contrast mechanisms described above, r could be assigned as the bond of comparably highest bond order. Out of these five bonds, it showed the largest Δf signal (Fig. 7.3d) and the smallest apparent length (Fig. 7.3c,e,f). For the remaining four bonds, the differentiation was less clear, as can be seen in the graphs in Fig. 7.3d and e. Note that for DBNP, the bond order assignment was more challenging because of its low symmetry.

From our measurements on all three investigated molecular species, one can conclude that Pauling bond order differences (down to about 0.2) between individual bonds can be distinguished using AFM by both described contrast mechanisms. The frequency shift measured in different experimental runs cannot be compared quantitatively because of different background contributions of different tips. However, the measured apparent length showed no tip dependence within the experimental errors, as long as a stable CO-functionalized tip was used. Thus, the apparent lengths measured with different tips and on different planar molecules^a can be compared, as shown for HBC and DBNP in Fig. 7.3e. In Fig. 7.3f, the apparent length is plotted as a function of the realistic bond length extracted from DFT calculations (for DBNP) and x-ray diffraction measurements (for HBC)¹³³. The slope of the linear regression is 11; that is, the differences of the apparent bond length are about one order of magnitude greater than the differences in real bond length, as a result of the CO tilting at the tip apex. The two contrast mechanisms – one based on the frequency shift and the other based on the apparent length measured by AFM – are both corroborated by DFT calculations, and both can be used to differentiate bond orders in individual molecules. Notably, tilting of the CO at the tip apex amplifies the apparent length differences and renders it possible to detect length differences between individual bonds down to 0.03 Å.

^aAs vdW background forces also induce substantial tilting of the CO tip, the apparent bond length can only be compared if the vdW background is constant, which is given in the central part of planar molecules. The bond length measured for C₆₀ cannot be compared with the bond length measured for planar molecules, because the vdW background is not constant in the region around the p and h bonds due to the spherical shape of C₆₀, resulting in additional lateral distortions. However, the p and h bonds can be compared with each other because of their similar vdW background.

7.2. Tilting of the CO tip molecule and effect of fluorination

Most of the content presented in this section has been published in Nano Letters^{a 134}. Text excerpts and figures are reproduced by permission of the American Chemical Society.

In the previous sections we have seen that atomic resolution of molecules can be achieved with AFM using CO-terminated tips^{38,43,112,125,126,135–139}. Such images appear distorted³⁸, which can be exploited to distinguish the bond order of individual carbon–carbon bonds in polycyclic aromatic hydrocarbons and fullerenes¹¹² (see section 7.1). The origin of this distortion was recently also highly debated among experimentalists^{112,132,135,136} and theorists^{43,140,141}. Here, we study this distortion resulting in an enlarged and sharpened appearance of the imaged molecules in more detail and identify the underlying mechanisms.

To this end, we imaged 4-(4-(2,3,4,5,6-pentafluorophenylethynyl)-2,3,5,6-tetrafluorophenylethynyl) phenylethynylbenzene^{142,143} (FFPB) (see Fig. 7.4a) atomically resolved with AFM as shown in Fig. 7.4b,c. In FFPB, four carbon rings are connected by ethynylene units with triple bonds with two rings being H-terminated and two rings F-terminated. In the following, the rings are denoted as H-rings and F-rings, respectively. The FFPB molecules were studied on NaCl(2ML)/Cu(111).

From previous measurements on fluorinated and non-fluorinated PAH molecules we assign the orientation of the molecule in Fig. 7.4b,c as displayed in the model (Fig. 7.4a). That is, H-rings (left) and F-rings (right), which is confirmed by the STM orbital image (Fig. 7.5h) and KPFM measurement (Fig. 7.5f). Several observations are made: The H-rings appear with a substantially larger diameter than the F-rings of the FFPB molecule. The halo, that is, the region of minimal frequency shift surrounding the molecule, is less pronounced around the H-rings than around the F-rings (see Fig. 7.4c,d,f).

We also determined the adsorption height and geometry of the FFPB

^aMoll, N., Schuler, B., Kawai, S., Xu, F., Peng, L., Orita, A., Otera, J., Curioni, A., Neu, M., Repp, J., Meyer, G. & Gross, L. Image distortions of a partially fluorinated hydrocarbon molecule in atomic force microscopy with carbon monoxide terminated tips. *Nano Lett.* **14**, 6127–6131 (2014).

7.2. Tilting of the CO tip molecule and effect of fluorination

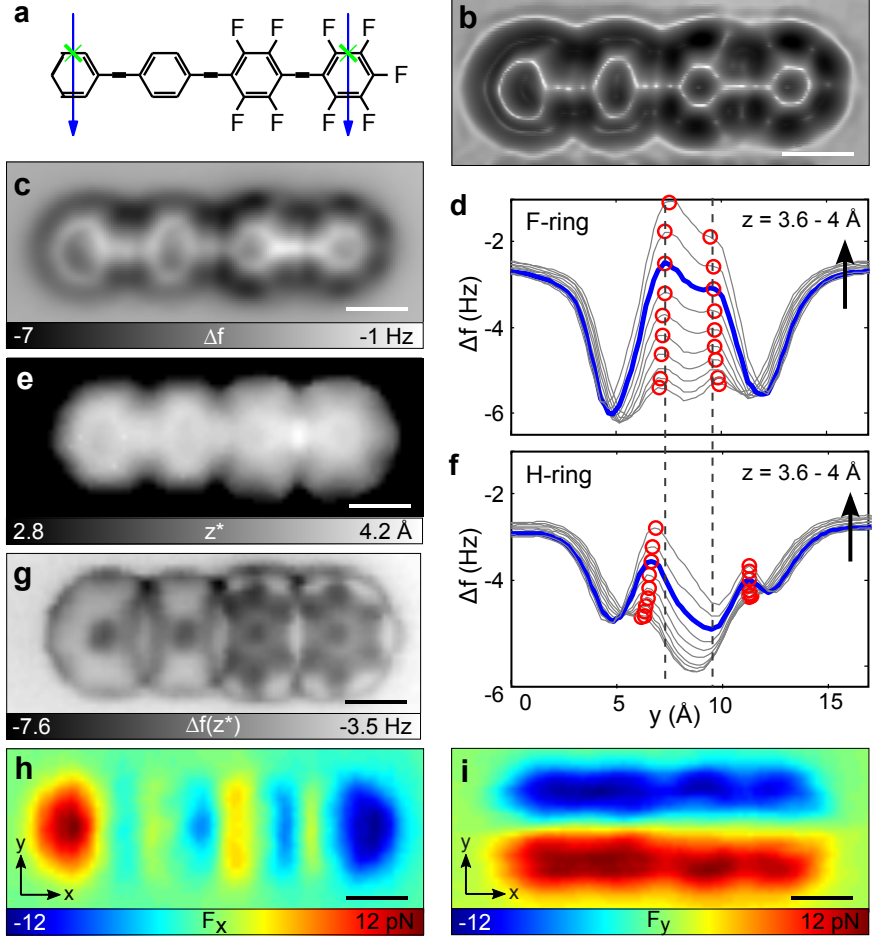


Figure 7.4.: **FFPB forcemap**. **a** The chemical structure of the FFPB molecule. Green crosses indicate the lateral positions y_{bond} which are compared to quantify the distortions, and blue arrows indicate the lateral positions of the linescans in **d** and **f**. **b** Pseudo 3D image of a Laplace filtered AFM map. **c** Unfiltered CO tip AFM data. **d,f** Δf linescans extracted from the forcemap across the outer F-ring (**d**) and H-ring (**f**) at different scan heights z . The red circles mark the apparent bond positions at each scan height. The dashed vertical line indicates the extent of the F-ring for the scan height printed in blue. **e** z^* (height of minimal Δf) topography extracted from a three dimensional force map. **g** Corresponding Δf value at z^* . Lateral forces extracted from the same forcemap: **h** F_x in the x -direction and **i** F_y in the y -direction. Scale bars: 5 Å.

7. Molecular properties measured by AFM

molecule on the substrate with AFM using the procedure detailed in section 7.3. We used z^* , that is, the tip height at minimal frequency, as a measure for the adsorption height (see Fig. 7.4e). The FFPB molecule adsorbs along a row of Na surface atoms, which is in agreement with the calculations. The absolute experimental tip height was calibrated by setting z^* at the center of the outer H-ring to the corresponding value of a calculated $\Delta f(z)$ spectrum ($z^* = 3.93 \text{ \AA}$). For the center of the outer F-ring, we measured $z^* = 4.03 \text{ \AA}$. In conclusion, the AFM measurements yield that the outer F-ring relaxes outward by 0.1 \AA compared to the outer H-ring, which matches the calculated height difference of 0.09 \AA very well. These results indicate that the adsorption geometry of the FFPB molecule on the substrate is very well described by the calculations with respect to the experiment. Differences in the adsorption height can lead to different apparent bond length and thus different apparent ring sizes as reported recently¹³⁶. The similar adsorption heights of the different rings, which we found by experiment and theory, indicate that for the FFPB molecule this effect will be small and other reasons must be responsible for the smaller appearance of F-rings compared to H-rings.

Next, we computationally investigated the mechanisms for the distortion of the AFM images obtained with CO-functionalized tips (for details see Ref. 134). The calculations were performed by Nikolaj Moll. First, to quantify the larger appearance of the rings in the AFM images, we looked at the lateral position y_{bond} of the molecular bond indicated by the green crosses in Fig. 7.4a with respect to the long molecular axis, which defines $y = 0$. Using the atomic positions of the calculated geometry of the FFPB molecule, we find that the outer H-ring and the outer F-ring have almost identical sizes in the y -direction as seen in Tab. 7.1. The difference in size is less than 0.4%.

Because the atomic contrast is a consequence of Pauli repulsion⁴³, which is related to the charge density¹⁴⁴, we examined the charge density of the FFPB molecule. Again we removed the substrate and kept the position of the molecule fixed. The charge density at constant height $z = 3.61 \text{ \AA}$ is shown in Fig. 7.5a.

The charge density above the H-rings is approximately a factor of two larger than that above the F-rings. The different saturations of the rings with either H or F atoms also lead to drastic differences in the apparent sizes of the rings in the charge density. This can be attributed to the larger electronegativity of the F atoms, which seems to influence the π -electrons of the FFPB molecule¹⁴³. The lateral position y_{bond} is given in Tab. 7.1

7.2. Tilting of the CO tip molecule and effect of fluorination

Table 7.1.: The lateral position of the molecular bond y_{bond} between the two outer C atoms of the H- and F-ring indicated by the green crosses in Fig. 7.4a: From the *geometry*, from the *electron density*, from the computed Δf image with a *fixed* CO at the tip, from the computed Δf image with a *relaxed* CO at the tip and from Δf image from *experiment*, respectively. For comparison the relative difference with respect to the value from the geometry is given in %.

	H-ring		F-ring	
	y_{bond} (Å)	%	y_{bond} (Å)	%
geometry	1.21		1.21	
density	1.45	20	1.05	-13
fixed	1.37	13	1.13	-6
relaxed	1.58	30	1.40	16
experiment	1.84	52	1.11	-8

when taking the maximum of the charge density as a measure for the bond location. y_{bond} for the H-ring is significantly larger and for the F-ring is significantly smaller with respect to the positions determined from the geometry.

AFM images are calculated using a Cu-dimer tip functionalized with a CO. First we considered a fixed CO at the tip. All four tip atoms are confined along a line perpendicular to the sample surface. The distances of the atoms were relaxed for the isolated tip. The frequency shift image is shown in Fig. 7.5b. As in the experiment the halo around the F-rings is larger and more pronounced compared to the H-rings. The image resembles the charge density very closely, except for the fact that the outer H- and F-rings exhibit a larger positive frequency shift than the two inner rings. In Tab. 7.1 the lateral position y_{bond} is given when taking the maximum of the frequency shift with this fixed tip as a measure. This value is relatively close to the corresponding value from the charge density for both the H-ring and the F-ring.

Next, the influence of the relaxation of the CO is examined. We calculated the frequency shift keeping the Cu-dimer tip fixed while relaxing the CO until the forces were smaller than 0.8 pN. The frequency shift image in Fig. 7.5c including relaxations of the CO shows some distinct differences to the image in Fig. 7.5b using a fixed CO. The halo around the F-rings is even more pronounced compared to that around the H-rings. Furthermore,

7. Molecular properties measured by AFM

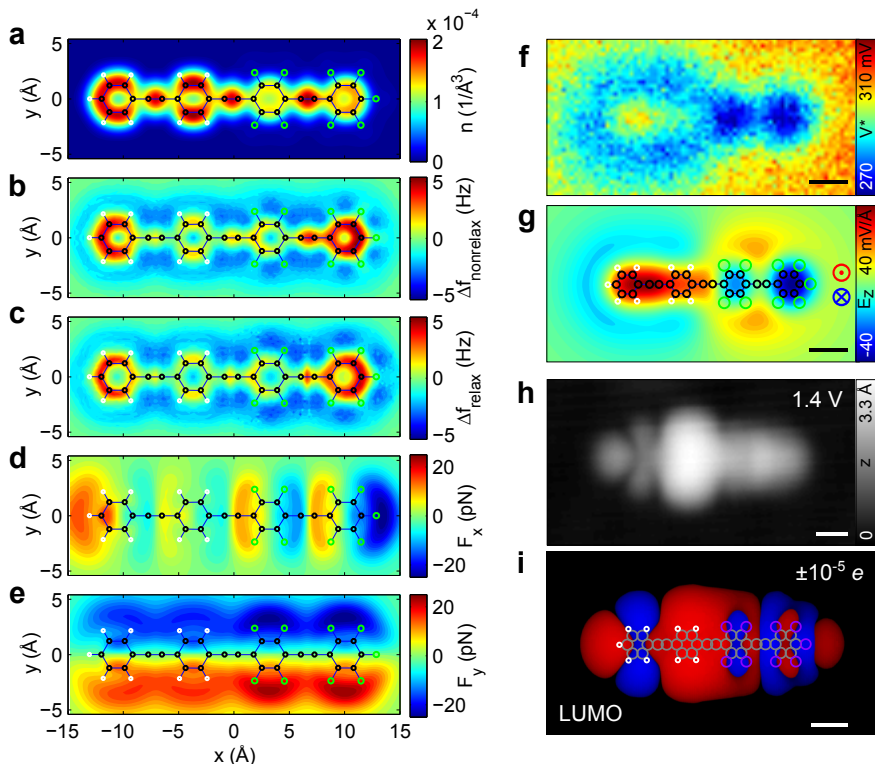


Figure 7.5.: **FFPB theory and KPFM.** **a** Calculated charge density at $z = 3.61$ Å and model of the FFPB molecule. **b** Calculated Δf image at a tip height of $z = 3.65$ Å with a fixed CO at a Cu-dimer tip and **c** with CO relaxed at the tip. **d** Calculated force F_x in the x -direction and **e** F_y in the y -direction. The lateral forces always tilt the CO towards the center of the nearest ring of the FFPB molecule. **f** Measured LCPD using a Cu tip. **g** The z -component of the electric field E_z above the FFPB molecule at a distance of 5 Å from the molecular plane. **h** STM orbital image ($I = 2$ pA, $V = 1.4$ V) of FFPB in the same orientation as the other images. **i** Calculated LUMO isosurface at $\pm 10^{-5} e$. Scale bars: 5 Å.

all rings appear larger (Tab. 7.1). Tilting of the CO enlarges the apparent sizes of the H- and F-rings when comparing with the results with a fixed tip.

To understand the origin of the differences between experiment and computations, we determined the lateral forces experimentally and computationally. Experimentally, the lateral forces were obtained by integrating

7.2. Tilting of the CO tip molecule and effect of fluorination

the frequency shift twice over the vertical distance and taking the lateral derivative in x - and y -directions³⁴. However, as the tilt of the CO depends on the tip height, the lateral position of the probing O atom changes with the tip height. This will lead to an error in the integration¹³⁵. The experimental lateral forces are shown in Fig. 7.4h,i. The largest lateral forces arise above and in the vicinity (about 2 Å) of the molecule, corresponding to the extent of the halo around the molecule. The forces always point towards the center of the nearest ring. The computed lateral forces (Fig. 7.5d,e) are qualitatively very similar to the experimental ones. In the experiment, the lateral force F_y is similar in size above both types of rings, whereas in the computations it is larger above the F-rings than above the H-rings. The reason for the larger lateral force above the F-rings is not clear. The screening of the substrate which is neglected in our calculations might reduce the van der Waals contributions. Finally, electrostatic interactions might be another source of the remaining discrepancy between experiment and theory. Electrostatic interactions and their effect on the tilting are included in our theory, however, with some errors. The dipole moment of CO tips is not completely accurate in DFT and under debate experimentally^{145,146}. Moreover, also higher order electrostatic multipole moments of the tip have to be taken into account^{94,147}.

The electrostatics can be probed experimentally employing KPFM. We recorded an LCPD map of the FFPB molecule⁴⁰, shown in Fig. 7.5f. The LCPD contrast can be qualitatively compared to the z component of the electrostatic field E_z ^{40,94,147}, which we calculated for the free FFPB molecule, shown in Fig. 7.5g. The qualitatively different contrast obtained on the H- and F- terminated rings and the good qualitative agreement with the calculations verifies also the molecular orientation as claimed above. Both experiment and theory indicate an essentially inverted electrostatic field for H- with respect to F-rings. The findings suggest that the H-rings are partially negatively charged in the center and positively in the ring periphery¹⁴³. The opposite is true for the F-rings, where the F atoms attract electrons to the periphery. Therefore, electrostatic forces will act differently on H- and F-rings and could lead to different image distortions for both type of rings.

In the computations, we can examine the origin of the lateral forces in more detail. From the lateral displacement Δy of the O atom of the CO and the lateral force F_y , we can calculate an effective spring constant. This is 30 to 60% larger than the inherent spring constant of 0.49 N/m for the

7. Molecular properties measured by AFM

tip calculated without a sample molecule¹¹². Especially the vertical force from the sample molecule acting on the CO leads to an additional restoring force. If we take a maximal vertical force of 80 pN and a lever arm of 3.02 Å¹³², this vertical force alone results in an increase of the lateral spring constant of the CO molecule of 0.26 N/m¹³⁵. Therefore, this additional stiffness to the inherent, position-independent stiffness of the CO cannot be neglected. Furthermore, a different substrate material can change the vertical van der Waals forces or a bias between tip and sample can lead to additional electrostatic vertical forces and therefore to a change of the stiffness of the CO tip and of the image distortions.

For large tip heights ($z > 4$ Å) the lateral forces show almost no atomic contrast and no contribution of the Pauli repulsion. For all lateral positions, the lateral forces tilt the CO towards the center of the nearest ring in the FFPB molecule. The tilt leads in general to a larger appearance of molecules and rings and at smaller tip heights also to a sharper appearance of the bonds. This lateral sharpening of the bonds is commonly observed in AFM measurements with CO terminated tips on molecules^{38,43,112,125,126,135–139}. At small tip heights, approximately when the maximal short range force is reached, the intramolecular bonds appear as sharp lines with a full width of half maximum (FWHM) much smaller than the charge density^{112,140}. This apparent sharpening of bonds is a result of the Pauli repulsion in interplay with the van der Waals interaction. Also the elongated shape of the triple bonds in ethynylene units perpendicular to the direction of the bond in AFM images (Fig. 7.5c) is a result of this intricate interplay. This characteristic distortion of triple bonds has also been experimentally observed in a recent study using CO-terminated tips¹³⁸ and is also apparent in the case of FFPB (Fig. 7.4b,c). It is important to note that the sharpening is not a dynamic effect and does not originate from the oscillating or scanning motion of the tip. The sharpening can be fully reproduced by the static calculations and is a result of the different tilt angles of the CO molecule at the different lateral tip positions.

The image distortions of a FFPB molecule in AFM with a CO-terminated tip were studied in detail. We observed experimentally that the fluorinated rings appear with smaller diameter than the hydrogenated rings. The distortions with respect to the atomic positions of the atoms have two origins: The charge density and the tilt of the CO at the tip. Already in the charge density in a plane above the FFPB molecule the rings exhibit different sizes. In addition the molecules appear distorted because of the tilt of the CO due

to attractive van der Waals and electrostatic forces. For small tip heights, the Pauli repulsion and the van der Waals interactions together tilt the CO in such a way that the bonds appear sharpened.

7.3. Adsorption geometry determination

Most of the content presented in this section has been published in Physical Review Letters^a ¹²⁶ and in Chemistry: a European Journal^b ¹⁴⁸. Text excerpts and figures are reproduced by permission of the American Physical Society and Wiley-VCH publishing.

As became apparent in the previous sections, the crucial factors affecting the AFM image contrast are the chemical interaction between probe and sample³⁶, the tip termination^{38,43,80}, and the adsorbate geometry¹²⁵. For organic molecules on metal substrates, the adsorption geometry (adsorption site, height, tilt) is intimately linked to the electronic properties of the adsorbate and the interaction between adsorbate and substrate¹⁴⁹. In other words, the adsorption geometry is a direct indicator of the adsorbate-substrate interaction. The adsorption height of molecules above the substrate is traditionally measured using the x-ray standing wave method (XSW)^{150,151}. While XSW allows us to determine the adsorption height with high precision and chemical sensitivity, it does not (yet) provide information about the lateral adsorption position or tilt angle. Because XSW values are averaged over large ensembles, individual molecules are not distinguished. In contrast, using scanning probe microscopy, molecules are treated individually, and therefore the molecular adsorption geometry can be measured as a function of molecular conformation¹²⁵ or the adsorption site¹⁵². The adsorption site of single adsorbates can be determined by STM using marker atoms^{153,154} or inelastic electron tunneling spectroscopy¹⁵⁵ or by directly resolving substrate and adsorbate by AFM^{39,110,125}. However, to date, adsorption heights could not be quantified by scanning probe microscopy.

In the following a novel experimental approach to extract the molecular

^aSchuler, B., Liu, W., Tkatchenko, A., Moll, N., Meyer, G., Mistry, A., Fox, D. & Gross, L. Adsorption geometry determination of single molecules by atomic force microscopy. *Phys. Rev. Lett.* **111**, 106103 (2013).

^bMistry, A., Moreton, B., Schuler, B., Mohn, F., Meyer, G., Gross, L., Williams, A., Scott, P., Costantini, G., & Fox, D. The Synthesis and STM/AFM Imaging of ‘Olympicene’ benzo[cd]pyrenes. *Chem. Eur. J.* **21**, 2011–2018 (2013)

7. Molecular properties measured by AFM

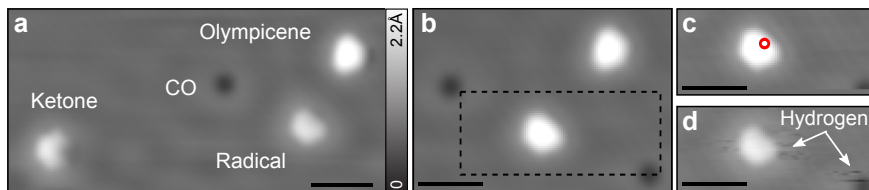


Figure 7.6.: **Olympicene dehydrogenation.** **a** STM topographies of olympicene, radical and ketone on Cu(111) ($I = 2 \text{ pA}$, $V = 0.2 \text{ V}$). Same topography scale applies also to **(b-d)**. **b** Two olympicene molecules (bright) and two CO molecules (black). The area within the dashed box is shown in **c** and **d**. **c,d** Olympicene molecule before (**c**) and after (**d**) applying a voltage pulse of 1.6 V at the position indicated by the red circle. After the pulse the olympicene is dehydrogenated to the radical. Scale bars: 20 \AA .

adsorption geometry in full detail by AFM is presented and the results compared to state-of-the-art DFT calculations. First, the method of determining heights is exemplified for pentacene and diindenoperylene (DIP) and the role of our tip termination, CO and Xe, is discussed. Thereafter, the method is applied to three molecules of the olympicene family, 6H-benzopyrene (olympicene), benzopyrene (radical), 6H-benzopyren-6-one (ketone), which differ in their chemical structure only by one atom. Finally, adsorption sites of all aforementioned molecules are determined by atomically resolving the substrate and the adsorbed molecule in one image. The molecules are investigated on Cu(111).

Before we turn our discussion to the adsorption height, the preparation of the olympicene molecules is briefly explained. Olympicene and ketone are prepared simultaneously by flash heating (as described in section 5.1) as in the olympicene sample many ketone molecules were present as a precursor from the olympicene synthesis. Radical is generated on the surface by removing one hydrogen atom from olympicene by a voltage pulse of 1.6 V at 10 pA (see Fig. 7.6)¹⁵⁶.

Adsorption height. In Fig. 7.7 typical AFM measurements with a CO tip are presented of radical and olympicene (Fig. 7.7a), pentacene and DIP (Fig. 7.7b) as well as two pentacenes (Fig. 7.7c). Qualitatively, the difference in adsorption height between and within a molecule becomes already apparent by the different Δf contrast. That is, increased repulsive forces in constant height mode indicate increased adsorption heights¹²⁵. This simplified picture is of course only valid, if the molecules being probed are chemically equivalent for the tip. In the case of olympicene and radical

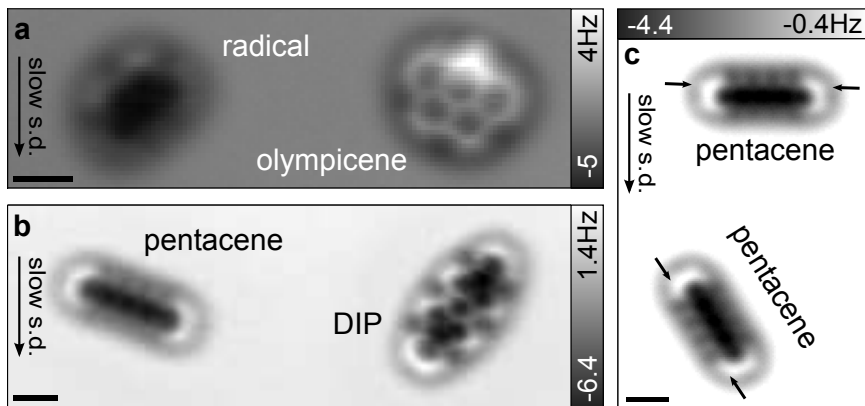


Figure 7.7.: **Constant height AFM.** a-c AFM images with a CO functionalized tips of radical and olympicene (a), pentacene and DIP (b) and two pentacenes (c) on Cu(111). Height offsets (STM conductance set points in brackets): -1.2 \AA ($G = 57 \text{ pS}$) in a, -1.2 \AA ($G = 10 \text{ pS}$) in b and -2.2 \AA ($G = 10 \text{ pS}$) in c. The arrows in c mark the pentacene site that is slightly up tilted. Scale bars: 5 \AA .

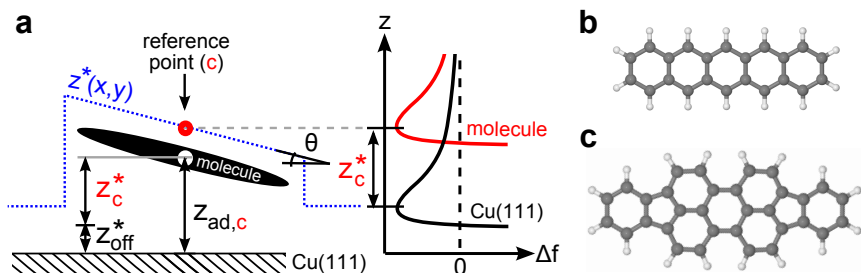


Figure 7.8.: **Adsorption height determination.** a Schematic of the adsorption height determination. b Pentacene structure model. c DIP structure model.

(Fig. 7.7a) it can be readily concluded from the constant height image that radical is closer adsorbed. The effective height difference, however, is difficult to quantify from the bare Δf information at constant height. The strong dependence of the Δf contrast on the molecule–tip separation even render possible to detect the slight tilting of pentacene along its short axis, see Fig. 7.7c. Note that the greater Δf value was always observed on the same molecule site with respect to the substrate, irrespective of the tip. That is, the two-fold symmetry along the molecules long axis is broken upon adsorption.

7. Molecular properties measured by AFM

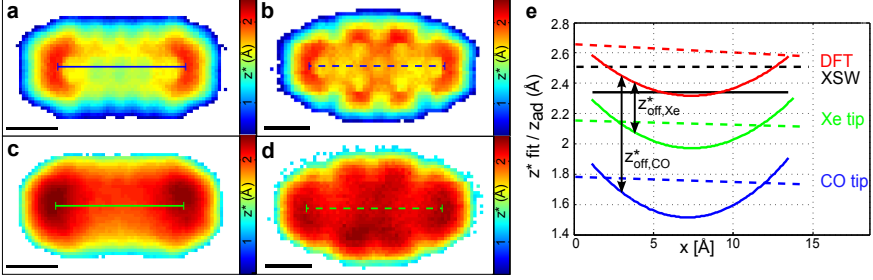


Figure 7.9.: **Adsorption height pentacene and DIP.** **a-d** The tip height z^* at minimal Δf on pentacene (**a,c**) and DIP (**b,d**) on Cu(111) with CO (**a,b**) and Xe (**c,d**) terminated tip. $z^*(x, y)$ is extracted from a 3D Δf map and given with respect to the z^* value on Cu(111) with the respective tip. White points mark spectra where the Δf minimum was not reached during data acquisition. **e** Line profiles of the fitted parabolic trough for pentacene (solid lines) and plane for DIP (dashed lines) for the measurements in **a-d** and calculated geometries using DFT+vdW^{surf} along the molecules' long axis (see lines in **a-d**). The black lines mark the experimental XSW values (no lateral information). Note that there is a tip dependent offset $z^*_{\text{off,CO}}$, $z^*_{\text{off,Xe}}$ between the calculated and AFM measured values. Scale bars: 5 Å.

To quantitatively determine the position dependent adsorption height a methodology is developed based on force-distance spectroscopy. In Fig. 7.8 the scheme of our method for measuring adsorption heights is illustrated. To access the molecular adsorption height and tilt we determine for different lateral positions (x, y) the height $z^*(x, y)$ where the frequency shift $\Delta f(x, y, z)^a$ is minimal:

$$z^*(x, y) = \arg \min_z \{ \Delta f(x, y, z) \} \quad (7.1)$$

with respect to the correspondent substrate value. To obtain a z^* map, individual $\Delta f(z)$ spectra were recorded with variable tip approach on a 2D grid above the molecule⁷⁷. To compare the molecular adsorption height, tilt and bending between experiment and theory a geometry model is fitted and the adsorption height at a certain reference point, tilt angle and bending from this fitted model is extracted. In general, the $z^*(x, y)$ values will differ from real adsorption heights $z_{\text{ad}}(x, y)$ (see Fig. 7.9e). The observed offset, $z^*_{\text{off}} = z_{\text{ad}}(x, y) - z^*(x, y)$, which depends on the tip termination, originates from the chemically inequivalent species being probed for the calibration:

^a The Cu background spectrum has been subtracted from all $\Delta f(z)$ curves.

Cu on the substrate and C on the molecule. Moreover, this offset is sensitive to the sample bias and macroscopic tip shape. Therefore, only adsorption height differences can be determined even if the tip does not change during the measurement. However, to facilitate an absolute adsorption height determination the offset can be gauged by z^* measurements on a molecule with known adsorption height (done here) or by calculating z^* on the substrate or molecule with an appropriate tip model. Furthermore, the bias dependence of z_{off}^* could be reduced by measurements at compensated bias (local contact potential difference, LCPD). However, the LCPD depends on the lateral and vertical tip position⁴⁰, which makes it difficult to account for.

Here, $z^*(x, y)$ maps were recorded on similar molecules (in extent and composition) with CO or Xe tips at zero bias. First, pentacene and DIP shown in Fig. 7.8b,c are investigated. For both molecules identical CO and Xe tips were used, respectively. The fact that absolute adsorption height values are known for pentacene and DIP from XSW measurements and theory allows us to link the measured z^* values to absolute height values. Maps of z^* with CO tips (Fig. 7.9a,b) are atomically corrugated, whereas Xe tips (Fig. 7.9c,d) give a smoother contrast being predominantly susceptible to the collective molecular geometry. With both tips, increased z^* values above the ends of pentacene with respect to its molecular center are observed.

Since XSW measurements can only provide averaged values for adsorption heights of a certain atom species, DFT calculations were performed to gain site-specific adsorption height information. These calculations are challenging due to the interplay of Pauli repulsion, covalent interactions, electron transfer processes and van der Waals (vdW) interactions¹⁵⁷. The DFT+vdW^{surf} method¹⁵⁸, which is a synergetic combination of the DFT+vdW method¹⁵⁹ for inter-molecular interactions with the Lifshitz-Zaremba-Kohn theory for the non-local Coulomb screening within the bulk, predicts adsorption heights of organic molecules on coinage surfaces with an accuracy of 0.1 Å^{160,161}. In the following the DFT+vdW^{surf} method is applied to our measured systems by using Perdew-Burke-Ernzerhof¹⁶² for the exchange-correlation functional. The calculations were done by Wei Liu in the group of Matthias Scheffler at the Fritz Haber Institute.

Pentacene has a parabolic shape along its long symmetry axis, DIP is mainly flat. Therefore a parabolic trough for pentacene and plane for DIP is fitted to the relaxed molecule structures and the experimental

7. Molecular properties measured by AFM

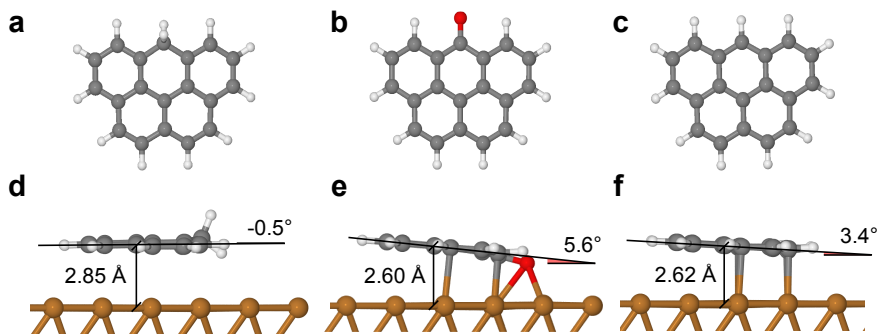


Figure 7.10.: **Olympicipenes theory.** **a-c** Molecule model of olympipene, ketone and radical, respectively. **d-f** Calculated adsorption geometry of olympipene, ketone and radical, respectively using PBE+vdW^{surf} DFT functionals.

z^* surface, which is presented in Fig. 7.9e. For pentacene and DIP the adsorption height difference between both molecules and the curvature of pentacene are in good agreement with the calculated adsorption geometry (see Tab. 7.2) and XSW measurements^{160,163}. By comparison to the DFT data it is found that z_{off}^* in the AFM measurements was $\approx 0.8 \text{ \AA}$ for the CO and $\approx 0.4 \text{ \AA}$ for the Xe tip shown in Fig. 7.9. Although the results obtained with CO and Xe tips match the calculations comparably well, we will focus in the following on measurements of z^* with Xe tips to avoid possible influence from CO bending, which has been reported to affect the Δf contrast^{42,112}. Moreover, the smooth z^* contrast of the Xe tip makes z_{off}^* independent of the specific molecule site that is probed.

Now we will apply the method introduced above to the olympicipenes. The olympicipenes are three molecules formed of five carbon rings. They differentiate from each other by the atom(s) bound to the carbon at the edge of the central carbon ring. In the case of olympipene (Fig. 7.10a) there is a sp^3 hybridized carbon atom forming a C-H₂ (methanediyl) moiety. For the radical the carbon atom is sp^2 hybridized having a single hydrogen bound to the carbon (C-H). The ketone has a carbonyl group (C=O) at that position. Despite their close structural similarities the olympicipenes have very distinct adsorption characteristics on Cu(111) predicted by theory¹⁶⁴. The DFT+vdW^{surf} calculations show very distinct adsorption height differences between the olympicipenes (see Fig. 7.10d-f). Olympipene is physisorbed (greatest adsorption height), ketone is in an intermediate regime between physis- and chemisorption, whereas radical is

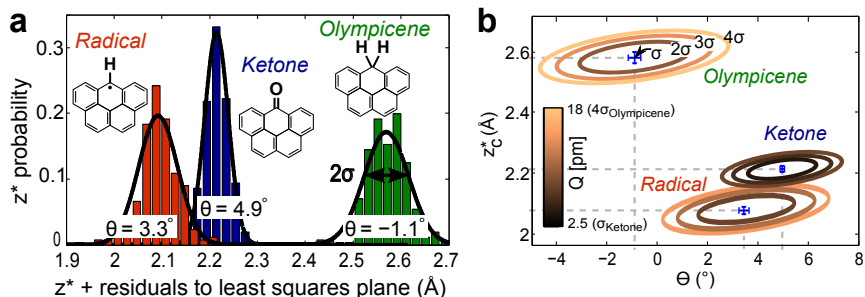


Figure 7.11.: **Adsorption height olympicenes.** **a** Probability distribution of z^* recorded with a Xe tip around the least-squares fitted plane with tilt angle θ and height z_c^* for the olympicenes. The black curves correspond to fitted Gaussian line shapes. The insets illustrate the molecule structures of the olympicenes, where the positions of other hydrogens have been omitted for clarity. **b** Contour plot of the root-mean-squares error Q between z^* and a plane with z_c^* and θ as free parameters. The contours are shown for multiples of the standard deviation of the least squares fitted plane σ . The blue error bars mark the standard error of the parameters.

chemisorbed¹⁶⁵ (smallest adsorption height). The olympicenes adsorb in a planar but tilted geometry. To compare the adsorption heights of this tilted geometry, the central carbon atom serves as reference point. The z^* and z_{ad} value (of the fitted model) at this reference point are denoted as z_c^* and $z_{\text{ad},c}$, respectively. Like in the case of DIP it is assumed from the calculation that the structure lies in a plane described by $z_i^* = f(x_i, y_i; z_c^*, \theta)$, where the z^* value of the spectrum i at the position (x_i, y_i) is given by z_c^* and θ describing the height offset and tilt angle, respectively. The plane is fitted by the least mean squares error method to those spectra of the 3D Δf map that are lying within the circumference of the calculated structure model. From the fitted plane, the tilt angle θ and z_c^* are extracted.

In Fig. 7.11 the different olympicenes are compared. In Fig. 7.11a a histogram of the residuals of z^* with respect to the least-squares fitted plane plus the corresponding z_c^* value are plotted. At the central carbon atom the adsorption height differences of the olympicenes can be identified. The normally distributed residuals of ketone and radical imply the appropriate choice of our geometry model (plane). In contrast, the residuals of olympiacene are less well described by the Gaussian because a small bending of the molecule perpendicular to its symmetry axis is observed. This small bending, which is also observed in the calculations, makes the structure not perfectly described by our geometry model.

7. Molecular properties measured by AFM

Table 7.2.: Comparison of adsorption heights from z^* , DFT+vdW^{surf} and XSW^{160,163} (if available).

	CO tip		AFM Xe tip		DFT		XSW
	z_c^*	θ	z_c^*	θ	z	θ	z
pentacene	1.51 Å	-	1.97 Å	-	2.32 Å	-	2.34 Å
DIP	1.76 Å	0.2°	2.14 Å	0.2°	2.61 Å	0.3°	2.51 Å
olypmicene	2.38 Å	-2.6°	2.58 ± 0.03 Å	-1.1 ± 0.2°	2.85 Å	-0.4°	-
ketone	2.08 Å	5.4°	2.21 ± 0.01 Å	4.9 ± 0.1°	2.66 Å	5.9°	-
radical	2.06 Å	2.5°	2.08 ± 0.03 Å	3.3 ± 0.1°	2.62 Å	3.4°	-

To estimate the error of the fitting parameters z_c^* and θ , the root-mean-square errors Q are plotted in Fig. 7.11b as a function of both fitting parameters with isolines at multiples of the standard deviation σ of the least squares fit. Q is given by

$$Q = \sqrt{\frac{1}{N} \sum_{i=1}^N (z_i^* - f(x_i, y_i; z_c^*, \theta))^2} \quad (7.2)$$

where N is the number of considered spectra. The error bars indicating the standard error of the parameters are defined by the contour line with the value $Q = \sigma\sqrt{1 + 1/N}$. The relative adsorption height difference and tilt angle between the olypmicenes can clearly be distinguished. The measured tilt angles for olypmicene, radical and ketone compare very well with the calculated tilt angles (see Tab. 7.2). By comparing z^* to the DFT calculations of the olypmicenes one finds for Xe tips that $z_{\text{off}}^* = (0.4 \pm 0.2)$ Å, i.e., similar values as for pentacene and DIP. Note that the high accuracy of z_c^* and θ is a consequence of the exponentially decaying Pauli repulsion^{43,144} and the reproducibility of z^* from the different Δf -distance spectra during one measurement.

In Fig. 7.12 a 3D plot of the z^* surface of the olypmicenes recorded with a CO tip are shown with the least-squares fitted plane overlaid. Please note that the error estimation procedure as described above was only done for the Xe tip. The respective errors of θ and z_c^* for the CO tip are about 5 times greater because of the atomic corrugation in z^* , which is not considered in the simple plane model. Consequently, the residuals of z^* with respect to this plane are not normally distributed.

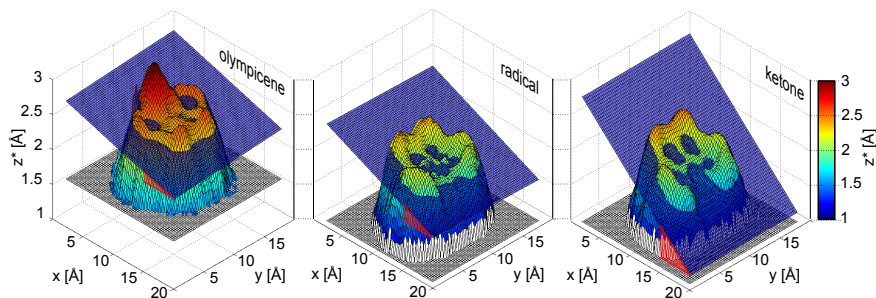


Figure 7.12.: **Olympicenes z^* surfaces.** **a-c** 3D representation of z^* maps of olympicene (**a**), radical (**b**) and ketone (**c**). Least squares fitted planes are superimposed in blue.

Adsorption site. The adsorption sites were determined by a method we name adjusted constant height AFM. To atomically resolve substrate and molecule, a CO terminated tip is scanned in constant height mode at a smaller height distant from the molecule and at a greater height above the molecule. By extracting the stacking sequence at a step edge, *hcp* and *fcc* hollow sites can be differentiated globally for the single crystal. Accordingly, the surface atoms of two subsequent terraces were atomically resolved in a single image (see Fig. 7.13a). The extrapolation of the grid of the upper terrace on the lower terrace identifies *hcp* sites as hollow sites where atoms of the lower terrace are found. Note that for the (111) face, the atom positions can be identified due to symmetry reasons. With the CO tip the Cu atom sites are more attractive (darker) than the atomic interspace in the operated distance regime.

Pentacene was found to adsorb either on *bridge*30° (Fig. 7.13b) or *hcp*30° site with respect to its carbon ring centers. The 30° describes the azimuthal angle between the close-packed directions of the (111) face to the direction connecting two opposing atoms in the carbon rings of the molecule. DIP adsorbs in a low symmetry direction of Cu(111) on *bridge*10° site (Fig. 7.13c). Olympicene and ketone were found to adsorb either on *hcp*30° or *fcc*30° sites (Fig. 7.13d,f). The radical on the other hand was observed exclusively on *fcc*30° sites. This could be explained by the larger substrate coupling observed by the smaller adsorption height. For each molecular species about ten adsorption site measurements were performed. Of course other possible adsorption sites, though unlikely, cannot be completely excluded. The simplicity, rapidity and accuracy of the introduced method without requiring marker atoms is very beneficial. Note that the

7. Molecular properties measured by AFM

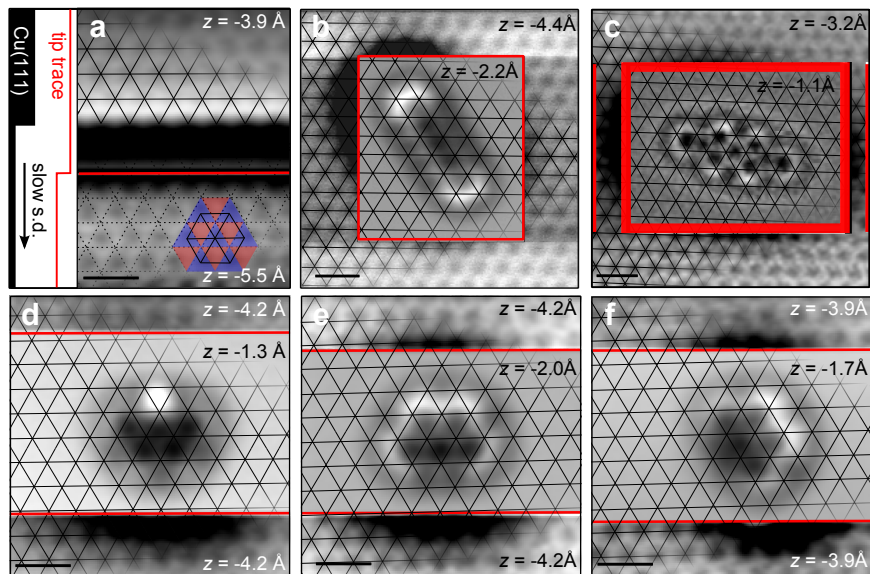


Figure 7.13.: **Adsorption site.** Adjusted constant height AFM images with CO functionalized tips (tip height z changes are marked by red lines). Tip heights are given with respect to a STM set point ($I = 2$ pA, $V = 0.2$ V). The Δf -scale is optimized in each image part (brighter means a less negative Δf value). Crossings of black continuous lines mark Cu atom positions. **a** The atom positions of both Cu layers at a step edge (grid of upper Cu layer is continued as dashed grid on lower layer) determine the *hcp* sites (triangles pointing up, marked blue) and *fcc* sites (triangles pointing down, marked red). The adsorption sites are given with respect to the centers of the C₆-rings. **b** Pentacene on *bridge*30° site (also *hcp*30° observed). **c** DIP on *bridge*10° site. **d** Olympicene on *hcp*30° site (also *fcc*30° observed). **e** Radical on *fcc*30° site (exclusive adsorption site). **f** Ketone on *fcc*30° (also *hcp*30° observed). Scale bars: 5 Å.

adsorption geometry of the molecule can be correlated to its adsorption site. For the shown molecules, however, no influence of the adsorption site on the adsorption height or tilt was observed within our measurement error.

In summary, the adsorption site, height and tilt of single molecules were measured by AFM using CO and Xe functionalized tips. The adsorption height is the sum of a tip dependent offset z_{off}^* and z^* that reflects the molecular adsorption geometry. The demonstrated small statistical error of 3 pm (!) for z^* facilitates a high sensitivity to inter- and intra-molecular differences in adsorption heights. Therefore differences in adsorption height

and tilt for the olympicenes could be determined. Furthermore, very small deviations from a planar adsorption geometry, like the bending and tilting of pentacene on Cu(111) were detected with a resolution of 0.2° (!). The offset that depends on the tip termination, the macroscopic tip shape, substrate material and applied bias has a larger systematical error. By comparison with DFT and XSW data it was found for our Xe terminated tips that this offset is approximately 0.4 \AA with an error of 0.2 \AA . Including this tip dependent offset facilitates the determination of absolute adsorption heights of individual molecules by AFM. This detection of the molecular adsorption geometry in combination with the knowledge about the adsorption site provides a detailed picture of the molecular adsorption characteristics. The presented method is also a first step to extract *quantitative* information by AFM.

7.4. Contrast formation in KPFM on molecules

Most of the content presented in this section has been published in Nano Letters^{a 147}. Text excerpts and figures are reproduced by permission of the American Chemical Society.

Measuring the detailed charge distribution in individual charge-transfer complexes (CTCs) is of particular interest because of their application in molecular electronics^{166–169}, organic photovoltaics¹⁷⁰ and organic light emitting diodes (OLEDs). Resolving their charge distribution on the atomic scale is a long-standing goal and Kelvin probe force microscopy (KPFM) is the designated technique to achieve this goal. By KPFM⁵¹, one measures the local contact potential difference (LCPD), which yields information about the distribution of charges (see section 3.2). With KPFM, charge sensitivity has been demonstrated on single atoms³¹, defects^{94,95,171,172}, surfaces^{87,94,97–99}, and also on molecules^{40,96,143}. However, the underlying contrast mechanism of KPFM at the atomic scale and the interpretation of atomically resolved LCPD maps are still under debate and are also tackled by recent theoretical studies^{101,102}.

Charge-transfer complexes. A CTC or electron donor–acceptor complex is in our context a single molecule (but in general can also refer to an

^aSchuler, B., Liu, S., Geng, Y., Decurtins, S., Meyer, G. & Gross, L. Contrast formation in Kelvin probe force microscopy of single π -conjugated molecules *Nano Lett.* **14**, 3342–3346 (2014)

7. Molecular properties measured by AFM

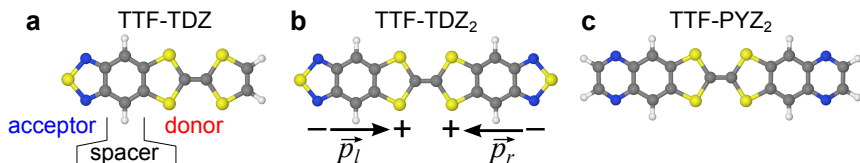


Figure 7.14.: **Charge-transfer complexes (CTCs)** **a** Structure model of the polar TTF-TDZ molecule. **b,c** Structure model of the bipolar TTF-TDZ₂ and TTF-PYZ₂ molecule, respectively.

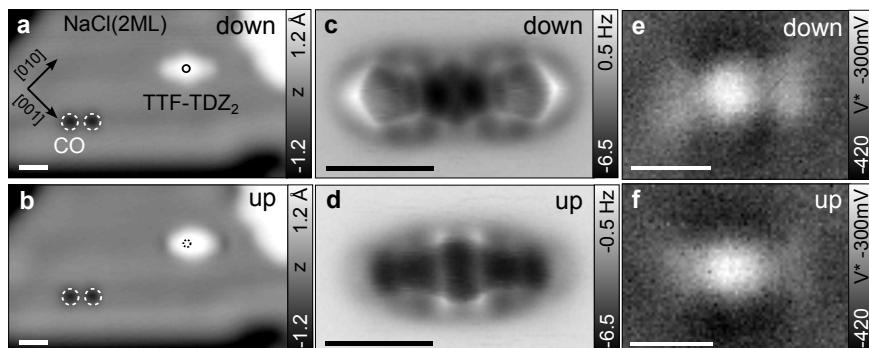


Figure 7.15.: **TTF-TDZ₂ on NaCl(2ML)/Cu(111).** **a,b** STM topographies ($I = 2$ pA, $V = 0.2$ V) of TTF-TDZ₂ in the 'down' (**a**) and 'up' (**b**) conformations recorded with a Cu tip. A voltage pulse of 0.8 V (at the position indicated by the black circle) was applied to switch between the conformations. A change in conformation is accompanied by a change in adsorption site from the TTF double bond on Cl top ('down') to a Cl bridge site ('up'). **c,d** AFM images of TTF-TDZ₂ in the 'down' (**c**) and the 'up' (**d**) conformation, obtained with a CO tip. **e,f** LCPD (V^*) map of TTF-TDZ₂ in the 'down' (**e**) and the 'up' (**f**) conformation using a Cu tip. Scale bars: 10 Å.

assembly of molecules) in which electronic charge (or fractions thereof) is transferred between different parts of the molecule upon excitation. The electron donating part is called donor, the electron accepting entity acceptor. The electron transfer is initiated by an electronic transition from the HOMO, localized on the donor, into the LUMO orbital, localized on the acceptor. This excitation is called intra-molecular charge-transfer transition and responsible for intense absorption bands in the electro-magnetic spectrum. The spatial separation of the HOMO and LUMO observed by STM has been previously reported¹⁷³.

Here we investigate the intra-molecular charge distribution of individual covalently linked donor-acceptor (polar) and acceptor-donor-acceptor (bipolar) CTCs^{174,175}. Thereby, the molecules under investigation were designed specifically as compactly fused donor-acceptor and donor-acceptor-donor entities (without large spacer groups). We make use of STM and AFM to determine and switch the molecular adsorption geometry and investigate its effect on the LCPD. Furthermore, we compare our measurements with calculations of the electrostatic field above the molecule. As a function of tip height, we find different molecular properties that are mapped by KPFM. Our results demonstrate that the information obtained by KPFM goes even beyond the determination of partial charges within the molecule.

We studied different CTCs with varying types [pyrazine (PYZ) or thiadiazole (TDZ)] and numbers (one or two) of acceptor components and a common tetrathiafulvalene (TTF) donor (see Fig. 7.14). As substrate, NaCl(2ML)/Cu(111) is used to decouple the molecules from metal states.

In Fig. 7.15 STM, AFM and KPFM measurements of the bipolar CTC TTF-TDZ₂ are shown. TTF-TDZ₂ on NaCl(2ML)/Cu(111) has two different conformational states (isomers) called 'up' and 'down' with different adsorption sites (see Fig. 7.16b,c). The chemical structure of the two states can be identified by AFM imaging of the molecule with a CO tip (see Fig. 7.15c,d)^{38,80}. In the 'down' state, the TTF part in the center is closer to the substrate than the molecule's ends, which therefore appear more pronounced and brighter than the central part in Fig. 7.15c. In contrast, for the 'up' state (Fig. 7.15d), the TTF part with its clearly visible four S atoms is sticking out. The Δf contrast difference between the outer and the center part is a consequence of the non-planar adsorption geometry and the high sensitivity of the short-range repulsive forces (Pauli repulsion) to changes of the tip-molecule distance^{125,126}. By applying voltage pulses of > 0.8 V or < -2.1 V, the molecule could be switched between the two states. Because the 'up' and 'down' conformations have different adsorption sites, each switching is accompanied by a lateral displacement of the molecule. The STM-induced conformation change and lateral manipulation are effects of inelastic tunneling electrons that can excite molecular vibrations⁹³.

Analogously to TTF-TDZ₂, also TTF-PYZ₂ has two different conformational states, 'up' and 'down', with different adsorption sites as shown in the adjusted constant height AFM images with a CO tip in Fig. 7.16f,g.

7. Molecular properties measured by AFM

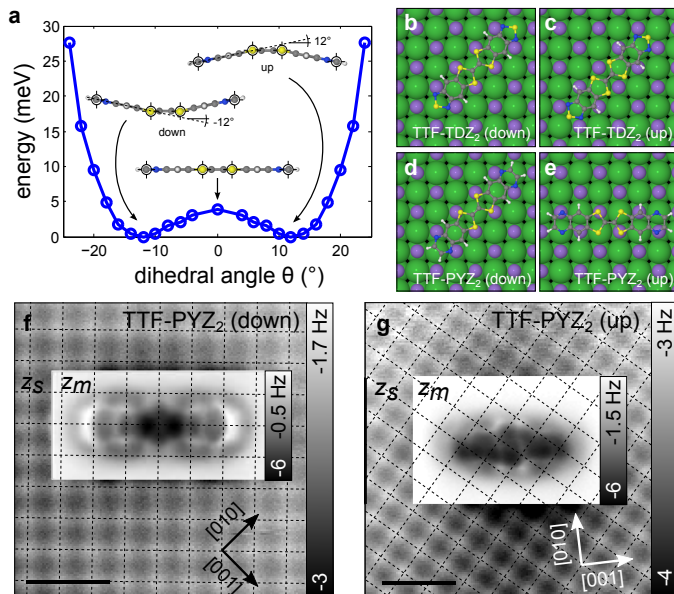


Figure 7.16.: **Adsorption geometry.** **a** Calculated energy profile for the dihedral bending at the four sulfur atoms of TTF-PYZ₂. The ground-state energy of the molecule is set to zero. The dihedral angle θ between the atoms marked by black cross-hairs was fixed in the calculations. **b/c** Model of the experimental adsorption site for TTF-TDZ₂ in the 'down'/'up' conformations. **d/e** Model of the experimental adsorption site for TTF-PYZ₂ in the 'down'/'up' conformation. Color code: H: white, C: gray, Cl⁻: green, N: blue, Na⁺: purple, S: yellow. **f,g** Adjusted constant height image of TTF-PYZ₂ in the 'down' (**f**) and 'up' (**g**) conformation with a CO tip (using two imaging heights, z_s and z_m). Note that for each imaging height, another contrast in Δf was chosen. The crossings of the dashed lines mark Cl atoms. Scale bars: 10 Å.

Interestingly, both molecules in the 'down' conformation are adsorbed with their sulfur atoms of TTF on top of Na sites. This can be explained by the attractive interaction between the Na⁺ ions and the lone pair of the sulfur atoms¹²⁵. Note that for TTF-PYZ₂ the molecule conformations could not be switched because they are restricted to different substrate directions. However, the molecules could be manipulated laterally with similar voltage pulses as TTF-TDZ₂ but without changing the adsorption site or the conformation. This is indicative of the common TTF part being decisive for the molecule hopping on NaCl, probably through excitation of the TTF flapping mode by inelastic tunneling electrons.

To corroborate our interpretation of the molecular geometry, we performed DFT calculations of the free TTF-PYZ₂ molecule with the highly optimized plane-wave code CPMD (see Appendix A for details). In the optimized geometry, we find indeed a boat-type geometry with a dihedral angle of $\theta = 12^\circ$ (see Fig. 7.16a). This is very close to $\theta = 13.5^\circ$ for bare TTF measured by gas electron diffraction¹⁷⁶. The calculated energy profile for the bending into a planar geometry is very shallow ($\Delta E \approx 4$ mV). This high flexibility¹⁷⁷ allows an easy transition between the 'up' and the 'down' boat state.

To gain insights into the charge state and charge distribution of the CTC and the effect of conformation on the aforementioned, we acquired maps of the LCPD above the molecules implemented by force-bias spectroscopy $\Delta f(V)$ ^{31,40,98,178}. From the individual parabolic $\Delta f(V)$ spectra, the peak voltage and the peak frequency shift ($V^*, \Delta f^*$) are extracted. This voltage V^* corresponds to the LCPD divided by the elementary charge. Maps of V^* , called LCPD maps in the following, are obtained by recording $\Delta f(V)$ spectra point by point in constant height mode on a lateral grid with a typical acquisition time of 15 h.

In Fig. 7.17e-h, LCPD maps of TTF-PYZ₂ and the corresponding maps of the LCPD-compensated frequency shift Δf^* are depicted. A CO tip has been used to explore also the small-distance regime. At moderate distance, the LCPD images recorded with a CO tip (Fig. 7.17e,g) resemble those obtained with a Cu tip (see Fig. 7.18a). In this regime we observe for both conformations ('up' and 'down') a similar LCPD contrast. Interestingly, the LCPD is increased at the positively charged donor as well as at the negatively charged acceptor sites as compared to the bare substrate. To the left and right of the molecule, the LCPD is decreased. This contrast contradicts the simple interpretation of LCPD maps (neglecting higher-order multipoles) of a positive/negative charge giving rise to a decreased/increased local work function and thus a decreased/increased LCPD. These findings are not specific to this particular molecule, but are also observed for TTF-TDZ₂ (see Fig. 7.15e,f).

With the CO tip, we can access the small-distance regime where Pauli repulsion sets in, and here the LCPD changes abruptly and significantly (Fig. 7.17f,h). At positions of repulsive interaction, the LCPD is decreased by several 100 mV. This LCPD decrease has the same high spatial localization as the repulsive Δf^* signal and sets in at the same imaging height, suggesting a correlation between Δf^* and the LCPD channel.

7. Molecular properties measured by AFM

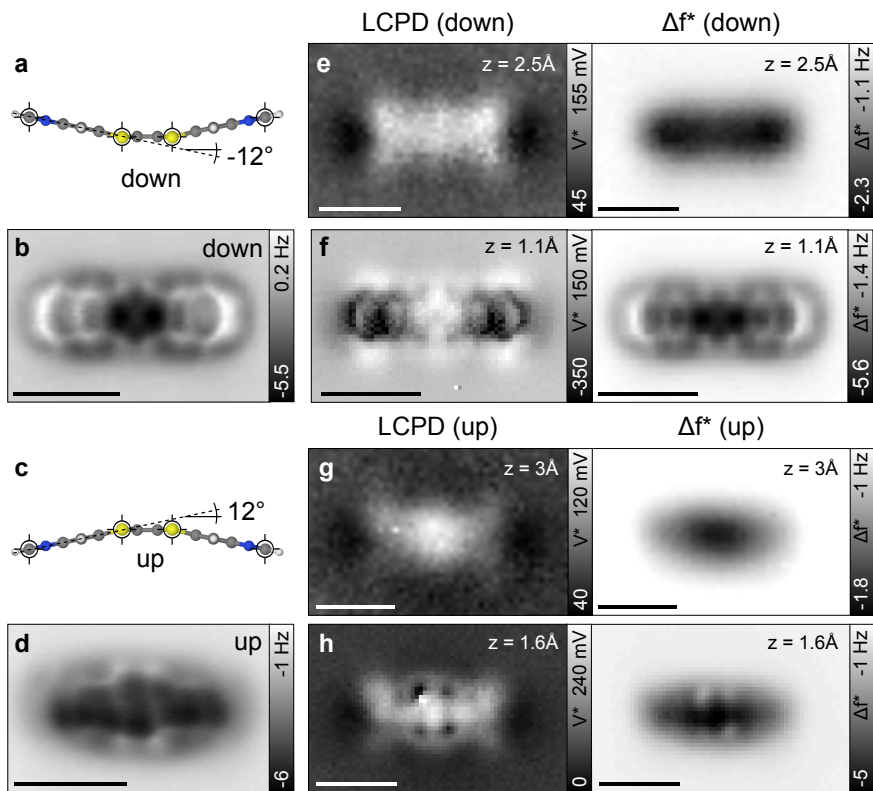


Figure 7.17.: **TTF-PYZ₂** **a/c** Side-view on the relaxed boat geometry of TTF-PYZ₂ in the 'down'/'up' conformation with the dihedral angle of $\theta = 12^\circ$ indicated. Color code: H: white, C: gray, N: blue, S: yellow. **b,d** AFM images of TTF-PYZ₂ in the 'down' (b) and 'up' (d) conformation with a CO tip. **e,f/g,h** LCPD (V^*) maps of TTF-PYZ₂ in the 'down'/'up' conformation at different heights z with a CO tip and the corresponding AFM maps at compensated LCPD (Δf^*). The heights are given with respect to a STM set point of ($I = 2 \text{ pA}$, $V = 0.2 \text{ V}$) over the substrate. Scale bars: 10 Å.

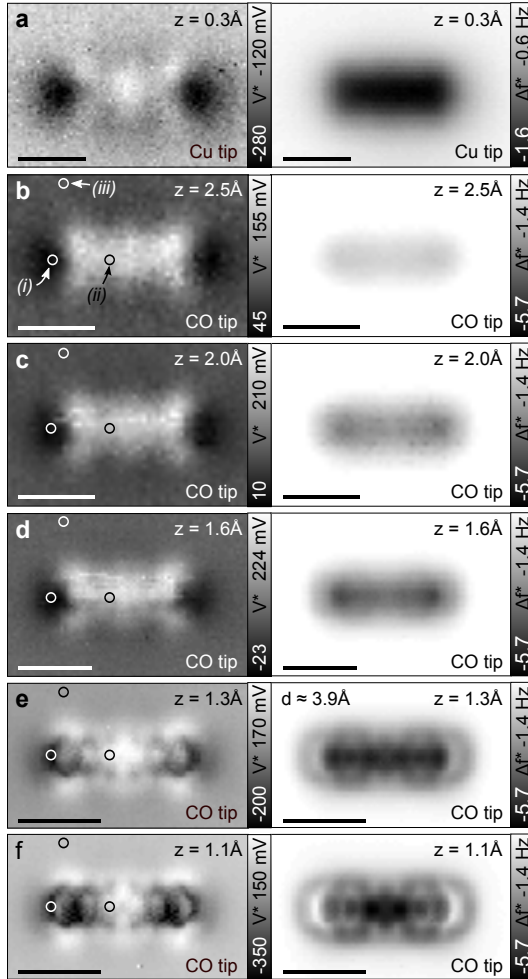


Figure 7.18.: **KPFM TTF-PYZ₂**. **a/b-f** LCPD (V^*) maps of TTF-PYZ₂ in the 'down' conformation at different heights z with a Cu/CO tip and the corresponding AFM maps at compensated LCPD (Δf^*). In measurements **b-f** the same CO tip was used. The heights are given with respect to a STM set point of ($I = 2$ pA, $V = 0.2$ V) over the substrate. In **e** $\Delta f^* \approx \Delta f_{\min}$ at the center of the carbon rings and the distance between the oxygen atom of the CO tip and the molecular plane can be estimated to be $d \approx 3.9$ Å^{38,112}. Individual $\Delta f(V)$ spectra at the three positions (i) – (iii) are shown in Fig. 7.19a-c. Scale bars: 10 Å.

7. Molecular properties measured by AFM

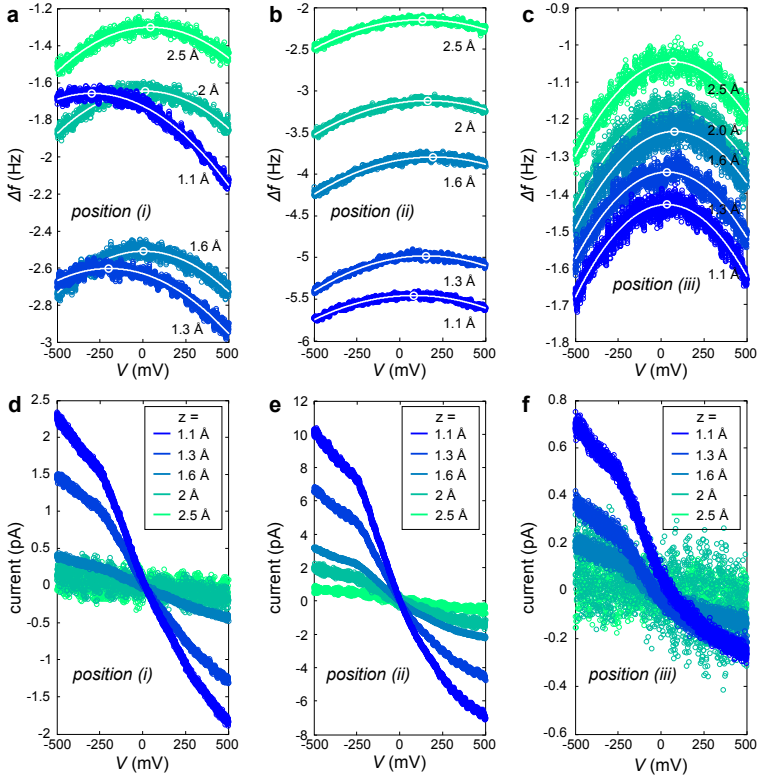


Figure 7.19.: **Individual $\Delta f(V)$ and $I(V)$ spectra.** **a-c** Individual $\Delta f(V)$ spectra at different heights $z = 1.1 - 2.5 \text{ \AA}$ extracted from the KPFM measurements and the positions (i) – (iii) indicated in Fig. 7.18b-f. For all measurement heights and positions there were no significant deviation from the parabolic $\Delta f(V)$ dependence observed. **d-f** Tunneling current recorded simultaneously with the Δf signal shown in **a-c**, respectively.

This can be clearly seen by comparing Δf^* and LCPD contrast for both conformations, for example, considering the four bright Δf^* spots and the four dark LCPD spots in Fig. 7.17h. The LCPD decrease at small distances could be explained by a local penetration of the tip in areas of significant electron density, which leaves the molecule's atomic cores partially unshielded. Consistently, the immersion of the tip into the extended π -orbitals leads to the repulsive Pauli interaction. Hence, the LCPD drops in region where the electron density is largest, i.e., in the small-distance regime the LCPD signal is dominated by the total electron density.

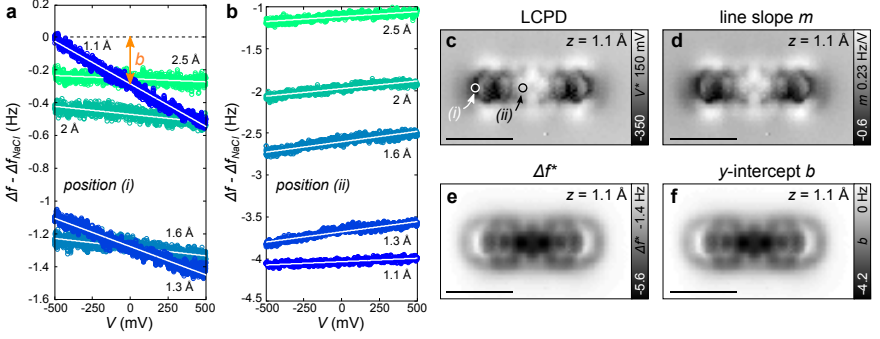


Figure 7.20.: **Difference spectra** **a,b** Difference spectra of the spectra shown in Fig. 7.19a,b and Fig. 7.19c: $\Delta f_{\text{diff}}(V, z) = \Delta f(V, z) - \Delta f_{\text{NaCl}}(V, z)$ for the positions (i) and (ii) at different heights z . The difference spectra linearly depend on V : $\Delta f_{\text{diff}}(V, z) = m(z)V + b(z)$. **c** LCPD at $z = 1.1$ Å. **d** Slope $m(z = 1.1$ Å) extracted from the difference spectra. **e** Δf^* map at $z = 1.1$ Å. **f** y -intercept $b(z = 1.1$ Å) extracted from the difference spectra. Scale bars: 10 Å.

In Fig. 7.19a-c individual $\Delta f(V)$ spectra, extracted from the measurements depicted in Fig. 7.18b-f, are shown. The position (i) corresponds to the left C-C bond, position (ii) is above the center of the left TTF ring and the position (iii) at the bare NaCl substrate. Note that for all measurement heights and positions we did neither observe significant deviations from the parabolic $\Delta f(V)$ dependence nor correlations to the tunneling current (shown in Fig. 7.19d-f).

Interestingly, all $\Delta f(V)$ parabolas at a certain height have roughly the same curvature. Subtracting the parabola on the substrate [position (iii)] from the parabolas recorded at (i) and (ii) results in straight lines (Fig. 7.20a,b). In general, one can consider a parabola of the form:

$$f_i(V) = -a_i(V - V_i^*)^2 + \Delta f_i^* \quad (7.3)$$

where the index i refers to a specific position (x_i, y_i) . By taking the difference of two parabolas that are required to have the same curvature a , one obtains

7. Molecular properties measured by AFM

$$f_2(V) - f_1(V) \stackrel{a_1 \stackrel{!}{=} a_2 = a}{=} \underbrace{2a(V_2^* - V_1^*)}_{\text{slope } m} \underbrace{V - a(V_2^{*2} - V_1^{*2}) + (\Delta f_2^* - \Delta f_1^*)}_{y\text{-intercept } b} \quad (7.4)$$

where m is the slope and b the y -intercept of the resulting straight line. By considering now a set of curves $f_2(V) = f(V, x, y)$ that are subtracted by a reference parabola $f_1(V) = f_{\text{ref}}(V)$ we obtain (provided all curvatures are equal) that the differences in their vertex points $V^*(x, y)$ are proportional to the slopes of their differences:

$$a(x, y) \stackrel{\text{exp}}{=} a \quad (7.5a)$$

$$\Rightarrow V^*(x, y) \propto m(x, y) \quad (7.5b)$$

This relation becomes apparent by comparing Fig. 7.20c and d, where $V^*(x, y)$ (Fig. 7.20c) and the slope from subtracting every $\Delta f(V)$ spectra by the reference spectra at point (iii) (Fig. 7.20d) exhibit the same contrast. We can also compare the y -intercepts $b(x, y)$ of these difference spectra with $\Delta f^*(x, y)$, which is shown in Fig. 7.20f and e, respectively. By looking at the Δf scale we can conclude that $b(x, y)$ essentially reflects the $\Delta f^*(x, y)$ map with subtracted background. By combining this experimental finding with eq. (7.4) it follows that

$$b(x, y) \stackrel{\text{exp}}{=} (\Delta f^*(x, y) - \Delta f_{\text{ref}}^*) \quad (7.6a)$$

$$\Rightarrow (\Delta f^*(x, y) - \Delta f_{\text{ref}}^*) \gg a(V^*(x, y)^2 - V_{\text{ref}}^{*2}). \quad (7.6b)$$

The right-hand side of this equation corresponds to the Δf difference between two sites at zero bias resulting from their different LCPD. This term is typically much smaller than the difference in Δf^* [left-hand side of eq. (7.6b)]. As a consequence, AFM images at zero bias usually closely resemble the Δf^* images, as discussed in section 6.3. Note that this is an empirical finding for this measurement and cannot be generalized.

Now we come back on the LCPD contrast on both bipolar CTCs. As discussed above, the LCPD contrast at moderate distance clearly contradicts the simple picture that it directly reflects the local charge in the molecule. Note that the LCPD contrast depicted in Fig. 7.17e and g is reminiscent

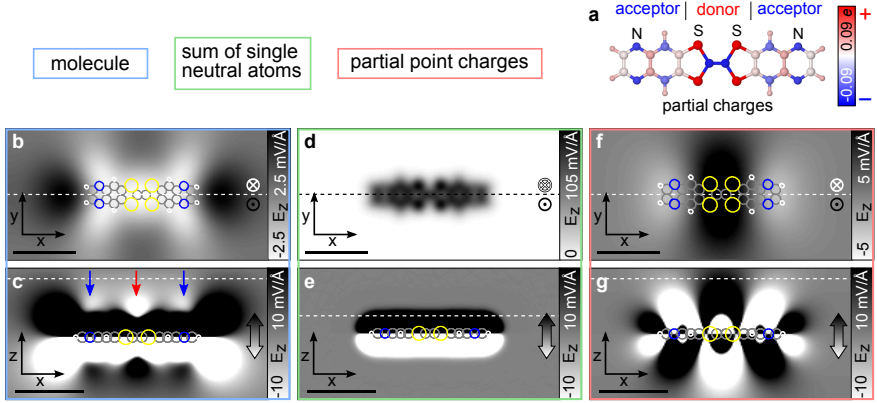


Figure 7.21.: **TTF-PYZ₂ theory** **a** DFT-calculated partial charges of TTF-PYZ₂ by real-space integration. **b** Calculated z -component of the electrostatic field (E_z) of the flat TTF-PYZ₂ at 8.6 Å away from the molecular plane (dashed line in **c**). **c** E_z in the x - z plane through the molecule's center (dashed line in **b**). Blue/red arrows indicate acceptor/donor positions. **d** Calculated E_z by assuming a set of non-interacting (spherical symmetric) neutral atoms in the TTF-PYZ₂ arrangement, at 2.5 Å away from the molecular plane (dashed line in **e**). **e** E_z in the x - z plane at the dashed line in **d**. **f** Calculated E_z generated by the partial point charges of TTF-PYZ₂ at 8.6 Å away from the molecular plane (dashed line in **g**). **g** E_z in the x - z plane at the dashed line in **f**. In **b,c,e,f,g** the molecule structure is overlaid (color code: H: white, C: gray, N: blue, S: yellow). Scale bars: 10 Å.

of two opposing dipoles in the order (+ −) and (− +). But in this CTC molecule, the sequence is exactly opposite: acceptor (−) to the left, donor (++) in the center and acceptor (−) to the right.

Interpretation of the KPFM contrast. To understand the apparently conflicting contrast of the measured and expected LCPD, we calculated the electrostatic field and partial atomic charges of the free, planar TTF-PYZ₂ molecule. The use of the planar instead of the boat geometry for these calculations is justified at larger distances because of the small differences of the LCPD and the Δf^* channel for both conformations at moderate height. The insulating NaCl layer provides an electronic decoupling and prevents hybridization and partial charge transfer with metal states. Since the molecule is neutral, we do not expect strong modifications of the surface dipoles as on metals. This allows us to compare the measurements on NaCl with calculations of the free molecule. It is an observation that

7. Molecular properties measured by AFM

the measured V^* contrast at the atomic scale qualitatively reflects the z -component of the electrostatic field (E_z) created by the sample^{40,94}. A quantitative comparison is challenging due to the different work functions of the mesoscopic tip and sample surfaces and the resulting averaging effects³¹. Fig. 7.21b shows E_z in the x - y plane 8.6 Å above the molecule^a. In comparison with Fig. 7.17e,g, the measured LCPD contrast is well reproduced by E_z showing only slight deviations that can be attributed to the nonplanar geometry.

In the following, we will describe which aspect of the molecular charge distribution will contribute in which way to the molecular E -field. In first order, the charge distribution of the molecule can be described by a set of single non-interacting neutral atoms with spherical symmetric charge distributions. The E_z -field from this charge distribution is displayed in Fig. 7.21d,e. We observe a short-ranged field that points away from the molecule in regions of significant electron density and is zero in the far field. For small distances this effect is predominant and resembles the total electron density that is also probed by the Δf^* signal. However, it cannot be decisive for medium and larger distances. A second major component is the E -field produced by the partial atomic charges resulting from polarization of bonds. This field has considerable multipole moments and can have large contributions in the medium- and large-distance regimes. In Fig. 7.21a, the partial atomic charges of the bipolar TTF-PYZ₂ molecule are illustrated obtained by a Bader charge analysis¹⁷⁹. As expected, the N heteroatoms of PYZ act as electron acceptors with a net electron excess of 0.07 e , whereas electrons are depleted at the TTF donor. The corresponding E -field generated by these point charges is shown in Fig. 7.21f,g. Note that E_z beyond the small-distance regime (Fig. 7.21f) resembles a field of two opposing dipoles ($- + + -$), the expected behavior of the bipolar molecule in the point-charge notion. Apparently, the sum of the fields generated by the spherical symmetric electron distribution and partial atomic charges does not result in the calculated (and measured) molecular E -field. The missing crucial factor, not considered so far, is the complex three-dimensional distribution of the electron density.

In the case of the bipolar TTF-PYZ₂ molecule, this effect even leads to an inversion of the E_z contrast above donor and acceptor positions

^aThe height was adjusted to reproduce the measured LCPD contrast in Fig. 7.17e,g. But as seen in Fig. A.1 in the appendix, the contrast of E_z beyond $z \approx 5$ Å qualitatively no longer changes significantly.

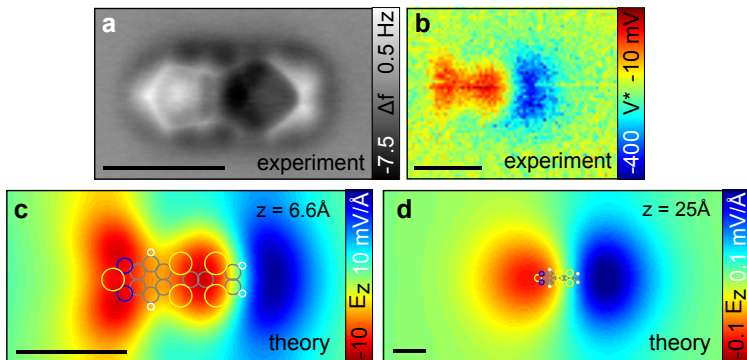


Figure 7.22.: **Polar TTF-TDZ** **a** AFM image of TTF-TDZ with a CO tip. Similarly to TTF-TDZ₂ and TTF-PYZ₂ also TTF-TDZ has boat-like geometry. **b** LCPD (V^*) map of TTF-TDZ using a Cu tip. **c,d** Calculated z -component of the electrostatic field (E_z) at different heights z with a molecule model overlaid. In **d** the far field of the molecular dipole is visible. Scale bars: 10 Å.

(compare Fig. 7.21b with Fig. 7.21f). The resulting E -field, which is in agreement with the experiment, is reminiscent of two opposing dipoles in the orientation (+ − + −) although the dipoles in the molecule are oriented (− + + −). This finding demonstrates that the LCPD image of a molecule cannot be broken down into an assembly of partial point charges located at the atom positions, but that the complex electron distribution in space has to be considered. Note that this effect of the electron distribution can be elegantly accounted for when measuring the charge transfer. However, this is possible only for stable molecular conformations with different charge distributions by looking at the difference of their LCPD maps⁴⁰.

To investigate the far-distance regime, we also examined the polar TTF-TDZ molecule, which has a nonvanishing lateral dipole moment ($p = 4.2\text{D}$). For TTF-TDZ, the measured LCPD shown in Fig. 7.22c is also in very good qualitative agreement with E_z (c.f. Fig. 7.22d). Although the E -field at medium distance is again more complex than its lowest-order multipole moment, it contains large contributions from the molecular dipole. In the far field, the calculated E -field converges to a simple dipole field (see Fig. 7.22e) in agreement with the expected behavior of a donor-acceptor molecule. Note that at these large distances the LCPD signal from the molecule is below our experimental limit of detection.

7. Molecular properties measured by AFM

In summary, we investigated the bipolar CTCs TTF-PYZ₂ and TTF-TDZ₂ and the polar CTC TTF-TDZ on NaCl(2ML)/Cu(111) using STM, AFM and KPFM. Both bipolar molecules show two conformational states 'up' and 'down', that were identified by AFM with CO-functionalized tips and corroborated by DFT. In KPFM, three main distance regimes were identified that exhibit quantitatively different contrast and are related to different aspects of the charge distribution within the molecule: At distances much larger than the molecule dimensions, the LCPD contrast resembles the electrostatic far-field with predominant contributions of the molecular electric monopole (net charge) and dipole. At distances similar to the molecule dimensions, the LCPD contrast corresponds to the electrostatic field with predominant contributions from higher-order multipoles caused by partial atomic charges and the complex three-dimensional electron distribution. At very small distances, which can be explored with a CO-terminated tip, the tip penetrates the electron density of the molecule^a. As a result, the molecule's nuclei are left partially unshielded, and the LCPD shows a strong decrease of several 100 mV at positions of high total electron density, in agreement with the occurrence of repulsive Pauli interaction. Only in this small distance regime do the tip and the adsorption geometry of the molecule play an important role for the LCPD measured.

^aAnother interpretation by Christian Lotze *et al.*¹⁸⁰ assumes the effect might be caused by polarizing the sample molecule with the tip.

CHAPTER 8

Chemical structure identification

If you have a strange substance and you want to know what it is, you go through a long and complicated process of chemical analysis. [...] It would be very easy to make an analysis of any complicated chemical substance; all one would have to do would be to look at it and see where the atoms are.

“There’s Plenty of Room at the Bottom”
Richard P. Feynman

The identification of molecular structures is an important emerging application of high-resolution molecular imaging by AFM with functionalized tips (typically CO tips). Recently, AFM was used in combination with nuclear magnetic resonance (NMR) for the structure elucidation of a natural product³⁹. Moreover, AFM was employed to identify reaction products formed by atomic manipulation²⁷ and by on-surface chemistry¹³⁸.

In this chapter we will first discuss the structure verification of a synthesized large polyaromatic hydrocarbon. Then, the structure elucidation of a newly discovered natural product is demonstrated where AFM assisted in its identification. In section 8.3 we then applied this technique to analyze one of the most complex natural mixtures existing. Gaining deep insights into the structural diversity of this material, a task that was impossible before. Thereafter, general conclusions are drawn in which cases AFM is beneficial for structure identification of molecules, based on the previously discussed examples.

8.1. Trinaphthaloperylene (TNP): Giant nanographene

Most of the content presented in this section has been published in Angewandte Chemie International Edition^a [181](#). Text excerpts and figures are reproduced by permission of Wiley-VCH publishing.

One of the biggest challenges that needs to be addressed in graphene science is the development of efficient methodologies for the preparation of this material with defined size, shape and quality^{[182](#)}. This is particularly important for device fabrication, since it is extremely difficult to create homogeneous nanosized graphenes with well-defined edges – a crucial issue for controlling and tuning the properties of this material^{[183,184](#)}. In this respect, the chemistry-driven bottom-up approaches to graphene materials have emerged as privileged methods to access nanostructures such as graphene nanoribbons or graphene quantum dots^{[185](#)}. In particular, organic chemistry methodologies in solution have been used during the last century to obtain polycyclic aromatic hydrocarbons (PAHs) and, given the structural similarities between graphene and PAHs, this approach can be especially useful to obtain large graphene molecules^{[186](#)}. However, a number of drawbacks associated with the use of these bottom-up approaches to nanographenes by solution chemistry have been identified, and these include: (i) The extremely low solubility of planar aromatic molecules, due to efficient intermolecular π -stacking, makes it difficult to characterize and manipulate these materials. (ii) The lack of volatility due to the large size hampers the integration of molecules into devices. (iii) The number of reactions that are suitable to obtain graphene molecules is very small and this limits the edges and shapes that can be achieved. In this section we discuss a contribution that attempts to overcome these drawbacks by introducing the nanographene trinaphthaloperylene (TNP) (see Fig. [8.1a](#)), a large PAH with 22 fused benzene rings, which was prepared in solution, isolated, sublimated and characterized on a surface.

This unsubstituted graphene molecule was synthesized by means of two sequential aryne cycloaddition reactions starting from perylene (**1**), a readily available PAH with five fused benzene rings. The synthesis procedure is illustrated in Fig. [8.1a](#). It is notable that this molecule can be obtained in a straightforward manner from both commercially available perylene (**1**)

^aSchuler, B., Collazos, S., Gross, L., Meyer, G., Pérez, D., Guitián, E. & Peña, D. From perylene to a 22-ring aromatic hydrocarbon in one-pot. *Angew. Chem. Int. Ed.* **53**, 9004-9006 (2014).

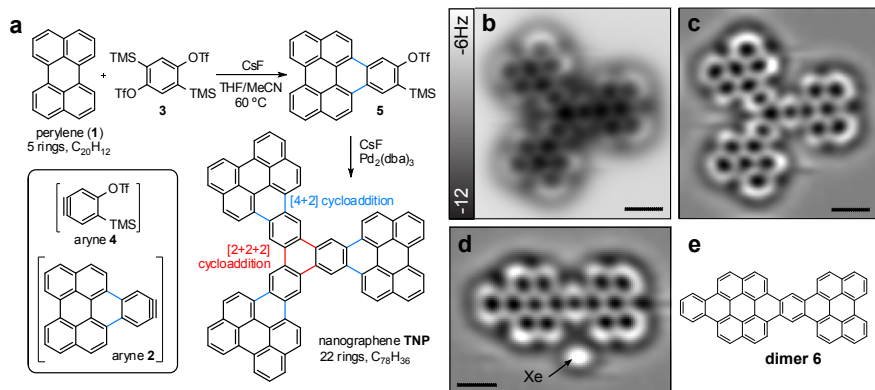


Figure 8.1.: **Trinaphthoperylene (TNP) synthesis and structure.** **a** Synthetic route of TNP. Functional groups: Trimethylsilyl (TMS), triflate (OTf), tetrahydrofuran (THF). **b** AFM image of TNP on NaCl(2ML)/Cu(111) with a CO tip. **c** Laplace filtered data of **b**. **d** AFM image of the arylene dimer **6**. **e** Structure of the arylene dimer **6**. Scale bars: 5 Å.

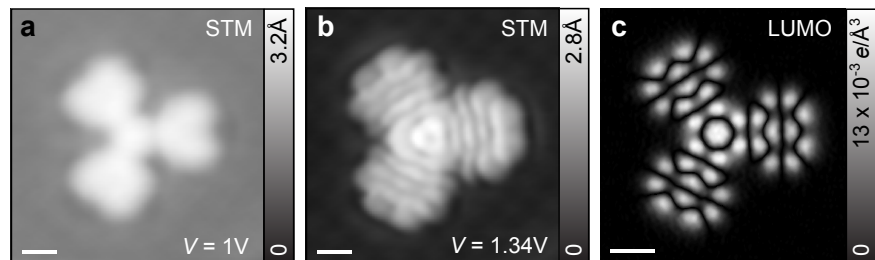


Figure 8.2.: **TNP LUMO.** **a/b** STM image ($I = 2 \text{ pA}, V = 1 \text{ V}$)/($I = 2 \text{ pA}, V = 1.34 \text{ V}$) of TNP on NaCl(2ML)/Cu(111) using a CO tip. Measurement in **a** is acquired in the HOMO-LUMO gap and measurement in **b** correspond to the LUMO resonance. **c** Calculated orbital density squared of the LUMO at a distance of 1.2 Å above the molecular plane. Scale bars: 5 Å.

and bisbenzyne precursor **3** in one pot without the need to isolate arylene precursor **5**. For further details on the synthesis, please see Ref. 181. Note that we could also generate and analyze the reactive intermediate arylene **2** by STM and AFM, which is discussed in section 9.1.1.

The extreme insolubility of this solid precluded characterization by conventional methods such as NMR spectroscopy. Therefore we attempted

8. Chemical structure identification

the confirmation of the molecular structure of TNP by AFM. The TNP sample was flashed by direct-current heating directly from a Si wafer, onto NaCl(2ML)/Cu(111) at $T = 10$ K. Most adsorbents we assigned to fragments of TNP, which one would expect to decompose when heated to its sublimation temperature due to its large size. However, evidence for some cloverleaf shaped molecules was found and detailed inspection by AFM with a CO-functionalized tip confirmed the presence of the nanographene TNP (Fig. 8.1b,c). STM (Fig. 8.2a,b) was also carried out in order to obtain molecular orbital images²⁶ and CO tips were again employed to increase resolution⁴¹. The measured image of the negative ion resonance (Fig. 8.2b) corresponds to the LUMO of TNP as seen by comparison with the calculation of its orbital density squared (Fig. 8.2c), thus confirming the presence of the intact TNP molecule.

Surprisingly, the AFM experiments revealed the presence of tetranaphthoheptacene **6** (Fig. 8.1d,e), a 15-ring PAH which is not a fragment of TNP. It is plausible that this compound was obtained by a sequence of reactions initiated with the [4+2] cycloaddition of aryne **2** with a bay region of triflate **5**. The isolation of this face-to-edge dimer of aryne **2** is particularly interesting, since the iterative version of this transformation could provide a new bottom-up approach to graphene nanoribbons, which regularly combine zig-zag and armchair edges.

In conclusion, large PAHs can be obtained from perylene by following an extremely simple procedure. This example demonstrates the potential and simplicity of aryne chemistry in solution to build nanographenes by a bottom-up approach, in which the formal triple bond of the aryne acts as a molecular glue to paste aromatic fragments together. Importantly, the work described here shows how atomic-resolution scanning probe microscopy techniques can provide synthetic chemists with unique tools for the identification of insoluble graphene molecules.

8.2. Breitfussin A: Single molecule case study

*Most of the content presented in this section has been published in *Angewandte Chemie International Edition*^{a187} Text excerpts and figures are reproduced by permission of Wiley-VCH publishing.*

Nature offers an inexhaustible and only partially explored source for small (biologically active) molecules, often with potential pharmaceutical applications. Especially the marine environment offers very diverse and unique habitats for organisms providing a large range of novel chemical structures. For structure identification of such natural products a bunch of well-established characterization methods exist, particularly, x-ray crystallography and spectroscopic techniques such as mass spectrometry (MS) and NMR. However, for certain classes of molecules *ab initio* structure analysis can be very challenging particularly for samples that hardly crystallize, that are sparsely hydrogenated or are available in insufficient quantities. In these cases, the conventional techniques may not succeed in the unambiguous determination of the chemical structure of the unknown compound.

Using high-resolution AFM as a complementary and direct tool for structure recognition is very appealing. Specifically, there is great potential for the structural characterization of planar, proton-poor compounds, as these compounds are prone to structural corrections^{39,188,189}. The first molecule determined using AFM was Cephalandole A³⁹, a molecule that was previously found in a Taiwanese orchid. Here we used AFM to assist in the structure elucidation of the formerly unknown molecule Breitfussin A. AFM was used in combination with spectroscopic methods, computer-aided structure elucidation (CASE)¹⁹⁰, and DFT to solve the structure, which could not be solved using either method alone.

The subject of this study was the arctic hydrozoan *thuiaria breidfussi* (family sertulariidae) (see Fig. 8.3a). Arctic marine environments support highly diverse and dense populations of marine invertebrates¹⁹¹. The sample of *thuiaria breidfussi* was collected from a sediment near Bjørnøya (bear island) in 2007, extracted with MeOH/CH₂Cl₂ and purified by the

^aHanssen, K. Ø., Schuler, B., Williams, A. J., Demissie, T. B., Hansen, E., Andersen, J. H., Svenson, J., Blinov, K., Repisky, M., Mohn, F., Meyer, G., Svendsen, J. S., Ruud, K., Elyashberg, M., Gross, L., Jaspars, M. & Isaksson, J. A combined atomic force microscopy and computational approach for the structural elucidation of Breitfussin A and B: Highly modified halogenated dipeptide from thuiaria breidfussi. *Angew. Chem. Int. Ed.* **124**, 12404-12407 (2012).

8. Chemical structure identification

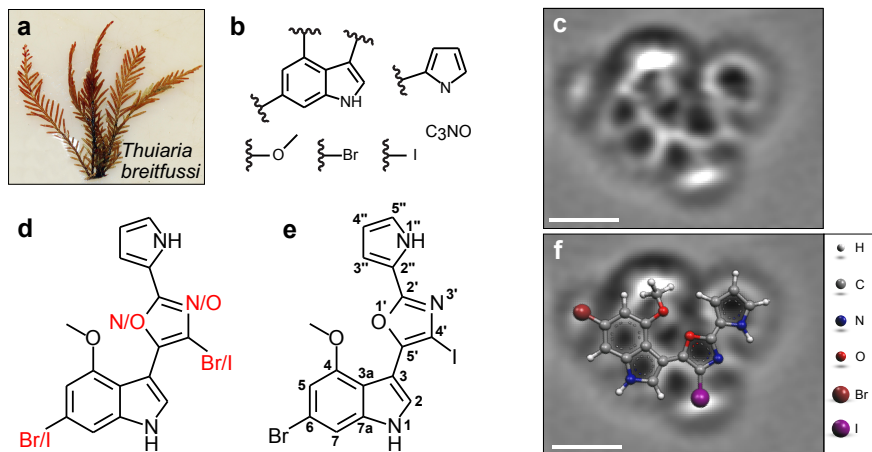


Figure 8.3.: **Breitfussin A.** **a** *Thuiaria breitfussi* photograph by Robert Johansen ©Marbank. **b** Substructures of Breitfussin A initially derived by mass spectrometry, ^1H and ^{13}C NMR spectroscopy. The substructures can be assembled in more than 1000 different ways. **c** Laplace-filtered AFM image of Breitfussin A imaged with a CO tip. **d** The four remaining constitutional isomers after AFM inspection. **e** Final structure of Breitfussin A. **f** Image **c** with a structure model of Breitfussin A overlaid. Scale bars: 5 Å.

group of Johan Isoksson yielding 6.2 mg of Breitfussin A. High-resolution mass spectrometry (MS) yielded the molecular formula $\text{C}_{16}\text{H}_{11}\text{N}_3\text{O}_2\text{BrI}$. The small amount available and limited purity of the sample prevented the analysis by diffraction methods. The fragmentation analysis by MS revealed fragments corresponding to the loss of I, CH_3O , Br and CH_3 . The ratio of heavy atoms to protons (ca. 2:1) indicated that structure determination by spectroscopic methods would be challenging. In Fig. 8.3b the derived substructures by MS, ^1H and ^{13}C NMR are shown (performed by the group of Marcel Jaspars), consisting of indole, pyrrole, a methoxy group, Br, I and a C_3NO fragment (for details see Ref. 187). Eventually, the small H abundance and large number (> 1000) of grouping possibilities of the identified substructures prevented the unambiguous assignment by spectroscopic methods alone.

Atomically resolved AFM measurements (see Fig. 8.3c) revealed a bicyclic system that includes a 5-membered ring and two additional connected rings where the symmetry could not be resolved unambiguously owing to the heteroatoms. Thus, the indole fragment could be readily confirmed. Fur-

thermore, the connection points of the rings at 3,5' and 2',2'' could be determined. Br and I are imaged as elongated single spots, which could be the result of their anisotropic electron distribution. The halogens are connected at 6 and 4' or vice versa to the ring system. Furthermore, we could allocate the major spot in the upper part of Fig. 8.3c,d as the bulky MeO moiety. Consequently, the four structures illustrated in Fig. 8.3d (remaining the ambiguity between the positions of Br, I and N, O, respectively) are consistent with the MS, NMR, and AFM experimental data.

The largely reduced amount of possible working structures from more than thousand to only four by AFM enabled the inspection of the experimental NMR data by CASE, performed by Kirill Blinov. The resulting structure with the best agreement between the measured chemical shifts and chemical shifts calculated from database entries of the possible substructures is shown in Fig. 8.3e (for details see Ref. 187).

The only remaining possible ambiguity is the practically unlikely but theoretically possible switch of the oxazole nitrogen and oxygen positions, which cannot be directly assessed by any of the above methods. Although the CASE analysis ranks the final suggested structure (Fig. 8.3e) higher than any other possible configurations of this ring, there is an intrinsic risk of bias towards known structures owing to database coverage. To rule this out, DFT chemical shift calculations^{192,193} were performed on the two reshuffled configurations of the oxazole ring. The calculated chemical shifts all show the least average error for the proposed structures compared to any other configuration for both ^{13}C and ^1H shifts. Thus, both DFT calculations and the database approach are in agreement with respect to the silent atoms in the oxazole.

In Fig. 8.3f the final structure of Breitfussin A is overlaid on the AFM map. Note that I is imaged with increased contrast compared to Br, which can be explained by the additional filled shell and the corresponding larger atomic radius of I compared to Br. Structurally, Breitfussin A defines a novel class of highly modified halogenated dipeptide comprising a rare molecular framework, with the combination of an indole, oxazole, and a pyrrole. Very recently, the total synthesis of Breitfussin A was reported¹⁹⁴, which verified the structure assignment described above.

The presented approach for structure elucidation by AFM, pioneered by Gross *et al.*³⁹, highlighted its general strengths and limitations and let us foresee possible impacts of AFM on molecular structure elucidation that

8. Chemical structure identification

we will briefly discuss next.

The obtained results for Breitfussin A emphasizes the strength of AFM to identify the carbon network and bond positions connected to it. It also manifests the problems of NMR concerning assignment of carbon rings interrupted by heteroatoms and the determination of bond positions. Major limitations of the AFM method arise from the fact that molecules are usually not planar, and even small deviations from a planar geometry complicate both measurement and analysis (cf. section 7.3). Partly, the geometry problem can be accounted for by the 3D force mapping technique with variable tip approach⁷⁷ where the closest tip approach is adapted to the molecular geometry. However, keeping in mind that about 30% of misassigned natural molecules of marine origin between 1975–2009 are planar or have planar moieties³⁹, a large number of molecules become suited for the AFM approach. Another major issue is the limited chemical sensitivity. The chemical sensitivity may be increased by using different tip functionalizations (see chapter 6): In case there is a lack of resolution in certain molecule parts, as a consequence of smaller chemical interaction, another tip functionalization can be tested that has higher or different chemical sensitivity. A missing systematical interpretation scheme or database for high-resolution AFM imaging is in this respect a clear handicap. Inspired from studies by Sugimoto *et al.*³⁶, it is expected that chemical sensitivity within molecules is also achieved by atomic force spectroscopy superseding different tip terminations. A big advantage of the introduced method above is the tiny amount of material that is necessary for the AFM inspection. It can be estimated that about 10 pmol, i.e. roughly 5 ng of material is required, which is about four orders of magnitude smaller than in NMR. Hence, structure identification employing high-resolution AFM is especially suited for rare, proton-poor compounds where crystallization is impractical or impossible, which often applies for natural products.

In general, the suggested *modus operandi* for structure identification of purified natural products by AFM would be that MS and NMR provide initially the molecular mass formula and possible molecule moieties. Then AFM yields the relative positions of these moieties and heteroatoms in the molecule structure and adds, confirms or eliminates possible molecule moieties, which also reduces the NMR inherent operator bias. From these considerations one or several working structures are worked out, each of which must be tested against, and be consistent with, the spectroscopic and AFM data. If necessary, the NMR spectra or AFM contrast from these work-

8.3. *Asphaltenes: Unraveling the chemical structure of a complex mixture*

ing structures are finally calculated and compared with the measurements, yielding hopefully an unambiguous structure assignment. Consequently, this procedure allows saving computation time (by decimating the number of working structures), avoiding possible misassignments and corroborates the structural assignment.

8.3. **Asphaltenes: Unraveling the chemical structure of a complex mixture**

In nature, molecules generally exist in mixtures. Petroleum is probably the most prominent of such mixtures and one of the most complex materials encountered with possibly over 100,000 distinct chemical constituents^{195,196}. The primary unresolved component of crude oil is its solid component, the asphaltenes^{196–198}. Understanding the structure of asphaltenes is of immense economic importance^{196,198–202}, and a prerequisite to establishing the structure–function relationship in petroleomics¹⁹⁶, but their molecular architecture has been subject to a long-standing debate^{197,203–207}. Asphaltenes are linked to many key economic issues in the petroleum industry today. Unwanted asphaltene phase transitions hinder petroleum production, transportation and refining^{196,198}. Asphaltene interfacial activity with rock affects wettability, offering a focal point for enhanced oil recovery²⁰². In addition, understanding chemical processes that occur in oil reservoirs^{200,201} is improved by accurate structural characterization. The capability to address all these concerns is founded on an accurate representation of asphaltene molecules. However, the structure analysis of asphaltenes has posed an exceptional challenge because of their chemical complexity that is only now being resolved²⁰⁸.

In the following, we present atomic-resolution AFM data of individual molecules of asphaltene, one of the most complex and intriguing natural mixtures existing. Additionally, orbital imaging with the STM is used to access the polycyclic aromatic hydrocarbon (PAH) moieties of asphaltene, their primary site of inter-molecular interaction. We compare asphaltenes from different sources: (i) Coal-derived asphaltenes (CAs) and (ii) petroleum asphaltenes (PAs). A STM overview image of the CA sample preparation is shown in Fig. 8.4a. All STM and AFM measurements shown in this section were recorded with a CO tip either on Cu(111) or NaCl(2ML)/Cu(111).

8. Chemical structure identification

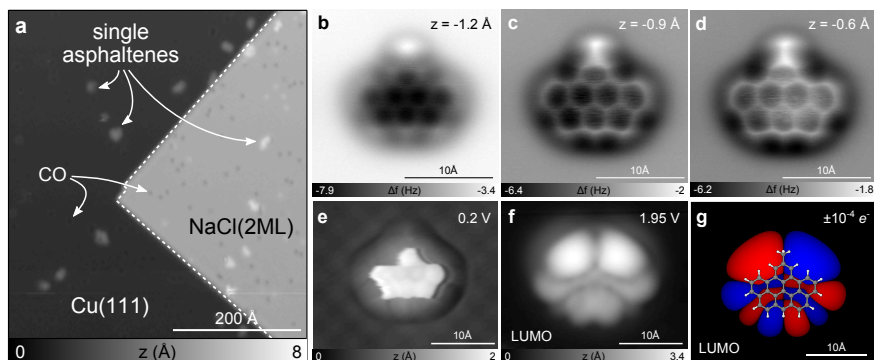


Figure 8.4.: **Coal-derived asphaltene sample preparation and CA1.** **a** STM overview image ($I = 1$ pA, $V = 0.5$ V) of the CA sample on NaCl(2ML)/Cu(111). **b-d** AFM images of **CA1** on NaCl(2ML)/Cu(111) at different set-points z from ($I = 1.4$ pA, $V = 0.2$ V). **e** STM image of **CA1** ($I = 10$ pA, $V = 0.2$ V). **f** STM image at the NIR ($I = 1.4$ pA, $V = 1.95$ V). **g** LUMO orbital of **CA1** with the molecular structure overlaid as a guide to the eye.

The combined use of AFM and STM for structure identification is demonstrated in Fig. 8.4b-f. AFM is used to propose a hypothesis of the molecular structure, including some side-groups. If molecular orbitals are accessible by STM, they can corroborate or refute the hypothesis. In Fig. 8.4b-d, AFM measurements of the CA molecule **CA1** on NaCl(2ML)/Cu(111) are shown. This specific specimen has eight fused benzene rings with a small side-group attached at the topmost ring that we identified as CH_3 (see Supplementary Information of Ref. 209 for comparison with a control compound). The good agreement between the measured LUMO resonance (Fig. 8.4f) and calculated LUMO (Fig. 8.4g), using the structure hypothesis from AFM, supports this structural assignment.

The molecule **CA2** (Fig. 8.5a-d) consists of eight fused benzene rings, subdivided into two aromatic parts: A pyrene and a methyl-substituted benzo[*c*]phenanthrene moiety connected by a central five-membered ring. For this molecule, LUMO (Fig. 8.5c) and HOMO (Fig. 8.5d) were accessible. They are in reasonable agreement with the calculated orbitals (see Fig. A.3), which are again based on our structure hypothesis from AFM. In Fig. 8.5e, an AFM image of **CA3** is shown. In regions where the contrast is weak, a Laplace-filtered image (Fig. 8.5f) reveals additional details. In addition, the orbital images of the LUMO and HOMO

8.3. Asphaltenes: Unraveling the chemical structure of a complex mixture

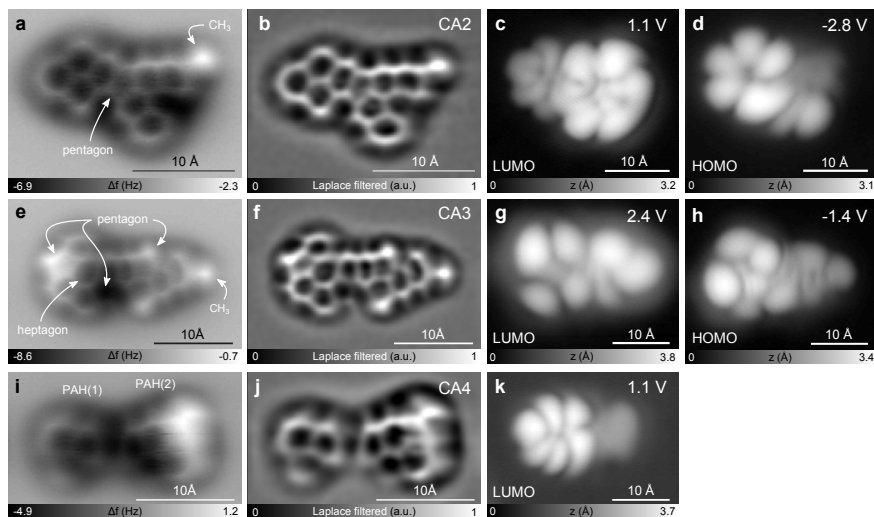


Figure 8.5.: **Coal-derived asphaltenes CA2-CA4.** **a,b** AFM image of **CA2** on NaCl(2ML)/Cu(111) (**a**) and the Laplace-filtered image (**b**). **c,d** STM orbital images ($I = 1.4$ pA) of **CA2** corresponding to the LUMO and HOMO resonance, respectively. **e,f** AFM image of **CA3** on NaCl(2ML)/Cu(111) (**e**) and the Laplace-filtered image (**f**). **g,h** STM orbital images ($I = 1.4$ pA) of **CA3** corresponding to the LUMO and HOMO resonance, respectively. **i,j** AFM image of **CA4** on NaCl(2ML)/Cu(111) (**i**) and the Laplace-filtered image (**j**). **k** STM orbital image of **CA4** corresponding to the LUMO resonance.

(Fig. 8.5g,h) were used to further elucidate the molecular structure (see discussion in appendix A.2). Importantly, structural information mediated by orbital imaging is accessible in many cases where AFM cannot resolve the structure directly. **CA3** comprises other structural motifs, such as a fluorene moiety featuring a methylene bridge, and a seven-membered ring.

In some cases (although in minor quantities), we also find CAs that have several (up to four) PAH islands connected by single covalent bonds. **CA4**, presented in Fig. 8.5i-k, comprising two non-resonant PAHs, is such an example. Consequently, the LUMO (Fig. 8.5k) is delocalized only over one side of the molecule. Another clear example of a molecule featuring two PAHs connected by a single bond is **CA16** in Fig. 8.6l. This is a direct detection of the ‘archipelago’-type architecture reported in other publications²⁰⁷. However, in contrast to previous suggestions, we never observed PAHs that were connected by chains longer than a single bond.

8. Chemical structure identification

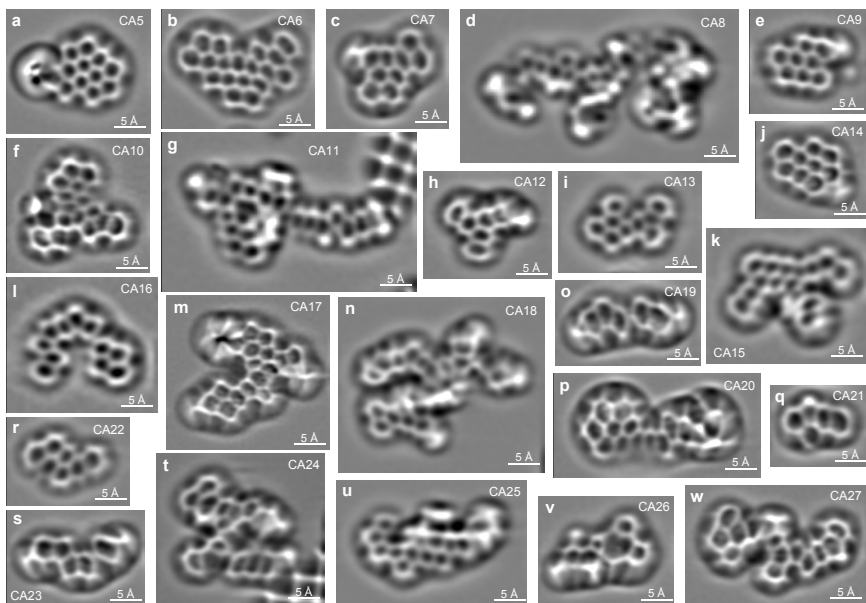


Figure 8.6.: **Coal-derived asphaltenes CA5-CA27.** **a-w** Laplace-filtered AFM images of different CAs on Cu(111) or NaCl(2ML)/Cu(111). In **g** and **t**, a small patch of third-layer NaCl is also imaged.

Orbital imaging is in general an expedient complement to the atomic-resolution AFM images. It provides information about the delocalization of electrons in the frontier molecular orbitals, hence the degree of conjugation of the PAH core, and an independent cross-check for testing a structure hypothesis from AFM. The HOMO–LUMO gap, which is closely related to the difference between the NIR and the positive ion resonance (PIR)^a that we can measure here, is also an indicator for the stability of the molecule²¹⁰. This stability is expected to be exceptionally high for asphaltenes inferred from their long lifetimes on the order of geologic timescales²¹¹.

In Fig. 8.6 other atomic-resolution images of CAs are shown. The huge diversity of the different structures observed is formidable. In all of the about 100 atomic-resolution AFM measurements of CAs taken, we never

^aNIR/PIR are related to the electron affinity and ionization energy of the molecule, respectively, by considering the polarizability of the substrate²⁶.

8.3. Asphaltenes: Unraveling the chemical structure of a complex mixture

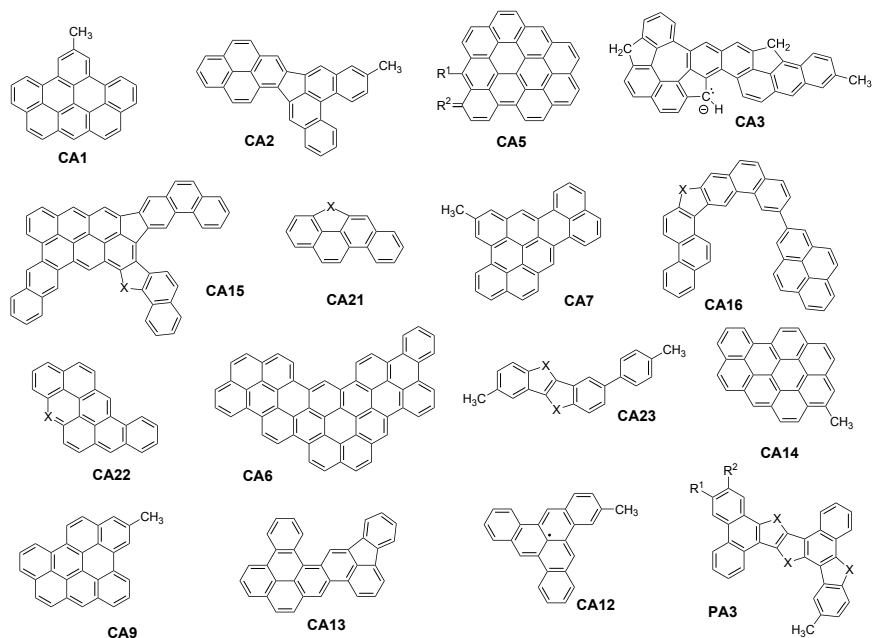


Figure 8.7.: **Proposed chemical structures.** The proposed structures are based on AFM measurements and STM orbitals images. *X* denotes unknown moieties within the carbon framework (likely CH, CH₂, N, NH, O or S) and *R* indicates unknown side-groups.

observed two identical specimens. Typically, CAs have a single central PAH core containing about 4-20 rings, which are predominantly fused in a peri-condensed manner (e.g., Fig. 8.6a), but also cata-condensed fragments can be observed (e.g., Fig. 8.6g). The molecules tend to be slightly bigger than expected by considering mass limits and presuming one PAH per molecule¹⁹⁷. Nevertheless, in most mass spectrometry (MS) studies of asphaltenes, an unidentified high-mass tail has been reported²¹². According to our measurements, we believe that these heavier molecules share the same molecular architectures as their lighter counterparts.

By analyzing each image in detail, one can identify additional interesting structural patterns. For example a 9-membered macrocycle in Fig. 8.6v, a molecule with four PAH islands in Fig. 8.6t, and a molecule with exceptionally large side-groups in Fig. 8.6d, indicating incomplete cracking. Another remarkable specimen that was unambiguously identified is **CA6**

8. Chemical structure identification

(Fig. 8.6b), a 18-ring nanographene. This suggests the exciting possibility of using asphaltenes to explore nanographenes with novel geometries²¹³. In Fig. 8.7 we present the proposed chemical structures for certain molecules that could be fully or partially identified.

CA molecules can be used to study PAHs of asphaltenes in general and are well suited for constant-height AFM imaging, because they are typically planar and have only few side-chains. However, PAs are much more important from an economic standpoint and are known to have more and longer side-chains attached to the PAH core, which complicates both measurement and analysis. The PA investigated here is from virgin crude oil (which typically stems from aquatic organisms) and did not undergo additional physico-chemical treatment (such as hydrogenation and cracking as CA). In Fig. 8.8a,b AFM images of **PA1** are shown. This molecule has a large PAH core with two side-chains attached. We observe repulsive contrast on the side-chains already at a tip height that is 2 Å larger than the tip height needed to atomically resolve the PAH. This is indicative of the side-chains being less closely adsorbed on the surface compared to the PAH¹²⁶. The side-chains sometimes also undergo structural changes when being scanned in STM or AFM mode. As shown in Fig. 8.8a, they often appear as zigzag-like patterns, associated with alkanes. In STM orbital images, these side-chains do not contribute (see Fig. 8.8e,f). A similar example is **PA2** (Fig. 8.8g-i), which has a side-chain of about 20 Å in length. Also here, the PAH core alone composes the orbital, which allow conclusions on its structure. Imaging orbitals is particularly important for PA as the peripheral alkanes can make interpretation of AFM images of PA difficult. Typically, PAs also exhibit more substituents and five-membered rings than CAs do. Exemplary, **PA3** shown in Fig. 8.8j-l, features three such pentagonal rings.

In summary, we find that asphaltene molecules consist of a central aromatic core with peripheral alkane chains. In some cases, this central core is divided into several distinct PAHs connected by a single bond, which proves the presence of ‘archipelago’-type molecules. Nevertheless, a single aromatic core with peripheral alkanes is the dominant asphaltene molecular architecture, proving the main aspects proposed by the Yen–Mullins model²⁰⁵. The diverse PAH architecture (number and type of rings and overall shape) of CAs and PAs is similar, despite significant differences in their formation and post-processing. The main difference is the presence of longer side-groups in PA. Additionally, PA contain more substituted

8.3. Asphaltenes: Unraveling the chemical structure of a complex mixture

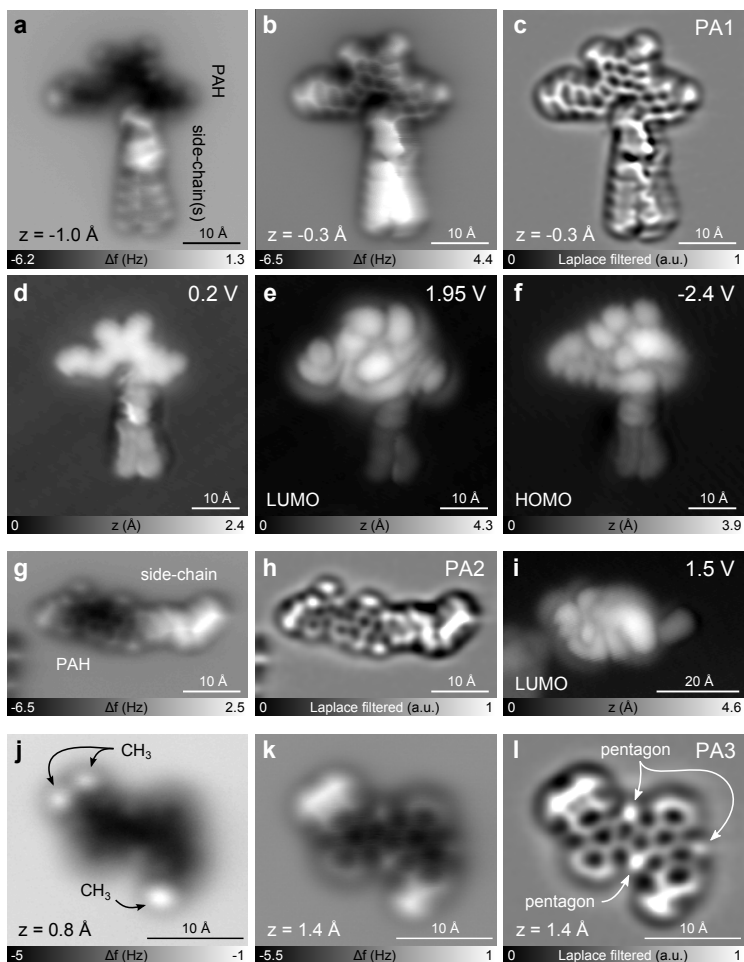


Figure 8.8: **Petroleum asphaltenes PA1-PA3.** **a,b** AFM images of **PA1** on NaCl(2ML)/Cu(111) at different set-points z from ($I = 1$ pA, $V = 0.2$ V). **c** Laplace-filtered image of **b**. **d-f** STM images ($I = 1$ pA) of **PA1** recorded at 0.2 V, 1.95 V and -2.4 V, respectively. **g,h** AFM image of **PA2** on NaCl(2ML)/Cu(111) (**g**) and its Laplace-filtered version (**h**). **i** STM orbital image ($I = 0.6$ pA) of **PA2** corresponding to the LUMO resonance. On the left side of **g-i** there is a small patch of third-layer NaCl. **j,k** AFM images of **PA3** on NaCl(2ML)/Cu(111) at different set-points z from ($I = 1.8$ pA, $V = 0.2$ V). **l** Laplace-filtered image of **k**.

8. Chemical structure identification

rings. Both, CA and PA molecules are larger than expected from previous studies^{197,206,212}. This study shows that complex, polydisperse molecule mixtures can be analyzed by AFM and STM on a single-molecule basis with atomic-resolution. We could resolve uncertainties about the mean molecular structures and also provide the first direct measurement of the tremendous range of molecular structures in asphaltenes.

More generally, this technique might be useful to study the traceability of a sample, that is to characterize and identify the origin of the raw material and chemical/physical processes involved in the formation of the compounds. Obviously, there is also a huge potential to analyze related carbon-based aromatic mixtures, such as vacuum residues, heavy fractions, tar, pitch, bitumen etc. The demonstrated structure elucidation of mixtures by scanning probe microscopy constitutes a paradigm shift for the development of new molecules: Many different molecules in a mixture can be screened by high-resolution scanning probe microscopy in a single preparation without going through a lengthy chemical synthesis, purification and characterization for each one of them beforehand. Important properties of individual molecules, i.e., electron affinity level, ionization potential, shape and extent of the molecular frontier orbitals are investigated by STM for hundreds of different molecules found in a mixture and their molecular structures are assigned *in situ* by AFM.

Conclusion structure identification by AFM. In this chapter we demonstrated AFM-based structure identification of molecules from a chemical reaction, a purified natural substance and a highly complex natural mixture. A strength of AFM is that single molecules can be addressed. This renders possible to investigate also samples that are mixtures of molecules and to identify their structures individually. Therefore in reactions that yield several products, these can be studied one-by-one and even very rare side products of chemical synthesis that cannot be assigned in the NMR spectra can be detected by AFM¹⁴⁸. Therefore, this technique does also not demand the same stringent purity requirements as spectroscopic or diffraction based methods. Moreover, as we will see in section 9.1, AFM has been used to identify reaction products and reactive intermediates formed by atomic manipulation. Importantly, STM orbital imaging and KPFM measurements naturally complement the structural information obtained by AFM. This complementary information might be used to verify or amend structure proposals from AFM.

CHAPTER 9

Atomic manipulation on insulators

The progress in manipulation techniques has not only extended the application of SPM but also opened-up the possibility to directly engineer matter at the atomic scale. For example the construction of many different artificial nanostructures^{5,7,214} has been demonstrated that allows the study of quantum phenomena locally. Inducing chemical reactions on the single molecule level^{10,12,156} is another fascinating application of atomic manipulation.

In the previous chapters vertical atomic manipulation has been used to pick-up atoms or molecules for tip functionalization. It turned out that the NaCl layer simplifies the pick-up of adsorbates due to their lower binding energy as compared to adsorption on metals. However, especially lateral manipulation is in general more difficult on insulators than on metals or semiconductors because of the unfavorable ratio between diffusion barrier and desorption energy⁹³.

In the following atomic manipulation is used to trigger chemical reactions of single molecules, to create defect structures, to manipulate the charge state of adatoms, to mechanically actuate an atomic switch and to implant individual metal atoms in an insulator. All of these manipulations were performed on an insulating film.

9.1. Single-molecule chemistry

In this section we take advantage of the possibility to study reactive intermediates using AFM at low temperatures and on thin insulating films. As will be shown, reactive intermediates can be created using atomic manipulation and can be stably imaged and studied under these conditions.

9. Atomic manipulation on insulators

9.1.1. Aryne: Catching the elusive intermediate

The capability to image and manipulate molecules on the atomic scale makes STM a well-suited tool to study on-surface chemistry on the molecular scale^{10,12,156}. Naturally, the ability of AFM to resolve chemical structures using functionalized tips³⁸ was an additional boost in this direction^{27,138,139,215}.

Reactive intermediates are involved in most chemical transformations. However, their characterization is a great challenge because of their short lifetime and high reactivity. Arynes are prominent reactive intermediates, formally derived from arenes by removal of two hydrogen atoms from adjacent carbon atoms. Their rich chemistry enables widespread use in synthetic chemistry, as they are privileged building blocks for the construction of polycyclic compounds containing aromatic rings. Here, we demonstrate generation and characterization of individual polycyclic aryne molecules on an ultra-thin insulating film by means of low-temperature STM and AFM. In addition, our results provide important insights into the chemistry of these elusive intermediates and its potential application in the field of on-surface synthesis.

The history of the short-lived aryne species dates back to 1902^{216,217}, although conclusive experimental evidence of the intermediacy of benzyne – C_6H_4 , the parent member of the aryne family – in a chemical transformation was reported only in the 50's by Roberts²¹⁸. Arynes soon proved to be useful synthetic tools as suitable methods for their generation in diverse reaction environments became available²¹⁹. Despite this broad range of practical applications, their structural characterization has been the subject of debate and remains a challenge. Microwave²²⁰ and IR²²¹ spectroscopic studies on benzyne – and several substituted and annulated derivatives – either in the gas phase or isolated in cryogenic matrices, support an electronic structure best described by a resonant form with a triple bond between two adjacent carbon atoms. However, the solution 1H and ^{13}C NMR spectra of benzyne, generated inside a hemicarcerand molecular container, are in agreement with a cumulene structure²²², whereas theoretical calculations suggest a structure of more acetylenic than cumulenic character²²³.

In section 6.1 we have already discussed how individual aryne molecules can be generated by a dissociation process from a precursor molecule

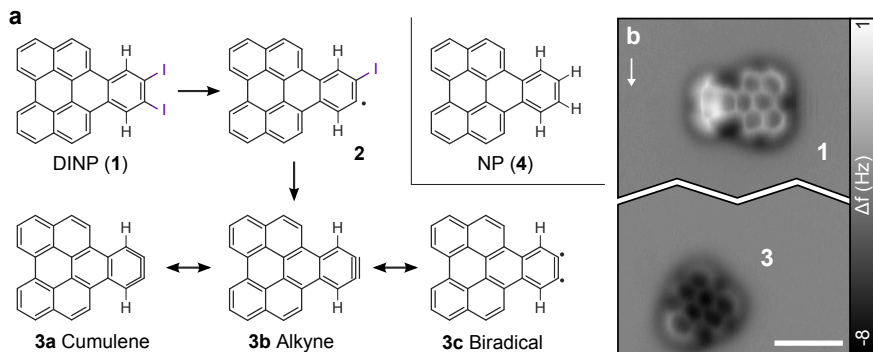


Figure 9.1.: **Molecular structures.** **a** Starting from DINP (1), iodine dissociation generates aryne 3. Dehalogenation may either occur directly from 1 to 3 or sequentially via intermediate 2. 3a-c are the three possible resonance structures of this aryne. NP (4) is the hydrogenated analogue of aryne 3 and investigated for comparison. **b** Direct comparison of a DINP (1) and an aryne molecule (3) in a single scan. Scan area in-between the molecules is omitted. The fast scan direction is indicated by the white arrow. Scale bar: 10 Å.

on NaCl(2ML)/Cu(111). From our experiments we see that dehalogenation occurs for voltages $V \gtrsim 1.6$ V. This threshold corresponds to resonant tunneling, suggesting that energy from vibronic excitations¹⁷ is dissipated to cleave the C-I bonds. Fig. 9.1a presents the molecular structures involved in the generation process. The starting material is 10,11-diiodonaphtho[1,2,3,4-*ghi*]perylene (DINP, 1), a molecule with two iodine atoms at the outer benzene ring. Tip-induced iodine dissociation may occur either in a two-step process via radical 2 or directly. The final product after dehalogenation, 10,11-didehydronaphtho[1,2,3,4-*ghi*]perylene (or naphthoperylyne, and simply denoted as aryne below), can be depicted using three resonance structures (3a-c). We have deliberately chosen large polycyclic DINP molecules to render bond-order analysis possible¹¹². In addition, structure 4 depicts naphtho[1,2,3,4-*ghi*]perylene (NP), which is the pure aromatic hydrocarbon.

The chemical structure of the compounds involved in the on-surface generation were investigated by means of CO-tip AFM imaging. In AFM images of DINP molecules (see Fig. 6.2a and Fig. 9.1b), the bonded I atoms show up as bright, elongated features corresponding to strong repulsive force contributions. After dissociation, these iodine atoms are typically found next to the molecule (see Fig. 6.2b,c), but not covalently bonded

9. Atomic manipulation on insulators

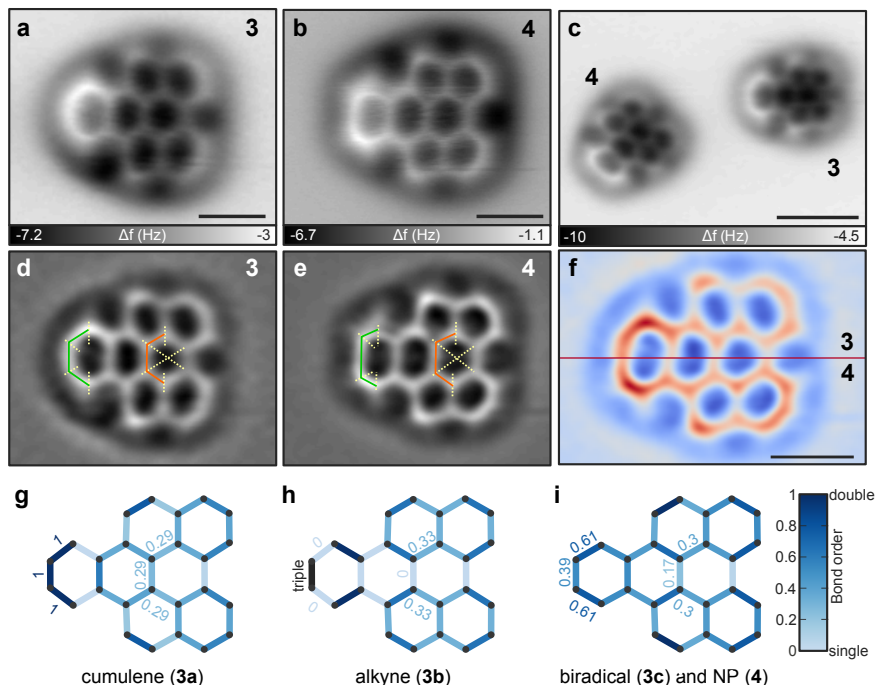


Figure 9.2.: **Structure and bond-length evaluation of aryne and NP molecules.** **a,b** AFM imaging of individual aryne (**3**, $z = -1.1$ Å) and NP molecules (**4**, $z = -0.8$ Å), respectively. **c** AFM image of an aryne (**3**) and an NP molecule (**4**) close to each other ($z = -1$ Å). **d,e** Laplace-filtered images of **a,b**. Solid and dashed lines are drawn to highlight differences in the apparent bond lengths. **f** Bisected image showing **d** (**3**) in the upper half and **e** (**4**) in the lower half to emphasize the differences. **g-i** Color-coded Pauling bond orders for Kekulé depictions **3a**, **3b** or **3c**, respectively. Note that **i** is also valid for NP molecules (**4**). z offsets are given with respect to ($I = 2$ pA, $V = 0.2$ V). Scale bars: 5 Å.

anymore.

Fig. 9.1b shows an AFM image of DINP and aryne in vicinity of each other. It is not surprising that these molecules appear quite differently in AFM images. For example, the differences in brightness of the two molecules in Fig. 9.1b result from a different adsorption height¹²⁶, which was about 0.2 Å smaller for aryne than for DINP. However, the question arises whether the final product corresponds to aryne. To this end, we also performed AFM imaging of closely related NP molecules (**4**) for comparison

with an aryne. AFM images of individual aryne and NP molecules are presented in Fig. 9.2a,b, respectively. The most striking differences arise for the on-axis rings at the aryne-related end and the adjacent ring. The end is characteristically curved for arynes, whereas for NP sharp kinks at the apparent carbon positions are visible. Moreover, additional features are resolved at the positions of C-H bonds and can best be seen in the Laplace-filtered images (Fig. 9.2d,e). The adjacent ring appears larger for NP than for aryne.

Beyond that, a closer look reveals more subtle differences referring to the different Kekulé depictions of arynes. The relative contributions of the resonance structures of arynes are unclear, ever since their first demonstration²²⁴. We thoroughly investigated the data in Fig. 9.2a-f in terms of differences in bond orders¹¹² using the empirical scheme proposed by Pauling¹¹³ as a qualitative and easy-to-obtain quantity¹¹⁴. The Pauling bond orders for structures 3a-c and 4 are depicted in Fig. 9.2g-i (greater bond orders correspond to shorter bonds). Note that the Pauling bond orders of NP (4) are identical to the biradical representation (3c, Fig. 9.2i) of aryne. In our analysis, we will discuss in particular the bonds highlighted in Fig. 9.2d,e. The bonds in the central part of the molecule, highlighted in orange, are ideally suited for a bond-order analysis¹¹². In the case of NP, the Pauling bond orders are 0.17 for the bond perpendicular to the symmetry axis, and 0.3 for the two adjacent ones. In agreement with that, the former bond is measured clearly longer than the latter ones in our data for NP (Fig. 9.2e). It is expected that alkyne (3b) contributions should lead to even more pronounced differences. On the contrary, the relative difference is much less pronounced in the case of aryne (Fig. 9.2d), indicating strong contributions from the cumulene resonance structure (3a). This observation is also in good agreement with the appearance of the three outermost bonds highlighted in green. In aryne these bonds appear very similar as expected for the cumulene (3a) representation, which shows identical bond orders for these three bonds. The biradical (3c) would be expected to show a clearly longer outermost C-C bond, as observed for NP. Finally, the triple bond of the alkyne (3b) would be expected to appear brighter than all other bonds in the molecule and elongated perpendicular to the bond direction^{134,138,215}.

Additionally, complimentary DFT calculations were performed by Nikolaj Moll (see Supplementary Information in Ref. 225) of free aryne and NP molecules. The resolution of the simulated AFM images based on the

9. Atomic manipulation on insulators

calculated molecules is too low (due to the high computational cost of the calculations) to resolve the subtle differences in the inner part observed in the experiment. However, the outer parts, for which the distortions are highest, are reproduced very well by the simulated AFM images and the theory reveals how the apparent atom positions are related to the real positions of the atoms. Due to the tilting of the CO tip^{112,125,134,140,226} all the atoms and bonds at the periphery of the molecule appear displaced towards the outside of the molecule. The displacement of the outermost bond on the symmetry axis is more pronounced for the aryne than for the NP molecule (Fig. 9.2a-f) resulting in an enlargement of the outer ring of aryne in agreement with the experiment. The length of the outermost carbon-carbon bond is calculated to be 1.26 Å for aryne. This is between a double bond and a triple bond, which have been calculated to be 1.33 Å and 1.21 Å for ethylene (ethene) and acetylene (ethyne) molecules, respectively. We conclude from our AFM data that the cumulene (**3a**) resonance structure plays the dominant role for this aryne. The remaining contributions are rather from the alkyne (**3b**) than from the biradical (**3c**) representation, as suggested by DFT calculations.

The stability observed for aryne molecules during imaging with different tip terminations (Cu, CO, and I) may raise doubts regarding their chemical reactivity, and thus, their arynic nature. To this end, we have investigated two possible on-surface reaction schemes. First, we discuss the situation depicted in Fig. 9.3a, in which the I atoms are lying close to the aryne molecule. After a manipulation event changing the adsorption position of one of the I atoms, both I are close to those of bonded atoms of DINP (Fig. 9.3b). Finally, Fig. 9.3c shows that a subsequent manipulation event has initiated bond formation and thereby regenerated DINP. Orbital imaging performed before and after the dissociation-and-healing process unambiguously proves that the molecule is indeed an intact DINP. This data provides a strong evidence that the activity of aryne is preserved on the surface.

In a different experiment, we performed dehalogenation of DINP molecules adsorbed on the bare Cu(111) surface (see Fig. 9.3d). The result of a voltage pulse of $V \approx 2$ V is shown in Fig. 9.3e. On the bare Cu surface, the dissociated I atoms result in a much weaker AFM contrast than on NaCl; but more importantly, the resulting molecular structure is very different compared to the adsorption on the NaCl surface, namely, only two out of three on-axis aromatic rings can readily be resolved on Cu(111).

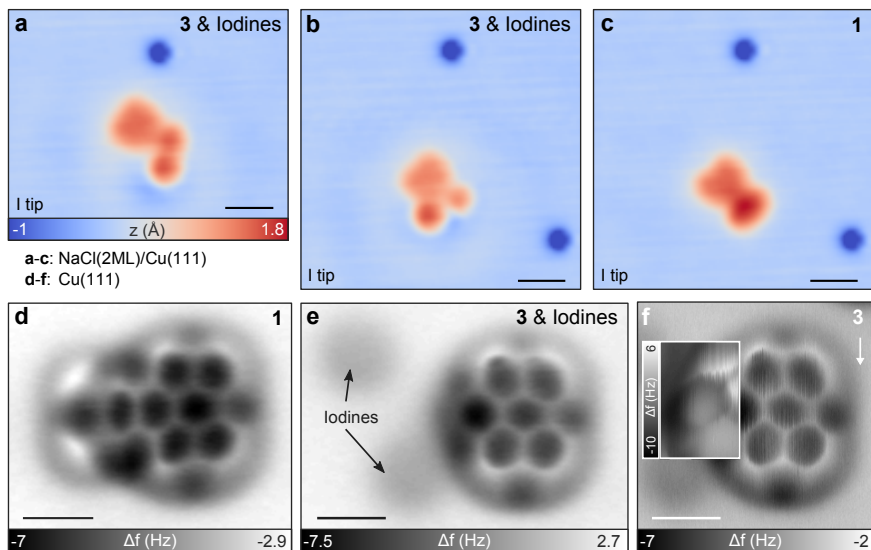


Figure 9.3.: **On-surface chemistry of an aryne.** **a-c** Sequence of STM images ($I = 2$ pA, $V = 0.2$ V) on NaCl(2ML)/Cu(111) proves reversibility of dehalogenation. A voltage pulse after scan **b** results in an intact DINP molecule. **d,e**, AFM images before ($z = 1.3$ Å) and after ($z = 1.2$ Å) dehalogenation of DINP on Cu(111), respectively. **f** Adjusted constant-height AFM image of the same molecule with $z = 2.7$ Å in the highlighted region and $z = 1.3$ Å elsewhere. An adjusted gray scale is used for this region, as indicated. The fast scan direction is indicated by the white arrow (otherwise it is horizontal). z offsets are given with respect to ($I = 2$ pA, $V = 0.2$ V). Scale bars: 10 Å in **a-c** and 5 Å in **d-f**.

However, adjusted constant-height AFM images¹²⁶, presented in Fig. 9.3f, reveal that the outermost ring is in fact present, but bent towards the surface, that is, the aryne immediately forms strong covalent bonds to the Cu surface, in agreement with previous studies on dehydrogenated phthalocyanine molecules¹⁵⁶ and benzyne adsorbed on Ir(100)²²⁷.

In summary, we have presented direct imaging of the chemical structure of individual arynes for the first time. Our experiments provide insight into a class of transient species that, in general, remain obscured because of their short lifetimes. The fact that the arynes' chemical reactivity is preserved even at cryogenic temperatures is promising for novel on-surface reaction schemes, for example, for the preparation of graphene-based materials. In general, the approach presented here might also be applicable for other

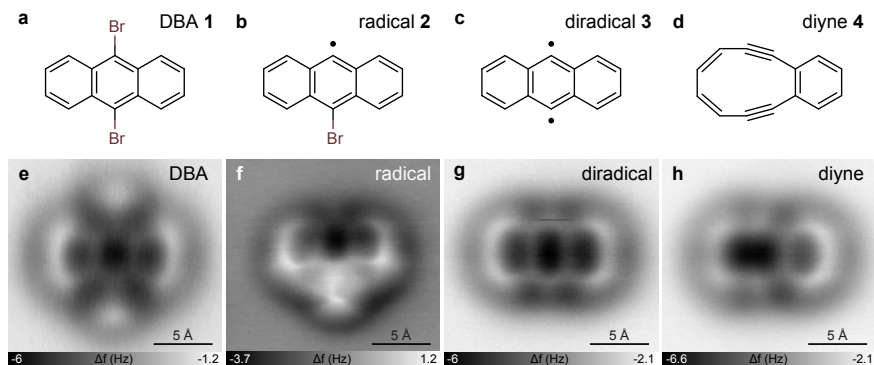


Figure 9.4.: **Starting material, reaction intermediates and products.** **a-d** Chemical structures of the reaction products formed by successive STM-induced debromination of 9,10-dibromoanthracene (DBA) and subsequent retro-Bergman cyclization: DBA, 9-dehydro-10-bromoanthracene (radical), 9,10-didehydroanthracene (diradical) and 3,4-benzocyclodeca-3,7,9-triene-1,5-diyne (diyne). **e-h** AFM images of the molecules **a-d**, respectively, on NaCl(2ML)/Cu(111) using a CO tip.

short-lived reaction intermediates. Furthermore, we have shown that even extremely small changes, like two missing hydrogen atoms in the chemical structure, can be resolved with AFM imaging. Analysis of bond-order-related contrast showed significant differences for the molecules investigated and indicated the dominant contribution of the cumulene representation for the aryne generated under these conditions.

9.1.2. Dibromoanthracene (DBA): Retro-Bergman cyclization

In the previous section we discussed a single-molecule reaction based on dehalogenating DINP. We could verify the creation of the highly reactive aryne molecule and prove its persistent reactivity also at low temperatures. In this section, we follow a similar approach: We dissociate both Br atoms from a dibromoanthracene (DBA) molecule (cf. sections 6.1 and 6.2) to form a diradical. Subsequently a ring-opening retro-Bergman cyclization could be initiated, all by means of atomic manipulation. The conversion between diradical and diyne is reversible, realizing a tri-state single molecular switch based on forward and backward Bergman reaction, i.e., the creation and cleavage of covalent carbon-carbon bonds within a molecule, triggered by atomic manipulation.

In recent years, on-surface synthesis has attracted an enormous interest

to prepare diverse nanostructures following bottom-up approaches^{228–230}. Among the reactions employed for this purpose, the Ullmann coupling of halogenated aromatic compounds has emerged as the most successful on-surface chemical transformation^{10,15,213,231}. In most cases, this reaction is thought to proceed via dehalogenation of aryl halides followed by C-C coupling of the resulting aryl radicals. It should also be mentioned that thermal-induced Bergman cyclization of enedynes, followed by radical polymerization, has been recently proposed to explain the synthesis of polyphenylene chains on Cu(110)²³². Moreover, a Bergman reaction has been also proposed to initiate the cyclization of oligo-(phenylene-1,2-ethynylenes) on Ag(100)¹³⁸. In this context, while studying the on-surface behaviour of 9,10-didehydroanthracene (diradical; **3**), generated from DBA (**1**), we observed the formation of cyclic diyne **4** by means of a retro-Bergman cyclization reaction²³³.

To confirm the structure of the precursor (Fig. 9.4a), and identify intermediates (Fig. 9.4b,c) and the reaction product (Fig. 9.4d) we employed AFM imaging with CO-functionalized tips. As visible in Fig. 9.4e the Br atoms of DBA appear as bright lobes of increased frequency shift. The C–Br bonds could be dissociated on NaCl(2ML)/Cu(111) by placing the tip above the molecule and applying a voltage pulse. The voltage threshold to dissociate the first Br atom, which forms 9-dehydro-10-bromoanthracene (radical **2**) is about 1.6 V and often the dissociation is accompanied by a lateral displacement of the Br atom and the molecule (cf. Fig. 6.1c,d). In the AFM image of the bromoanthryl radical, shown in Fig. 9.4f, the bright feature corresponding to the Br atom can only be seen on one side of the molecule. The contrast of the molecule indicates that its adsorption is non-planar^{125,126}. The gradual brightness increase in Δf from the debrominated side towards the brominated one is indicative of a smaller adsorption height at the side of the dangling bond. Frequently, the radical was found in another, more planar geometry, with a distinctively different contrast in STM and AFM (see Fig. 9.5c,f). The planar and non-planar adsorption geometry could also be inter-converted. However, the planar geometry was less stable to image.

The second C–Br bond is dissociated to form the diradical **3** by applying a voltage pulse of about 3.3 V, thereby the tip was retracted by several Ångströms to limit the current to tens of picoamperes. Again, the debromination process was often accompanied by a displacement of the organic fragment and the Br atom. The AFM image of the diradical is

9. Atomic manipulation on insulators

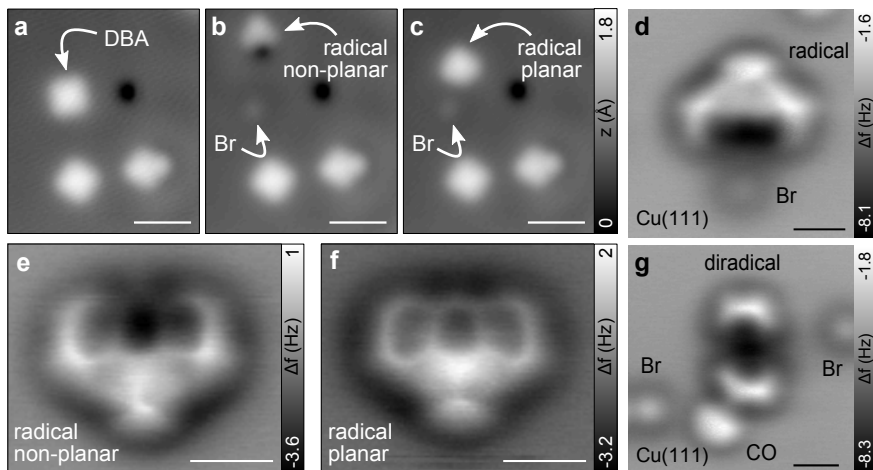


Figure 9.5.: Radical conformations on NaCl(2ML)/Cu(111) and debromination on Cu(111). **a** STM image of two DBA molecules and a (planar) radical with a close-by Br (bottom right). **b** After a voltage pulse of 1.6 V, a DBA was dissociated to a radical and a Br atom. In this case, the radical appears with a black depression where the Br is missing (non-planar adsorption). **c** The conformation of the radical can be switched from non-planar to planar, by a voltage pulse of 0.6 V. **d** AFM image of the radical on Cu(111). **e/f** CO tip AFM image of radical in the non-planar/planar conformation. **g** AFM image of the diradical on Cu(111). Scale bars: 20 Å in **a-c**, 5 Å in **d-g**.

shown in Fig. 9.4g. As demonstrated for arynes, the NaCl film facilitates the stabilization of reactive intermediates, radicals and diradicals²²⁵. While the consecutive debromination of DBA on Cu(111) was possible as well, the debrominated sites strongly bind to the substrate in this case (see Fig. 9.5d,g). From the image of the diradical alone this molecule could easily be mistaken for the anticipated image of anthracene (compare the positions of H and dangling bonds in Fig. 9.4g and see also images of pentacene for comparison³⁸). However, the generation of diyne from the molecule shown in Fig. 9.4g (as described below) proves that the latter was actually the diradical. A voltage pulse of 1.7 V was applied with the tip above the molecule shown in Fig. 9.4g. AFM imaging of the resulting product, shown in Fig. 9.4h, revealed a molecule apparently consisting of a fused 6- and a 10-membered ring, suggesting the formation of diyne **4**. Note that diyne was often created directly from the radical without observing diradical **3** in the first place.

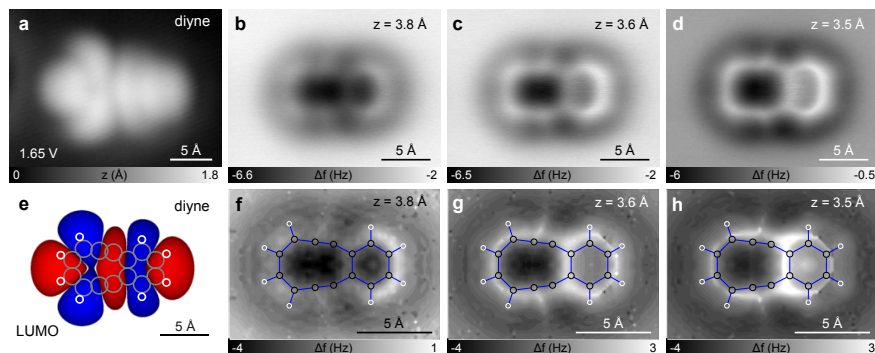


Figure 9.6.: **Diyne identification.** **a** STM topography ($I = 2$ pA, $V = 1.65$ V) of diyne. **b-d** AFM images of diyne on NaCl(2ML)/Cu(111) at different heights z . **e** Calculated LUMO orbital isosurface at $\pm 10^{-4} e$ of diyne with the molecular structure overlaid as a guide to the eye. **f-h** Calculated Δf maps of diyne at different tip–molecule distances using a relaxed CO tip.

To prove that we indeed created the cyclic diyne, we employed a combination of STM for orbital imaging²⁶ (Fig. 9.6a), CO tip AFM images at different tip heights (Fig. 9.6b–d) and compared the experiments with DFT calculations (Fig. 9.6e–h). Like in section 7.1, the tip–molecule distance is estimated by setting the height of the Δf minimum at the center of the outer carbon ring to $z = 3.9$ Å. With orbital imaging, only the LUMO resonance was in the experimentally accessible voltage range without switching or displacing the molecule. Though, switching and associated displacements observed at elevated voltages (> 1.65 V) restricted us to the measurement of the LUMO resonance onset, corresponding to a higher electron density isosurface. The relative orbital intensities and the location of the nodal planes are in good agreement with the calculated LUMO of diyne (Fig. 9.6e), corroborating our assignment.

Moreover, the experimental and calculated AFM images are in good agreement. Particularly, the 10-membered carbon ring of the diyne exhibits features that relate to different bond orders¹¹² and that lead to a characteristic fingerprint of this moiety. For example the triple bonds appear with a distinctive elongation perpendicular to the bond direction as previously found for alkynes imaged by CO tips^{134,138}.

On the metal, no diyne creation was observed, emphasizing the importance of the insulating layer to facilitate the reaction. The direct visualization of

9. Atomic manipulation on insulators

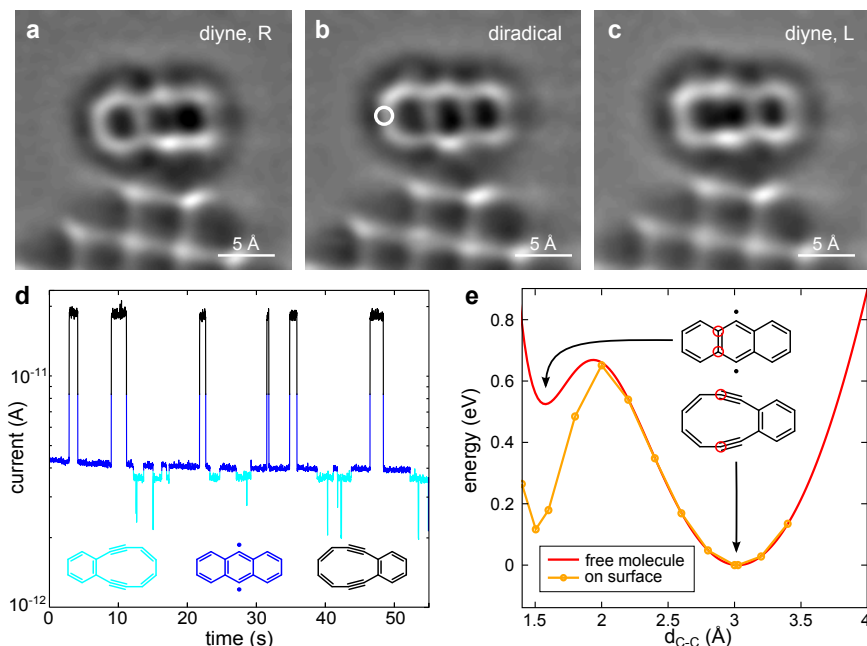


Figure 9.7.: **Reversible Bergman cyclization.** **a-c** Laplace-filtered AFM images of diene, R (**a**), diradical (**b**) and diene, L (**c**) on NaCl(2ML)/Cu(111). **d** Current trace during a voltage pulse of $V = 1.64$ V at the position indicated by the white circle in **b**. The different current levels correspond to the molecular structures of the same color shown in the inset. **e** Calculated energy of the Bergman cyclization, using the carbon–carbon distance d_{C-C} of the carbons indicated by the red circles as a reaction coordinate.

the molecular structures by AFM and the good agreement of theoretical calculations with AFM and STM images proves the creation of diene and thus the successful execution of a retro-Bergman cyclization using atomic manipulation.

Next, we study the Bergman cyclization reaction in more detail and prove its reversibility and the inter-conversion between the two possible diene topomers. Which topomer is created depends on which of the two C–C bonds that are shared by fused benzene rings is cleaved. Problematically, manipulation events are usually associated with the displacement of the molecule, which hampers the exclusion of possible rotations. To avoid such displacements, we stabilized the diradical at a step edge of a third-layer

NaCl island. To this end, we first manipulated the molecule by inelastic excitation⁹³ (involving several conversions between diradical and diyne) to bring the molecule to a NaCl step edge shown in Fig. 9.7. With the molecule anchored at the third-layer step, the voltage for the Bergman cyclization could be applied without lateral displacement of the molecule. In the current trace recorded during such switching at 1.64 V (Fig. 9.7d) we observe switching between three different current states. By reducing the voltage after switching of the molecule and taking an AFM image, we can relate the three different current plateaus in Fig. 9.7d to the three different molecular structures shown in Fig. 9.7a-c. Fig. 9.7a shows diyne, with the 10-membered ring on the right hand side (diyne, **4R**) and corresponds to the low-current state in Fig. 9.7d. Fig. 9.7b shows the diradical corresponding to the medium-current state and Fig. 9.7c shows diyne, **4L**, which corresponds to the high-current state in Fig. 9.7d. Note that the lateral position where we apply the voltage and measure the current determines the value of the current plateaus measured above the different isomers. As indicated by the white circle in Fig. 9.7b we chose an off-centered position in order to distinguish the diyne topomers, **4L** from diyne, **4R**.

First of all, these observations demonstrate that the Bergman reaction can be performed reversibly in this system, that is the two C-C bonds shared by two fused benzene rings within the molecule can be created and cleaved again. Note that we cannot direct in which state the molecule will switch, but we can stop the switching at any of the three molecular states at will. When reducing the voltage below the reaction threshold all three molecular structures remain stable and no switching was observed enabling the recording of AFM images at low voltage. Note that the switching yield per electron depends not only on the molecular electronic structure, but also on the environment, in particular on the adsorption at the step edge, which breaks the symmetry of the molecule.

We calculated the potential energy surface of the Bergman cyclization of the free molecule and the molecule adsorbed on NaCl/Cu(111) by DFT using the carbon-carbon distance of the bond that is formed during the Bergman reaction as the reaction coordinate (see Fig. 9.7e). For both, the free molecule and the molecule adsorbed on the surface, the diradical and the diyne form two (meta)stable conformations. In vacuum, diyne has a lower absolute energy compared to the diradical by 0.52 eV, with a barrier of 0.67 eV (according to our calculations and in good agreement

9. Atomic manipulation on insulators

with theory²³⁴). Our calculations show that upon adsorption, the diradical energy is significantly lowered but the diyne structure is still favored by about 0.12 eV. This is consistent with the observations made by AFM and STM: Both, the diradical and diyne are observed but the latter prevailed after random switching. During AFM measurements at close distance we also observed spontaneous switching from the diradical to diyne but never the opposite.

We could demonstrate the sequential derivation of diyne by three single-molecule reactions starting from DBA by means of atomic manipulation. The reaction intermediates and product could be identified and characterized by atomic resolution AFM measurements and STM orbital imaging that are compared with DFT calculations. The last reaction represents a retro-Bergman cyclization that could be triggered reversibly, and involves two diyne topomers, constituting a tri-state molecular switch.

9.2. Cl vacancy chains: Effect of electron–phonon interaction on the formation of one-dimensional electronic states

One-dimensional nanostructures assembled from single metal atoms and molecules on surfaces are of great fundamental and technological interest as their electronic states exhibit a wealth of new quantum phenomena that might be exploited in future molecular electronics devices²³⁵. Some examples of such phenomena identified by STM and STS include metal-atom chains exhibiting ‘particle-in-box’ states²³⁶, bistable anti-ferromagnetism²⁵, Tomonaga–Luttinger liquid behavior²³⁷, and signs of Majorana spinors²³⁸. The formation of extended or band-like electronic states in metal-atom and molecular chains on surfaces has been widely studied experimentally^{215,239–242}, but potentially interesting effects of strong electron–phonon coupling on these states, such as, for instance, polaronic effects, have attracted much less attention. A notable exception is the observation of coherent electron–phonon states and the breakdown of the Born–Oppenheimer approximation in oligothiophene molecular chains²⁴³. In the electronically adiabatic regime, where the Franck–Condon principle is applicable, the electron–phonon coupling results in vibronic satellite structures. How these vibronic effects influence the delocalization of an injected electron in a one-dimensional nanostructure is an open question,

in particular when the electron–phonon coupling is so strong that these effects dominate.

Here we address this question by studying coupled electronic states localized at intentionally created Cl divacancies and vacancy chains in a NaCl bilayer on Cu(111). The Cl vacancies provide a quantum-well structure that could be created with atomic precision using the STM tip^{244,245}. The energies of the electronic states formed in these structures by injection of an electron from the tip of a STM and their spatial behavior on the atomic scale were resolved by STS. Our findings have ramifications for the formation of extended states from coupled adsorbate or confined defect states (such as in dopants²⁴⁶ or dangling bonds²⁴⁷) in semiconductors and ionic crystals. Hence, it could improve the understanding of polaronic effects in coupled quantum systems, such as quantum dots^{248–253}, charge-based qubits^{254,255} and quantum cellular automata²⁵⁶.

Coupled, individual Cl vacancies in a NaCl bilayer on a Cu(111) surface are ideal model systems to study the delocalization of electronic states in the presence of strong electron–phonon coupling. First, Cl monovacancies are atomically well-defined and highly symmetric defects. They feature two distinct electronic states: An unoccupied vacancy state (VS) that is strongly coupled to optical phonons in the film and a localized interface-state (LIS) with a negligible electron–phonon coupling^{26,257}. The electronic coupling between VSs or LISs of different vacancies can be tuned in a controlled way by the lateral spacing between vacancies with atomic precision²⁵⁸. Finally, Cl vacancies feature a much higher stability against inelastic excitations than adsorbates²⁵⁹. Cl vacancies could even be filled with other atoms (see section 9.3.3). Hence, they allow us to explore artificial coupled quantum systems with great control.

In the spectroscopic measurements, the tunneling conductance dI/dV was recorded with conventional lock-in techniques with an ac bias amplitude of 25 mV at a frequency of 294 Hz. In the double-barrier tunneling junction geometry, the voltage drop across the insulating film will cause a voltage-dependent shift of the electronic levels. This tip-induced Stark shift is a few percent of the applied bias but depends only weakly on the tip distance. Therefore it is not considered here¹⁰⁹. As described in the previous section, the vacancies were created by controlled contact of the tip with the NaCl surface. AFM images with a CO tip^{38,80} were recorded to identify the vacancy location and exclude the generation of other close-by

9. Atomic manipulation on insulators

defects. In addition, the local contact potential difference on the polar film was measured with Kelvin probe force microscopy to ensure that the defects are indeed Cl vacancies⁹⁴.

In a previous study, single Cl vacancies in a NaCl bilayer on copper surfaces were characterized in detail (see Ref. 109). A Cl vacancy in the outermost layer of this supported NaCl bilayer is analogous to the widely studied and well-known color centers in bulk NaCl²⁶⁰ with one key difference: The localized VS is unoccupied because the electron can tunnel into unoccupied metal states. The unoccupied VS then gives rise to a positively charged vacancy and an attractive potential that is able to split off a LIS from the free-electron-like interface-state band of the NaCl/Cu(111)²⁶¹. This LIS was observed as a narrow resonance just below the bottom of the interface-state band in the dI/dV spectra, whereas the VS showed up as a broad negative ion resonance at a sample voltage of about 2.8 V in dI/dV . The negative ion resonance was found to have a large Gaussian broadening (full-width half maximum of $\sigma = 0.27$ V) because of the strong electron-phonon coupling of the electron in the VS to optical phonons in the NaCl bilayer. Despite this strong coupling, the associated relaxation energy of the electron in the VS is not large enough to prohibit tunneling into unoccupied metal states and to allow the formation of a stable occupied VS corresponding to a localized polaron. In contrast to the VS, the LIS was found to be dominated by lifetime broadening with a negligible phonon broadening in the dI/dV spectra, owing to the efficient screening of the electron-phonon interaction by the metal electrons.

First, vacancy pairs are created with different separations. Divacancies in the ninth-nearest-neighbor (9NN), 6NN, 5NN, 4NN, 3NN and 2NN^a configurations (see schematic in Fig. 9.8a) were created from two Cl vacancies close to each other but not in the vicinity of any other vacancies or defects. AFM images of the 5NN to 2NN divacancies and of a single vacancy are shown in Fig. 9.8b-f. With a CO tip, the vacancies can be recognized as a bright cross-like feature in AFM maps. The electronic structure of the divacancies were characterized by single dI/dV spectra or constant-height $dI/dV(x, V)$ maps along the line connecting the two vacancies. The VS resonances are shown in Fig. 9.8g-l and the LIS resonances in Fig. 9.8m-r, respectively. Note that all dI/dV data shown here are recorded using Cu-terminated tips. For divacancies with a separation larger than 10 Å

^a The 2NN divacancy was less stable than the divacancies with larger separations.

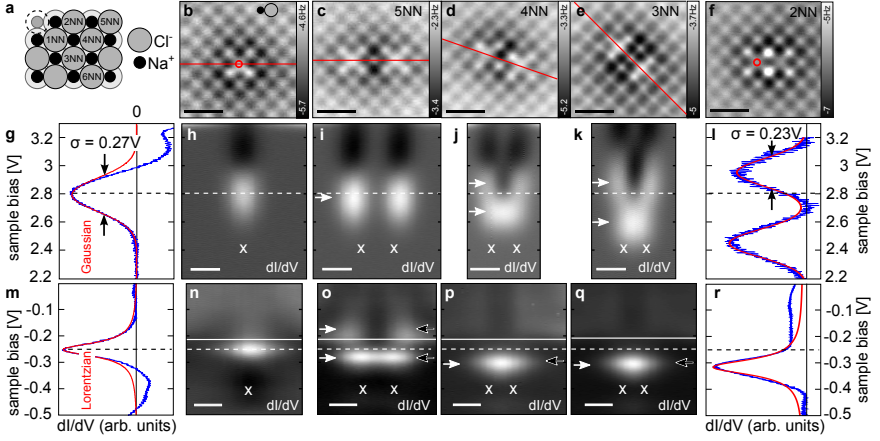


Figure 9.8.: **Vacancy states (VSs) and localized interface-states (LISs) of Cl divacancies.** **a** NaCl bilayer model with a Cl vacancy (dashed circle) and its nearest Cl neighbors indicated. **b-f** CO tip AFM images of a single Cl vacancy (**b**) and divacancies in the 5NN (**c**), 4NN (**d**), 3NN (**e**) and 2NN (**f**) configurations. **g, l** dI/dV spectrum of the monovacancy and 2NN divacancy VS peaks with a Gaussian fit in red, recorded at the red circles in **b, f**. **h-k** $dI/dV(x, V)$ maps along the red lines in **b-e** (same V scale as in **g**). Peaks in dI/dV are displayed as bright, whereas the darkest areas mark regions of negative differential conductance. The dashed line indicates the monovacancy VS peak position. **m, r** dI/dV spectrum of the LIS of a monovacancy and a 2NN divacancy with a Lorentzian fit in red, recorded at the red circles in **b, f**. **n-q** $dI/dV(x, V)$ maps along the red lines indicated in **b-e**, respectively (same V scale as in **m**). The dashed line indicates the monovacancy LIS peak position and the solid line the interface-state band onset. White crosses indicate the vacancy positions. White arrows mark the peak positions of the observed dI/dV resonances. Black arrows in **n-q** mark the peak positions of the calculated LDOS using the σ -wave multiple scattering model. Scale bars: 10 Å.

(i.e. larger than a 4NN divacancy), we observe a single VS resonance localized at each vacancy site separately with an energy similar to the one of the monovacancy. For smaller separations (4NN–2NN divacancies), however, two peaks with Gaussian line shapes appear around 2.8 V. The $dI/dV(x, V)$ maps show that the state at lower energy is localized between the vacancies (symmetric), whereas the state at higher energy has a nodal plane between them (antisymmetric), in analogy with the bonding and antibonding orbitals of the hydrogen molecule.

Similarly, the divacancy LISs were also observed to split into a symmetric and an antisymmetric state. However, for small vacancy separations, the latter state lies above the NaCl/Cu(111) interface band onset at

9. Atomic manipulation on insulators

$\varepsilon_B = -230\text{ mV}$ and overlaps with the band continuum. Hence, only the symmetric state is observed as a well-defined peak in dI/dV . The splitting of both the VSs and LISs was found to increase with decreasing inter-vacancy distance. The VSs do not split symmetrically about the monovacancy energy but their mean value is shifted towards lower energies. In addition, the VSs show a tendency to have a smaller level broadening with decreasing separation. Interestingly, a theoretical model derived in Ref. 262 reveals that the observed VS level separation is significantly enlarged by level repulsion compared to the pure electronic splitting, resulting from the strong electron-phonon coupling. Particularly, the enhanced splitting can be attributed to an avoided crossing between the potential energy surfaces of the symmetric and antisymmetric VS along the anti-correlated portion of the (uncorrelated) zero-point phonon motion.

To study the delocalization of VSs and LISs further, short 1D arrays of N vacancies, referred to in the following as vacancy chains, were created in the 5NN (apolar [001] NaCl direction) and the 3NN (polar [011] NaCl direction) configuration. They were also characterized by CO tip AFM images (Fig. 9.9a,c). For the 5NN chains, the LISs form 1D quantum-well states, observed as distinct resonances in dI/dV , with an increasing integer number of nodal planes with voltage (see Fig. 9.9b). Remarkably, also broader resonances are observed up to 200 – 300 mV above the interface-state band onset. These quasi-bound LISs have a lower height in dI/dV , owing to the increased lifetime broadening compared to the bound LISs. This originates from the additional decay channel into the interface-state band. Furthermore, the energy position of the ground-state LIS does not change significantly from the $N = 4$ to the $N = 6$ chain and seems to converge to about -0.33 V . The VS of the 5NN chains only show a single resonance peak at about 2.7 V, localized at each vacancy site because of the weak electronic coupling.

In contrast, the 3NN chains displayed in Fig. 9.9c are subject to significant interaction between the VSs and exhibit several resonances, as shown in Fig. 9.9d. The increasing number of nodal planes with voltage shows that the VSs are delocalized over the entire chains despite the strong electron-phonon coupling. Notably, the level broadening decreases for longer chains as displayed in Fig. 9.10a. This effect is a direct evidence of the dependence between the electron-phonon coupling and the enhanced delocalization for longer chains. It can be rationalized by the larger spatial extent of the eigenstates, which decreases their relaxation energy and

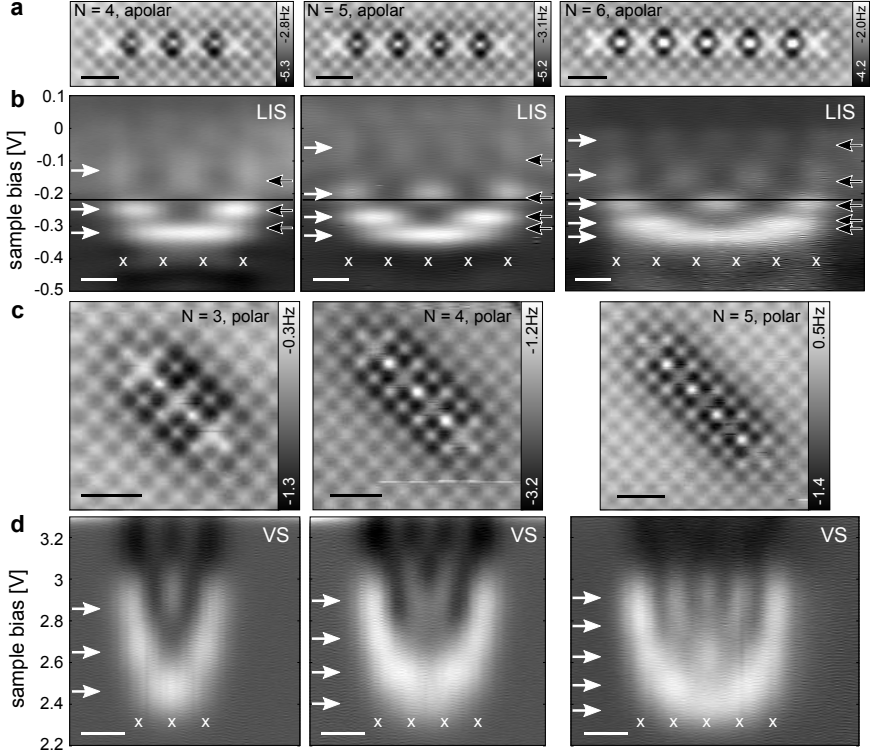


Figure 9.9.: **Vacancy states and localized interface-states of Cl vacancy chains.** **a** CO tip AFM images of Cl vacancy chains with $N = 4, 5, 6$ vacancies in the 5NN configuration (apolar direction). **b** Corresponding $dI/dV(x, V)$ maps of the LISs along the chains. The continuous line indicates the interface-state band onset. White arrows mark the peak positions of the observed dI/dV resonances, and black arrows mark the peak positions of the calculated LDOS. **c** CO tip AFM images of Cl vacancy chains with $N = 3, 4, 5$ vacancies in the 3NN configuration (polar direction). **d** Corresponding $dI/dV(x, V)$ maps of the VSs along the chains. White crosses mark the positions of the vacancies and the white arrows dI/dV peaks. Scale bars: 10 Å.

9. Atomic manipulation on insulators

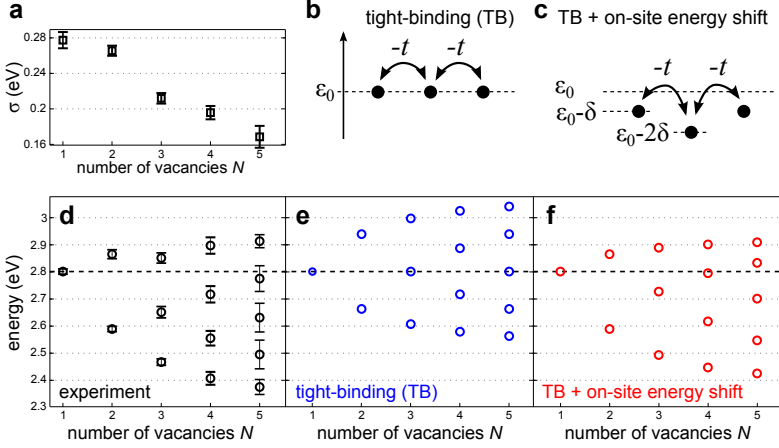


Figure 9.10.: **Tight-binding models.** **a** Experimental VS broadening σ as a function of the 3NN chain length. **b** Tight-binding (TB) model for a $N = 3$ chain. **c** TB model including the electrostatic on-site energy shift between nearest neighbors. **d** Experimental VS energies as a function of the 3NN chain length. **e** TB model energies obtained by fitting the on-site energy $\epsilon_0 = 2.8$ eV and hopping term $t = 0.14$ eV to the experimental mono- and divacancy VS energies shown in **d**. **f** TB model accounting for a shift of the on-site energy ($\delta = 0.07$ eV) due to the electrostatic interaction between nearest neighbors.

accordingly the effective electron–phonon coupling.

In the following, the VS energies of the 3NN chains are compared with the results from a simple tight-binding (TB) model. First, we assume that each vacancy in the chain has an on-site energy ϵ_0 and is coupled to its next neighbor(s) with a hopping term $-t$, as sketched in Fig. 9.10b. By adjusting the free fitting parameters ϵ_0 and t to the experimental mono- and divacancy VS energies, one can calculate the energy levels for different chain lengths as shown in Fig. 9.10e. In comparison with the experimental energy spectrum, depicted in Fig. 9.10d, the level spacings for each chain could be roughly reproduced, but the TB model does not capture the shift of the band center towards lower energies with increasing chain length (as already described for the divacancies). This shift can be explained by the electrostatic interaction between adjacent vacancies that deepens the potential at each vacancy and therefore lowers the on-site energy. To account for the energy shift we introduce the parameter δ , which is the on-site energy shift due to a neighboring vacancy (see Fig. 9.10c).

The resulting energy levels of this extended TB model are shown in Fig. 9.10f. The calculated energy spectrum now agrees very well with the experimentally observed VS levels of the chains.

The coupling between the LISs of Cl divacancies and chains were studied in a simple, multiple σ -wave (zero angular momentum in 2D) scattering model of the interface-state scattering from the positively charged vacancies, detailed in Ref. 262. The results from this model, as indicated in Fig. 9.8o-q, are able to fully capture the observed behavior of the coupled LISs. Furthermore, the obtained energies for the LISs of the vacancy chains are in excellent agreement with the experiments, as indicated in Fig. 9.9b.

In summary, from an AFM and STS study we find that the localized VSs and LISs at intentionally created Cl divacancies in a NaCl bilayer on Cu(111) form symmetric and antisymmetric states, in analogy to the bonding and antibonding orbitals of a hydrogen molecule. As expected, the energy splitting between these states increases with decreasing intervacency distance. Furthermore, VSs and LISs of vacancy chains form 1D quantum-well states. The VS levels of the chains could be well described by a simple tight-binding model that takes the electrostatic interaction between neighboring vacancies into account. The decreased level broadening observed for longer chains and the enlargement of the level splitting predicted by theory are clear signatures of the effect of electron-phonon interaction on the delocalization of electronic states. The results shown here prove that coupled defect states represent a possible option for the construction of conducting wires on insulating surfaces.

9.3. Au atoms on NaCl(2ML)/Cu(111)

9.3.1. Au^- , Au^0 & Au^+ : Charge state tristability

Stabilizing and controlling the charge state of atoms and molecules is of great interest regarding molecular scale memories and gates in the framework of molecular electronics. The charge state also governs many physical and chemical processes. Moreover, the study of these charging phenomena on an atomic level has ramifications for our understanding of local polaron formation, electron transfer, and electron solvation²⁶³ in a condensed environment, as well as for catalysis on supported metal atom clusters²⁶⁴. Along with the charge state control of the Au adatom that we study here comes the control of its magnetic moment. The neutral adatom (Au^0) exhibits a partially occupied $6s$ state resulting in a net (spin) magnetic moment, therefore being paramagnetic. For the Au anion (Au^-) this state is fully occupied and hence renders Au^- diamagnetic.

Especially KPFM has proven the feasibility to probe directly single-electron charges with atomic resolution³¹. Key to the multistability of charged atoms on NaCl are large ionic relaxations (polarizability) of the film in response to the additional charge³⁰. Charge-state manipulation has been shown for single atoms^{30,265–267}, defects²⁶⁸ and molecules⁹⁶ on bi- and multi-layer NaCl films. In particular charge-state tristability of Au adatoms (Au^0 , Au^- and Au^+) on multilayer NaCl has been reported recently²⁶⁷. Here, we briefly review the manipulation protocols, appearance of the different Au charge states in STM and measurement characteristics through which they can be identified.

After evaporation the Au atoms are found as Au^0 . One electron can be added by an electron attachment process by ramping the sample voltage to $V \gtrsim 0.8$ V. Due to the electronic decoupling, most electrons that tunnel resonantly into the empty Au $6s$ state are sufficiently long-lived that the NaCl film has time to relax lowering the energy of the Au anion below the Fermi energy, such that the tunneling electron is captured³⁰. The lattice relaxations also introduce an energy barrier that prevents the decay into the favored Au^0 state. This process is highly efficient with a switching probability per tunneling electron on the order of unity. Similarly, an electron detachment from Au^0 can be triggered by a voltage ramp to $V \lesssim -2$ V. Both, electron attachment and detachment are reversible. It should be noted, however, that the neutralization of the Au^+ state

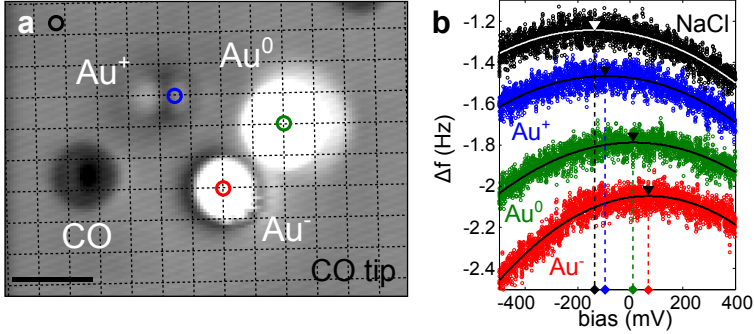


Figure 9.11.: **Au⁻, Au⁰, Au⁺ charge state tristability.** **a** STM image of CO, Au⁺, Au⁻ and Au⁰ on NaCl(2ML)/Cu(111) measured with a CO tip. Crossings of the dashed grid mark Cl positions of the NaCl substrate. **b** $\Delta f(V)$ spectra recorded at the same height [$z = -2 \text{ \AA}$ from $I = 1.5 \text{ pA}$, $V = 0.3 \text{ V}$ above the bare NaCl(2ML)/Cu(111)] at the positions indicated in **a**. According to their relative shifts of the LCPD, the different Au states can be identified as Au⁺ ($V^* = -96 \text{ mV}$), Au⁰ ($V^* = 11 \text{ mV}$) and Au⁻ ($V^* = 68 \text{ mV}$). Scale bar: 10 \AA .

sometimes resulted in a segregation into the NaCl film often with the creation of surface defects. For this reason and due to its small corrugation, Au⁺ was overlooked in previous studies. The stability of the charged states mainly depends on the work function of the sample and electron affinity and ionization energy of the adatom, as well as the relaxation energy²⁶⁵.

In Fig. 9.11a a STM image of Au⁰, Au⁻ and Au⁺ is presented. With a CO tip (as well as with a metallic tip), Au⁰ appears as a single protrusion and Au⁻ has a sombrero-like shape. The Au⁺ corrugation is comparably much smaller (apparent height $\approx 0.2 \text{ \AA}$ at $I = 2 \text{ pA}$, $V = 0.2 \text{ V}$) and has a peanut-like shape with a CO tip, similar to Ag⁺^{88,265}. With a metallic tip, Au⁺ appears as protrusion with a neighbouring depression. In section 9.3.2 Au⁺ is characterized in detail. Au⁰ adsorbs on-top Cl and Au⁺ in a slightly off-centered bridge position. Interestingly, Au⁻ was observed on both on-top Cl (smaller protrusion in STM topography) and bridge site (bigger protrusion) as seen in Fig. 9.12a. The stabilization of Au⁻ on two different sites was assigned to the locally varying strain field entailed by the Moiré pattern of the incommensurate growth of NaCl(2ML) on Cu(111)²⁶⁹.

Here, we investigate the charged adsorbates in two ways: Indirectly exploit-

9. Atomic manipulation on insulators

ing the NaCl(2ML)/Cu(111) interface state (IS), and directly employing KPFM. Owing to the long-range electrostatic interaction, charged adatoms interact strongly with the IS electrons confined a few Ångströms underneath. Localized charges on top of the NaCl layer strongly scatter these IS electrons and lead to a circular standing-wave pattern around the adsorbate³⁰. But only positive charge forms an attractive potential giving rise to a bound localized interface-state, analogously to the Cl vacancy (cf. section 9.2)¹⁰⁹. This state can be detected below the IS band onset in tunneling spectroscopy (see Fig. 9.12k). Alternatively, the charge of adatoms can also be identified directly, by the LCPD shift. Regarding investigations on thicker insulating films the latter method is highly desirable, because it does not require a conductive tunneling junction. In Fig. 9.11b $\Delta f(V)$ parabolas recorded on Au⁰, Au⁻ and Au⁺ are shown. In agreement with the proposed charge states, the LCPD shifts towards lower voltages from Au⁻ to Au⁰ and from Au⁰ to Au⁺. It should be noted that the complicated adsorption structure of Au⁺ generates an electrostatic field that is reminiscent of a dipole field (see section 9.3.2 for details). Note that the absolute charge state of the atoms cannot be directly deduced from the LCPD values. Only the differences of the charge states are revealed by the relative differences of the LCPD measured above the atoms. It should also be noted that we compare here KPFM spectra at different lateral positions on a certain height (disregarding the different tip distances to the adsorbate). In more complicated systems, e.g. like a molecule, single spectra often fall short on revealing all aspects of the charge distribution and a full three-dimensional data set of $\Delta f(V)$ parabolas should be considered (see section 7.4).

9.3.2. Au⁺: Toggling the local electric field with an embedded adatom switch

The concept of using single atoms and molecules as functional elements in electronic devices was established several decades ago¹⁶⁶. Special interest in atomic-scale memory elements and switches arise especially for the study of single electron transport in molecular networks. Many atomic-scale switches have been identified and investigated by STM^{6,19,25,28,96,120,270–275} and AFM^{27,34,35,276,277}. Naturally, SPM techniques prevail the quest of finding suitable molecular switches due to their capability to image and manipulate adsorbates at the atomic scale. Conceptually, molecular switches can be classified by their actuation (e.g. by light, short-range forces, electric currents, electric fields, or other external stimuli) and

switching mechanism (e.g. change in adsorption geometry, charge state, magnetization, molecular conformation, or chemical composition and combinations thereof). In this section we study a geometrical switch formed by two adsorption states of Au^+ on $\text{NaCl}(2\text{ML})/\text{Cu}(111)^{\text{a}}$, which could be controlled by the force exerted by the microscope tip. It is demonstrated that the switching changes the electric field in its vicinity.

As discussed in the previous section, Au cations could be formed from neutral Au adatoms by detaching an electron via a positively biased tip²⁶⁷. The consecutive creation of Au^+ ions is shown in Fig. 9.12a-d. The STM images of the formed Au cations have an asymmetric appearance consisting of a protruding feature (bright contrast) next to a depression (dark contrast). As we will see later, the two topmost Au cations adopt equivalent adsorption sites bridging two Cl sites that are rotated by 90° with respect to each other. In the following we will use a Xe tip to increase the resolution in the STM topography. After image acquisition of Fig. 9.12e, the tip was moved to the lateral position indicated by the white circle and the tip-sample distance was decreased until a sudden jump in the Δf channel was observed. During the approach no sample bias was applied. The subsequently recorded image Fig. 9.12f, showed that the STM topography of Au^+ was mirror-reflected about a switching axis (indicated by the dashed line in the close-up inset). In Fig. 9.12f-h the three Au^+ have been sequentially and deliberately switched into the mirror reflected conformation.

The observation of a strong directional dependence of spontaneous switching events during AFM imaging in the constant-height mode sheds more light on the mechanism behind the Au cation switch, as shown in Fig. 9.13. The Au cation appeared as an oval depression surrounded by an off-centered protrusion in the Δf channel imaged with a Xe tip. Atomic resolution was obtained on the NaCl lattice with bright and dark contrast on the Na and Cl sites, respectively⁹⁴. From this we can assign the adsorption site of Au^+ to be on a near bridge site along the Cl rows. When the fast scan direction was oriented perpendicular to the switching axis (Fig. 9.13a), repeated bidirectional switching between the Left ('L') and Right ('R') states was observed for the Au cation. In contrast, only a single switching event was observed when the fast scan axis was aligned parallel to the switching axis

^aNote that the switch could also be realized on thicker NaCl films grown on different Cu facets. The adsorption properties of Au^+ , as well as the switching mechanism do not depend on the film thickness and the orientation of the Cu substrate.

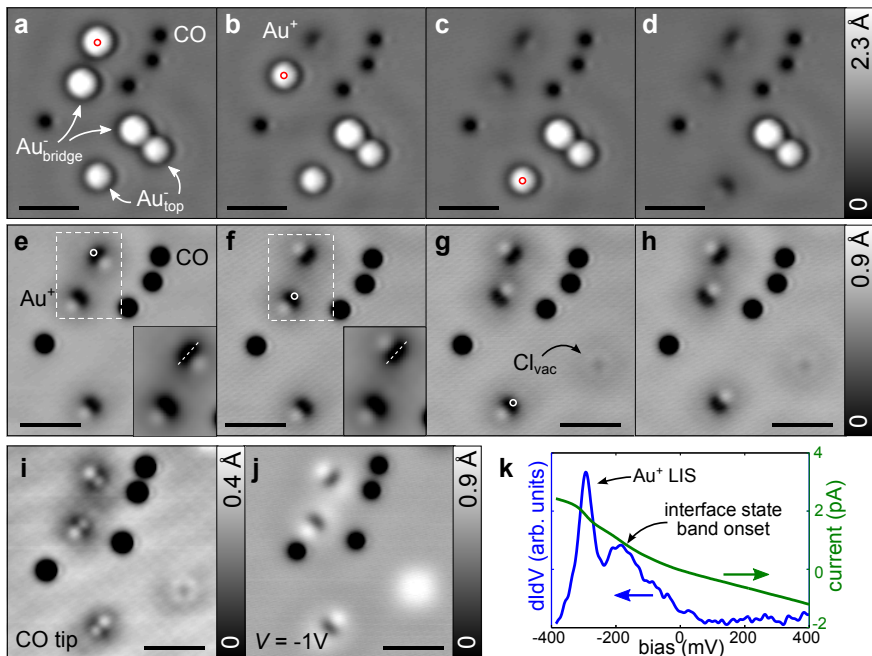


Figure 9.12.: **Au^+ creation and switch.** **a-d** STM images of Au^- (on Cl top and bridge sites) and CO (on Na sites) on $\text{NaCl(2ML)}/\text{Cu(111)}$. Au^- on bridge sites appear brighter than on Cl top sites. By applying voltage pulses of -1.7 V on Au^- (red circles), Au^- is switched to Au^+ . **e-h** STM images of Au^+ and CO recorded with a Xe tip. Au cations are sequentially switched between the two equivalent off-centered adsorption positions (tip position indicated by white circles). Insets show a close-up (white dashed rectangle) and indicate switching axis (white dashed line). **i** STM image recorded with a CO tip also reveals the asymmetric Au^+ state. **j** STM image with a Xe tip. The bright features centered at the Cl vacancy and the dark side of Au^+ belong to localized interface-states (LISs). STM images in **a-i** were acquired using ($I = 2$ pA, $V = 0.2$ V) and **j** using ($I = 2$ pA, $V = -1$ V). **k** Bias spectrum on Au^+ . Scale bars: 20 Å.

(Fig. 9.13b).

In Δf line scans displayed in Fig. 9.13c the influence of the tip-sample distance on the switching was analyzed. The locations of the line scans are indicated by red and blue arrows in Fig. 9.13a. Only a selection of the data is shown for the sake of clarity. The Au cation was initially in the 'L' state. The top three curves, which were recorded at the largest tip-sample distances, show a featureless depression at a lateral distance of -3 Å. At

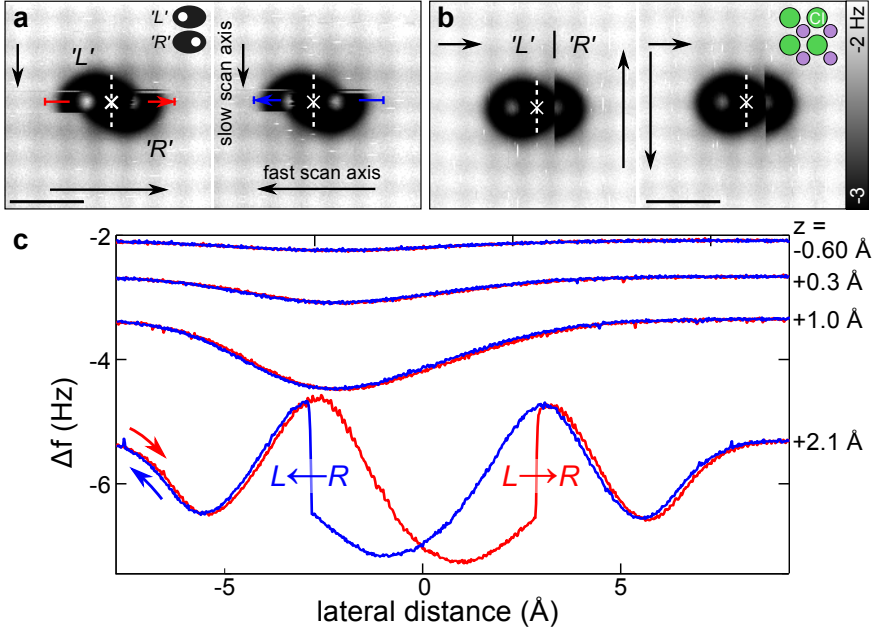


Figure 9.13.: **Au⁺ lateral manipulation.** **a,b** AFM maps of Au⁺ on NaCl(2ML)/Cu(111) with a Xe tip recorded in different scan directions (fast scan direction: long arrows, slow scan direction: short arrows). When the tip is scanned parallel to the switching direction (**a**), the Au⁺ geometry is switched in every scan line in the central part of the image. When the tip is scanned perpendicular to the switching direction (**b**), only one switching event occurs during one image. 'L' and 'R' denote the two geometry states where the bright Δf spot (which we identified as protruding Cl⁻) is left or right. The white dashed line indicates the switching axis. This axis is aligned with the bridge site (white cross). **c** AFM line scans at the position indicated by the colored arrows in **a**. z heights are given with respect to the STM set-point ($I = 2$ pA, $V = 0.2$ V). From a certain height on, the bright Δf spot seems to be pulled towards the tip. Scale bars: 10 Å.

a height set point comparable to the one in Fig. 9.13a,b, $z = 2.1$ Å, a hillock appears in the center of the depression. Furthermore, reversible switching between 'L' and 'R' states was observed in the forward and backward traces. Note that the switching from 'L' to 'R' states occurred almost precisely where the protrusion of the 'R' state was located, and vice versa. The same lateral switching positions were observed for all tip-sample distances between $z = 1.6$ Å and 2.1 Å but are not shown here. The Sader-Jarvis formalism⁶⁷, was used to extract the attractive vertical

9. Atomic manipulation on insulators

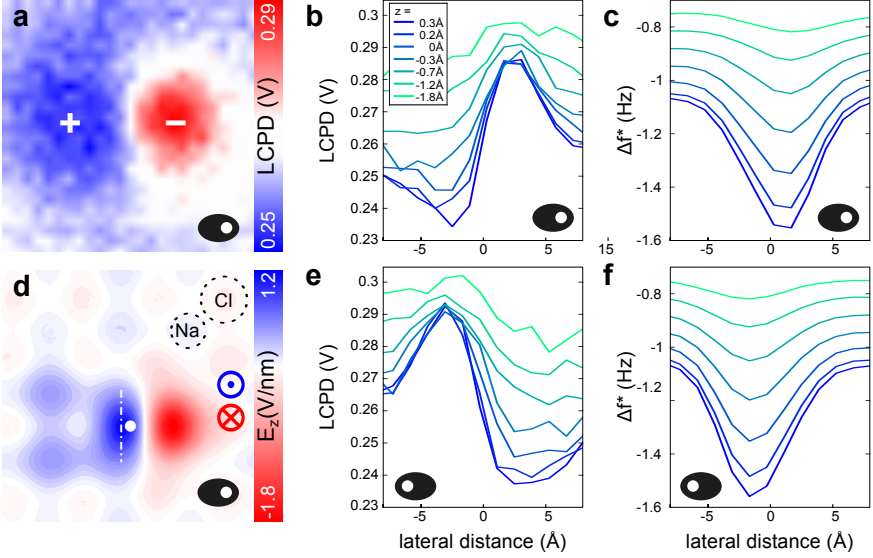


Figure 9.14.: Au^+ KPFM. **a** LCPD map ($z = 0 \text{ \AA}$, image size: $15 \times 15 \text{ \AA}^2$). The + and - signs indicate the anticipated local sample charges. **b,c** LCPD and corresponding Δf^* line scans at different heights. **d** Calculated electric field at a distance of 5 \AA from the top NaCl layer by DFT. The switching axis is indicated by a dash-dotted line. The position of the Au atom is indicated by the dot. In **a-d** Au^+ is in the 'R' state. **e,f** LCPD and Δf^* line scans at different heights, with Au^+ in the 'L' state. The measurements were recorded with a Xe tip. Tip heights are given with respect to a tunneling set point of ($I = 2 \text{ pA}$, $V = 0.2 \text{ V}$) above NaCl.

force, $F_z = -200 \pm 40 \text{ pN}$, from the Δf -line scans that was required to actuate the Au cation switch³⁴. Please note that force magnitude and direction ('pulling' vs 'pushing') of the actuation might depend on the tip termination.

In a LCPD map of the 'R' state (see Fig. 9.14a), one can recognize an LCPD decrease on the left (blueish contrast) and an LCPD increase on the right (reddish contrast), indicative of a positive and negative local charge, respectively. Line scans of LCPD and Δf^* across the Au cation switching axis at different heights are plotted in Fig. 9.14b,c, respectively. Clearly, the LCPD is increased to the right, where Δf^* is most attractive. This attractive electrostatic force arises from the interaction between the negative local charge mentioned before and the positively charged Xe tip⁹⁴. After switching from the 'R'- to 'L'-state (Fig. 9.14e,f), the LCPD

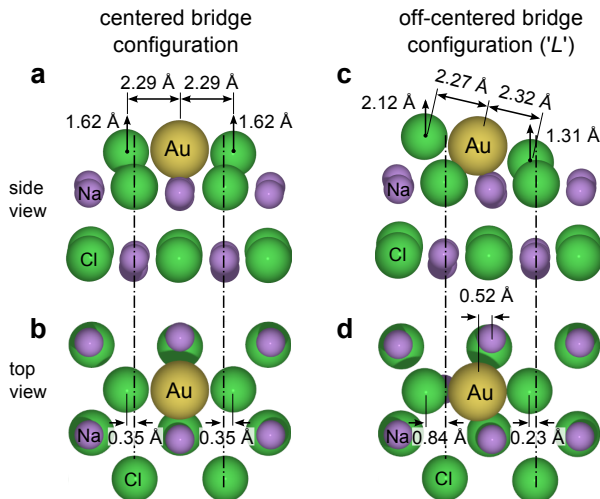


Figure 9.15.: **Calculated Au^+ geometry.** DFT calculated adsorption geometries of Au^+ on NaCl(2ML)/Cu(111). **a,b** Side-view and top-view of the symmetric Au^+ adsorption geometry on the bridge site. **c,d** Side-view and top-view of the asymmetric Au^+ adsorption geometry on the near bridge site. The $(\text{AuCl}_2)^-$ cluster is here in the 'L' configuration i.e. the Au adsorption site is shifted to the left with respect to the centered bridge position and the Cl^- to the left of the Au^+ is protruding more outwards.

contrast is essentially reversed and the attractive part is now to the left. Furthermore, the features with more positive LCPD in Fig. 9.14 emerge at the position of the bright protrusion of the respective state shown in Fig. 9.13. It should also be noted that the LCPD contrast above the positive charge decays faster than the one above the negative charge with increasing tip height, which we ascribe to a topographic effect as discussed below.

From DFT calculations based on a perfect conductor model^{278,279}, performed by Ivan Scivetti and Mats Persson, one meta-stable centered bridge configuration (Fig. 9.15a,b) and two equivalent off-centered configurations (Fig. 9.15c,d) for the Au^+ were identified. The latter configurations were found to be slightly more stable than the former configuration by 40 meV. As shown in Fig. 9.15c,d, the Au cation forms essentially a tilted linear complex, $(\text{AuCl}_2)^-$, with two Cl anions. The Au^+ complex resembles the Ag^+ complex on NaCl(2ML)/Cu(111)²⁶⁵ but in the latter case the complex is bent and only a centered configuration was identified. The formation of

9. Atomic manipulation on insulators

the tilted $(\text{AuCl}_2)^-$ complex gives rise to large charge rearrangements as illustrated by the associated large electric field in a plane 5 Å from the top NaCl layer, shown in Fig. 9.14d.

Based on our experimental results and DFT calculations, we relate the protruding features of the Au cation complex in the STM images shown in Fig. 9.12 and the corresponding protrusions in the AFM images in Fig. 9.13 to the strongly lifted Cl anions of the off-centered and tilted complex. The negative local charge at the position of the bright protrusions in Fig. 9.13, as revealed by the LCPD and Δf^* measurements in Fig. 9.14, supports this assignment. The presence of negative charge on this protruding Cl anion is demonstrated by the negative electric field in this region shown in Fig. 9.14d. Furthermore, the distance of ~ 6 Å between the protrusions of the 'L' and the 'R' states in Fig. 9.13a,b is in agreement with the corresponding calculated distance of 5.8 Å between the protruding Cl ions. Finally, note that the two orthogonal orientations of the Au cation switch, (see Fig. 9.12), are imposed by the bridge adsorption site and the four-fold axial symmetry of the NaCl film.

The atomistic insight into the nature of the Au cation complex gained from our experiments and DFT calculations suggests a force-actuated switching mechanism. According to Fig. 9.13, the switching occurred always at the position of the lower-lying Cl anion in the tilted, linear $(\text{AuCl}_2)^-$ complex. Apparently, the attractive force exerted by the tip 'pulled' this Cl anion atom upwards and forced the other Cl atom to move down, in analogy to a rocker switch. As a consequence, two bright protrusions shown in Fig. 9.13a,b, which are mirrored about the switching axis, correspond to the lifted Cl atoms in both conformations of the switch. A tunneling electron mechanism can be excluded since the switching occurred at zero voltage applied and the same switching behavior was observed also on thicker insulating NaCl films. The Au cation switch is thus an example of a purely force-actuated atom switch.

Actuation of the Au cation switch causes the LCPD to change locally by approximately 40 meV^a according to Fig. 9.14a. Recent work has shown that properties of single molecules and molecular ensembles can be influenced by changing their local chemical environment^{29,275,280,281}. For example, the orbital sequence of single Cu-phthalocyanine molecules could be controlled by

^aNote that the magnitude of this change is tip and height dependent.

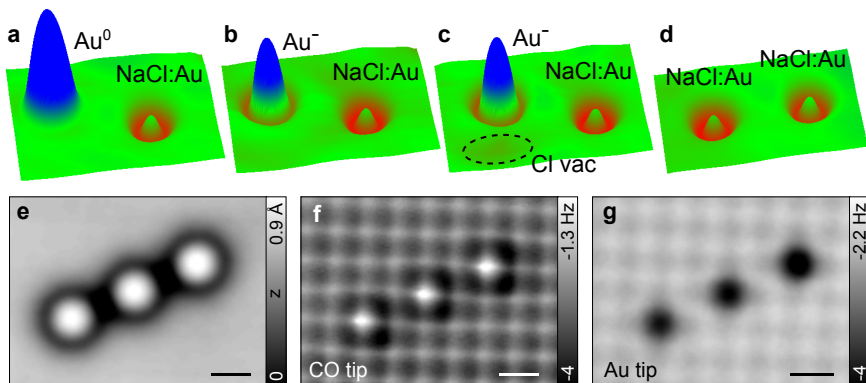


Figure 9.16.: **Au incorporation in NaCl.** **a-d** Series of STM images that shows the Au incorporation in NaCl(2ML)/Cu(111) ($I = 2 \text{ pA}, V = 0.2 \text{ V}$). After creating a Cl vacancy (c) the Au atom is laterally manipulated by voltage pulses of -1.4 V at about 20 pA . Thereby, the charge state of Au can be changed between neutral (Au^0) and negatively charged (Au^-) until Au replaces the missing Cl atom (NaCl:Au). Thereafter the Au atom can neither be moved nor its charge state changed. **e** STM image of three Au^- impurities in NaCl(2ML)/Cu(111) ($I = 20 \text{ pA}, V = 0.2 \text{ V}$). **f/g** AFM map of the same NaCl:Au chain with a CO/Au tip. Scale bars: 5 \AA .

changing the distance between Au and Ag atoms placed in the proximity of the molecule²⁷⁵. In a similar fashion, the intramolecular hydrogen-transfer reactions in single porphycene molecules on a Cu(110) surface could be controlled by placing a Cu atom nearby²⁹. These examples indicate that the Au cation switch could be used to control the properties of single molecules through its electrostatic field. Importantly, the $(\text{AuCl}_2)^-$ complex that is formed is embedded in the NaCl film, which makes this switch especially robust against external perturbations.

9.3.3. Au incorporation in NaCl with atomic precision

Material doping by introducing foreign atoms into a host crystal is an incredibly successful concept to tune material properties and is widely applied for semiconductors. On semiconductor surfaces, efforts have been made to measure and control the doping even on the atomic-scale²⁴⁶ including precise dopant placement by atom manipulation^{276,277} or hydrogen lithography²⁸². Also for insulators, such doping is known to affect catalytic, optical, magnetic and transport properties²⁸³. However, atom manipulation on insulators is particularly challenging owing to the lower

9. Atomic manipulation on insulators

binding energy of adsorbates and the restriction to AFM. Nonetheless, it has been reported recently that Br atoms can be vertically manipulated and implanted into NaCl by a statistical exchange mechanism with an AFM tip²⁸⁴. Though, replacing Br by Cl will not significantly change the material properties, as both belong the same chemical group. Lately, Li *et al.* have shown that (magnetic) Co atoms are directly incorporated in NaCl upon adsorption at low temperatures, by substituting either Na or Cl atoms²⁸⁵. In contrast, we have seen in the previous sections that Au adsorption on NaCl/Cu is noninvasive, leaving the insulating film undamaged. However, in sections 6.3 and 9.2 it was demonstrated that defects can also be introduced artificially by atomic manipulation using the tip. In the following we will see how a combination of manipulation techniques can be used to incorporate Au atoms in the NaCl film with atomic precision.

The Au implantation into the NaCl film is possible by ‘pushing’ the Au adatom into a Cl vacancy. A series of manipulation events to incorporate a Au atom at a former Cl site is presented in Fig. 9.16a-d. First, a vacancy is created as described in section 6.3. Thereafter, the Au adatom is laterally manipulated by negatively charging and discharging the Au adatom. Since Au^0 and Au^- can have different adsorption sites, a charging/discharging event is often accompanied by a lateral displacement of the atom, predominantly in the direction of the tip. The last displacement after which the Au atom is found at the former vacancy position is typically larger, revealing the affinity of Au to move to the vacancy site. In STM, the implanted Au atom (NaCl:Au) has a sombrero-like appearance similar to Au^- , but with a significantly smaller protrusion in the center (see Fig. 9.16b). In Fig. 9.16f a CO tip AFM image of three NaCl:Au atoms aligned in a chain are shown. Clearly, the incorporated Au atoms are built into the lattice at Cl sites. The IS scattering, present for the Cl vacancy, is strongly suppressed when it is filled by the Au atom. Accordingly, NaCl:Au is likely singly negatively charged and compensates for the missing Cl^- ion. With a Au tip, the NaCl:Au sites appear more attractive than the NaCl lattice (Fig. 9.16g). From the atomic resolution images no apparent distortions of the lattice are observed (unlike for the Cl vacancy).

Evidence for the negative charge of NaCl:Au is also provided by the KPFM measurement shown in Fig. 9.17. Here, the same NaCl:Au chain as in Fig. 9.16e-g is investigated. At positions of the Au impurities, the LCPD is shifted towards larger values, indicative of excessive negative charge. Apparently, the LCPD (and Δf^*) contrast is more pronounced compared

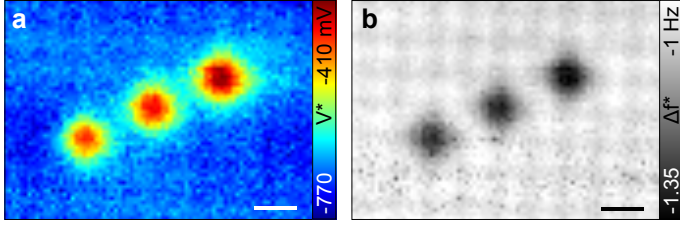


Figure 9.17.: **NaCl:Au chain KPFM.** **a** LCPD map of the NaCl:Au chain shown in Fig. 9.16 recorded with a Au tip. **b** Corresponding Δf^* map. Scale bars: 5 Å.

to Cl^- sites. This might be related to the outwards protrusion of the Au atom as argued in the following.

In Fig. 9.18 the results of a 3D forcemap recorded with CO tip on the same NaCl:Au chain as discussed before are presented. Different constant-height slabs of this measurements are illustrated in Fig. 9.18a-c and single $\Delta f(z)$ spectra at the NaCl:Au, Cl, Na and Na next to NaCl:Au sites are compared in Fig. 9.18d. Qualitatively, the curve form of NaCl:Au (Fig. 9.18d blue) resembles the one on the Cl site (Fig. 9.18d cyan). Both start a repulsive branch around $z = 1.5 \text{ \AA}$, become attractive again before finally repulsion sets in at very close distance. It can be assumed that these spectra are dominated by the CO tilting (discussed in sections 7.1 and 7.2): First, the CO 'sees' the bigger anion (Au^- or Cl^-) leading to the first repulsive branch but is deflected towards the Na site at close distance. The NaCl:Au curve is, however, shifted towards larger distances compared to the Cl curve, indicating that the Au impurity is protruding outwards (assuming the ionic radii of Cl and Au to be similar). Due to this z shift, NaCl:Au and Cl undergo several contrast inversions in Δf . Striking differences can also be recognized between Na (Fig. 9.18d red) and the Na next to the Au impurity (Fig. 9.18d brown). At farther distances (Fig. 9.16f or Fig. 9.18a) Na next to NaCl:Au are more attractive than other Na sites, leading to a dark contrast surrounding the Au impurity. At close distance (Fig. 9.18c) the Δf contrast is reversed, the Na next to NaCl:Au appears more repulsive than other Na sites. These differences might arise from polarization effects in the vicinity of the impurity.

The results provided here demonstrate the creation of a Au atom inlay²⁷⁶. That is, the artificial creation of an atomic pattern formed from a few embedded atoms in the plane of a surface templated by Cl vacancies. Further

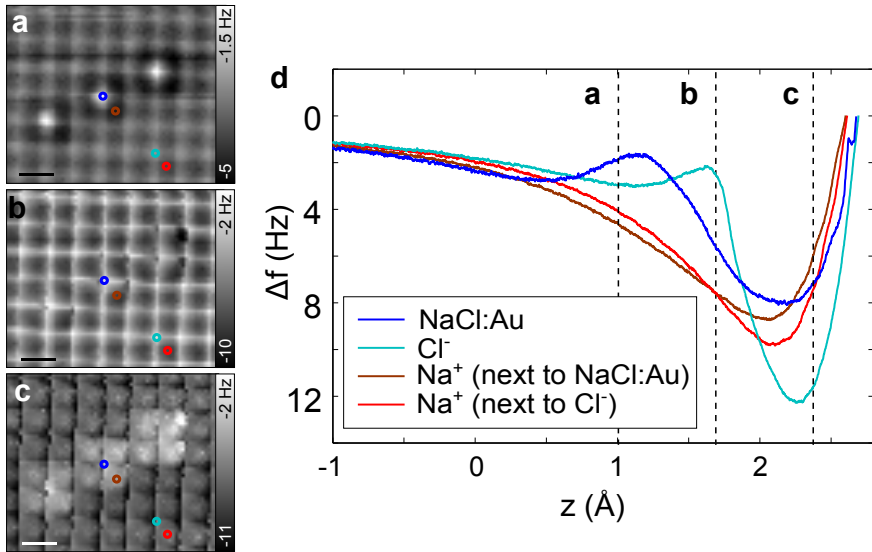


Figure 9.18.: **NaCl:Au chain 3D forcemap.** 3D forcemap on the NaCl:Au chain shown in Fig. 9.16e-g recorded with a CO tip. **a-c** Constant height slabs from the forcemap at $z = 1 \text{ \AA}$ (**a**), 1.7 \AA (**b**) and 2.4 \AA (**c**) where $z = 0$ is the tip height at the STM set point ($I = 2 \text{ pA}$, $V = 0.2 \text{ V}$). **d** Individual $\Delta f(z)$ spectra extracted from the same 3D forcemap at the locations indicated by the circles in **a-c**. The dashed vertical lines indicate the height where the constant height slabs in **a-c** are shown. Scale bars: 5 \AA .

investigations might be performed to analyze the stability of such atomic structures. It might also be interesting to study the capturing process of diffusing Au atoms in the presence of (diffusing) Cl vacancies (created for example by field emission) at elevated temperatures or potential pinning of metalated molecules (e.g. metal-phthalocyanines) to vacancy sites. In addition, incorporation of foreign atoms by deliberately filling manually created vacancies may be applicable to a broad range of atoms. In particular, this system might be suited to study magnetic interactions between magnetic impurities embedded in an insulating matrix.

CHAPTER 10

Conclusions

In this thesis we have discovered that a tremendous richness of detail and deep level of understanding of atomic-scale objects can be revealed by combining STM, AFM and KPFM, exploiting the contrast enhancements with functionalized tips. All three techniques yield complimentary information about the system under investigation, which was applied to learn about the atomic and electronic structure of single molecules, defects and atoms on NaCl(2ML)/Cu(111).

In chapter 6, methods were described how tips can be terminated by individual Cl, Br, I, Xe and Kr atoms and CO and NO molecules and we assessed their performance for STM and AFM operation on molecules. We found that CO tips excelled for AFM imaging due to the high resolution and stability, with the drawback of inducing strong image distortions from the tilting of the CO tip. Br tips are suited for undistorted AFM imaging and lateral manipulation (along with I), whereas Xe tips are highly stable, making them attractive for STM orbital imaging and KPFM. In section 6.3, single Cl vacancies were created to ascertain the underlying contrast mechanism of AFM on ionic surfaces by means of different tip functionalizations. It was found that atomic-resolution AFM images on ionic surfaces show a strong voltage- and tip-dependence, identifying electrostatic forces as the main contribution to the contrast. On the contrary, almost no tip dependence was observed in KPFM maps, except for a constant offset.

In chapter 7 we investigated how different molecular properties influence the measured AFM and KPFM signals and exploited this to extract qualitative and quantitative information about molecular model systems. High-resolution AFM imaging turned out to be a unique analytic chemistry tool, capable of studying individual molecules and even addressing single bonds. In section 7.1 the bond order of single carbon-carbon bonds could be discriminated by two contrast mechanisms: First, bonds of higher

10. Conclusions

bond order appear brighter, resulting from their increased electron density. Second, bonds of higher bond order appear shorter. The difference in apparent bond length are, however, significantly exaggerated, which can be traced back to the CO tip tilting. In section 7.3, it was described how the adsorption geometry of molecules can be extracted from force–distance spectroscopy; Providing a very sensitive method for the detection of relative adsorption heights and marking a first step to extract quantitative information by AFM. As a different topic, the contrast formation in KPFM on several charge-transfer complexes was inspected in section 7.4. Three distance regimes were identified: Far away, the LCPD contrast resembles the electrostatic far-field with dominant contributions from electric monopoles and dipoles. At distances similar to the molecule dimensions, the LCPD contrast still corresponds to the electrostatic field, but is dominated by higher-order multipoles. In this regime, considering only partial charges falls short of explaining the contrast. At very small distances, the LCPD strongly drops at regions of repulsive interaction, which can be understood in terms of a local penetration of the tip into the electron density of the molecule.

In chapter 8, we applied the method of high-resolution AFM imaging with CO tips and STM orbital imaging for the verification of synthetic compounds and identification of natural products. First, the structure of a large, practically insoluble synthetic polyaromatic hydrocarbon was verified and a reaction side-product detected. Then, the newly discovered structure of Breitfussin A could be identified by combining AFM with conventional state-of-the-art structure elucidation techniques. The demonstrated *modus operandi* constituted a perfect case study to describe when and in which way AFM might be applicable for structure identification of molecules in general. Thereafter, we went a step further, by analyzing one of the most complex natural mixtures existing: Asphaltenes. Here, we could resolve a long-standing debate about asphaltene molecular architecture and uncover the tremendous diversity of molecular structures nature has to offer.

In addition to tip functionalization, we employed the potential of atomic manipulation on insulators in chapter 9 in different ways: First, two examples of single-molecule reactions induced by STM manipulation were reported. In the first example, DINP was dehalogenated and we could verify the successful creation and stabilization of the highly reactive aryne molecule. It could be demonstrated that the insulating layer enables the isolation of the reactive intermediate and that its reactivity is preserved at

cryogenic temperatures. In the second example, DBA was debrominated to dehydroanthracene. Subsequently, we could trigger a retro-Bergman cyclization reaction, which could be reversibly performed demonstrating the reversible breaking and making of covalent intramolecular bonds. In section 9.2, Cl vacancy pairs and chains were created to study the effect of strong electron–phonon interaction on the formation of one-dimensional electronic states. As expected, the energy splitting between the symmetric and anti-symmetric vacancy state and localized interface-state of divacancies increases with decreasing inter-vacancy distance. Remarkably, the energy splitting of the vacancy states is enlarged by level repulsion resulting from the electron–phonon interaction. In section 9.3, we analyzed the adsorption characteristics of different charge states of Au adatoms in detail. The Au cation could be mechanically switched between two equivalent sites. The switching inverts the local dipole, which stems from the dramatic rearrangement of the next-nearest Cl anions. In addition, the atomic-precise implantation of Au atoms in the NaCl film was demonstrated.

The findings reported here tackle a wide range of different problems, with ramifications for different fields: It improved our understanding of the relevant contrast mechanisms in different SPM modes; we could explore the usefulness of SPM as analytical tool for chemistry and surface science; it gave us deep insights into atomic-scale processes in molecular systems on surfaces and it allowed us to study fundamental physical phenomena such as delocalization of electrons and electron–phonon interactions.

Part IV.

Appendix

APPENDIX A

Density functional theory calculations

The DFT calculations in section 7.4, chapter 8 and section 9.1 and in this appendix were carried out for a free molecule, using the highly optimized plane-wave code CPMD²⁸⁶. The Perdew–Burke–Ernzerhof (PBE) exchange–correlation functional¹⁶² was used with *ab initio* norm-conserving pseudopotentials²⁸⁷ created according to the scheme of Trouiller and Martins²⁸⁸. The pseudopotential method provides an accurate description of valence electrons outside the core region (e.g. around 0.6 Å for C atoms), whereas the core electrons are eliminated within the frozen-core approximation. Thereby, the pseudopotentials replace electronic degrees of freedom in the Hamiltonian by an effective potential. They lead to a reduction of the number of electrons in the system and hence allow for faster calculation or the treatment of bigger systems. This approximation yields an excellent description of the total electron density at distances relevant in this thesis. The size of the unit cells in our calculations was chosen to be at least three times the size of the largest molecule dimension. The structural optimization was performed until the forces on all atoms were below $5 \cdot 10^{-5}$ eV/Å, and a cutoff energy of 100 Ry (≈ 1.4 keV) was used for a single k point (Γ). The z -component of the electric field was obtained by differentiating the calculated electrostatic potential with respect to z .

Note that the DFT and/or model calculations discussed in the sections 7.1, 7.2, 7.3, 9.2 and 9.3.2 were performed by other people (see [Contributions to this work](#)) using different codes. Please refer to the respective sections or referred publications therein for details.

A.1. Charge-transfer complexes

In this section additional calculations of the z -component of the electrostatic field (E_z) of the charge-transfer complex (CTC) TTF-PYZ₂ as discussed in section 7.4 are provided. Specifically the distance dependence

A. Density functional theory calculations

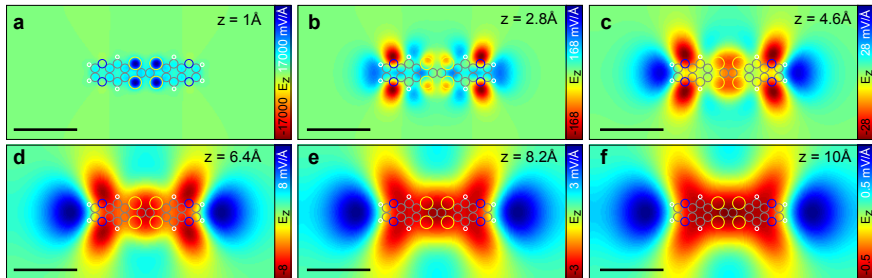


Figure A.1.: **Electrostatic field of TTF-PYZ₂.** **a-f** Calculated z -component of the electrostatic field (E_z) at different (equidistant) heights z with the molecule model overlaid. Scale bars: 10 Å.

of E_z before and after the intramolecular charge transfer transition (ICT) is analyzed.

In Fig. A.1, E_z above TTF-PYZ₂ is plotted at different distances from the molecule. In the regime up to about 5 Å, E_z is subject to qualitative contrast changes. Further away, however, the contrast persists qualitatively, but changes in its strength. The measured LCPD contrast at moderate distances for both conformations is in good agreement with this E_z -field further away. Note that this E_z contrast is reminiscent of two opposing dipoles in the order (+ -) and (- +). But in this CTC molecule, the sequence is exactly opposite: acceptor (-) to the left, donor (++) in the center and acceptor (-) to the right, which is also corroborated by the calculated partial charges of the donor and acceptor components (see Fig. 7.21a). This again demonstrates that E_z and hence the LCPD cannot be translated directly into the partial charge at a certain position.

It should be noted that the simplified calculations used here shows very good agreement with the experiments, although it neglects all influences of the tip and sample. However, quantitatively there might be influences of both tip and sample. For example tip dipoles or the electrostatic field of the ionic substrate⁹⁷ might induce small atom displacements in the molecule or polarize the molecule.

We also examined the ICT of the charge-transfer complexes, where an electron is excited from the HOMO localized on the TTF to the LUMO localized on the acceptor. In Fig. A.2, the calculated E_z of TTF-PYZ₂ in this excited

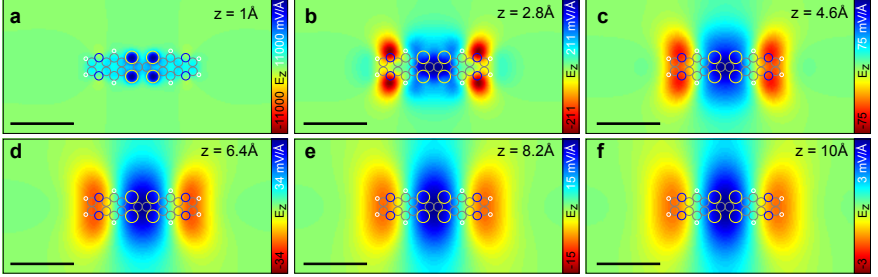


Figure A.2.: **Electrostatic field of TTF-PYZ₂ after the intramolecular charge transfer transition (ICT).** **a-f** Calculated z -component of the electrostatic field (E_z) at different (equidistant) heights z of TTF-PYZ₂ after the transition of one electron from the HOMO to the LUMO (ICT) with the molecule model overlaid. The simplification has been made that the geometry of the charge-transfer state is the same as in the ground state. Note that the scales are slightly different compared to Fig. A.1. Scale bars: 10 Å.

state is shown. Strikingly, the E -field in the excited state looks qualitatively very different compared to the E -field in the ground state (cf. Fig. A.1). After the ICT, the E -field from about $z \approx 4$ Å on clearly resembles a field that can be described by two opposing dipoles in the sequence $(- + + -)$, as expected after donation of one electron from the center to the molecule's ends. In this case, the large partial charges (on the order of $1e$) are the pre-dominating effect for the E -field contrast. Note that the E -field strength in the medium distance regime is approximately by a factor of 5 larger for the molecule after the ICT than the molecule in the ground state (compare Fig. A.1d-f with Fig. A.2d-f). We were not able to measure the molecule in the ICT state by scanning probe microscopy, because of the short lifetime (in the range of ps) of the excitation.

A.2. Asphaltenes

In this section, we present molecular orbital (MO) calculations for the coal-derived asphaltene molecules **CA2** and **CA3** discussed in section 8.3. The proposed structures are based on the measured AFM images of the respective molecule. The MOs are calculated using DFT as described above.

For **CA2**, the molecular structure of the entire molecule could be readily identified from the AFM measurement (cf. Fig. A.3a and Fig. A.3d). The calculated HOMO (Fig. A.3e) and LUMO (Fig. A.3f) are in good agreement with the measured orbitals (Fig. A.3b,c). The deviations in the

A. Density functional theory calculations

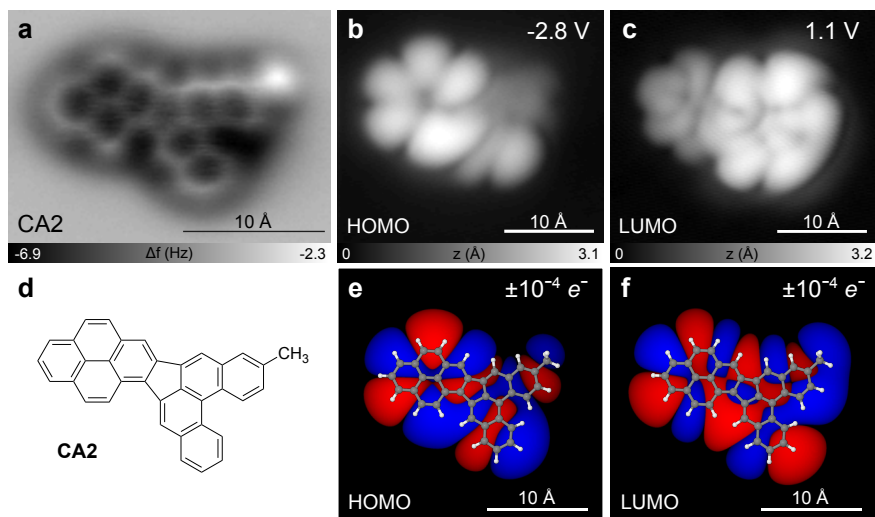


Figure A.3.: **CA2** calculated orbitals. **a** AFM image of **CA2** on NaCl(2ML)/Cu(111). **b,c** STM orbital images of **CA2** of the PIR (**b**) and the NIR (**c**). **d** Structural model of **CA2**. **e,f** HOMO (**e**) and LUMO (**f**) orbital of the structure in **d**.

LUMO can be explained by the small calculated energy difference between LUMO and LUMO+1 ($\Delta E = 0.25$ eV). As the MOs are significantly vibronically broadened on the NaCl film¹⁰⁹, both levels contribute to the measured STM orbital image²⁷⁵.

The situation is less clear for **CA3**. Here, the molecular structure could only be partially resolved by AFM owing to the reduced contrast in certain parts of the molecule. Consequently, various structure proposals are legitimate. Some structure guesses are shown in Fig. A.4a. The unknowns here are the moieties at the five-membered rings. Possible are CH, CH₂ or CO moieties or ring substitutions by N, NH or S. However, the heteroatom content in CA is relatively low, which renders the heteroatom substitution of the pentagonal rings less likely. In Fig. A.4d-o MO calculations are shown for the different structure hypotheses sketched in Fig. A.4a. Apparently, many orbitals share common motifs. However, only for a small number of structures are both the HOMO and the LUMO in reasonable agreement with the measured orbitals shown in Fig. A.4b,c. The best match is achieved for the structures shown in Fig. A.4f and Fig. A.4n. Note that both structures

have a singly occupied HOMO in the neutral state. However, we observe a distinctively different positive (PIR) and negative ion resonance (NIR) for **CA3**, which excludes the possibility of a radical. Possibly, the molecule could be charged by one electron^a, which would fill up the semi-occupied HOMO. In addition, we performed further MO calculations using other molecule hypothesis (especially different PAH ring geometries) that showed less agreement with the measured orbitals.

^aMolecules can be charged depending on the level alignment of their states with the Fermi energy of the surface.

A. Density functional theory calculations

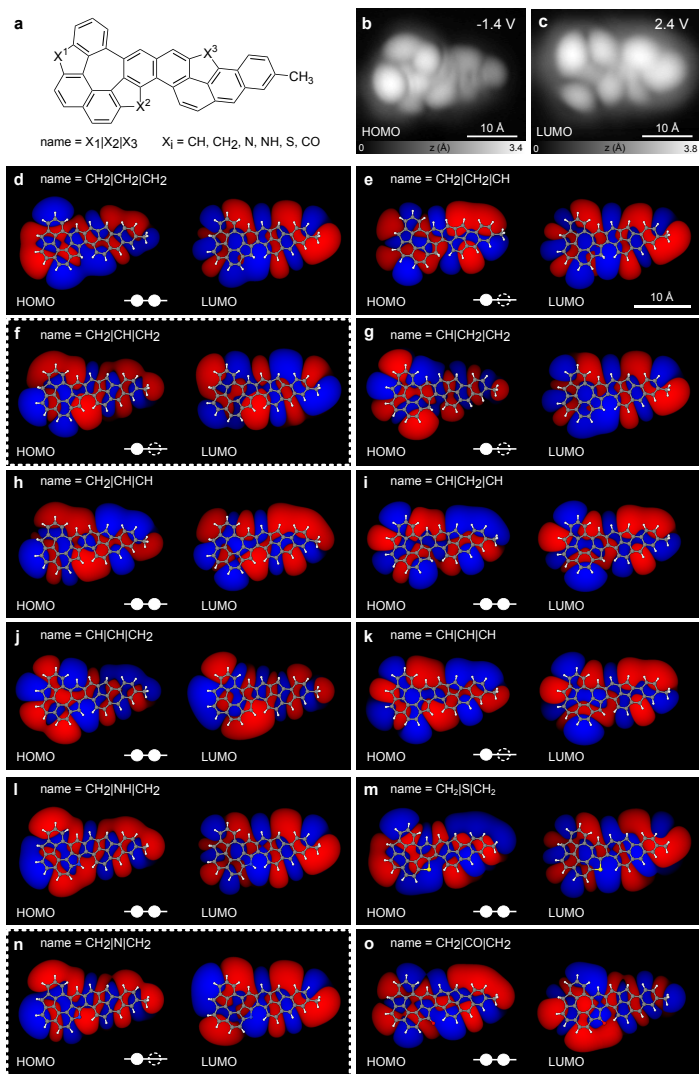


Figure A.4: **CA3** calculated orbitals. **a** Different possible structures of **CA3**. **b,c** STM orbital images of **CA3** of the PIR (**b**) and the NIR (**c**). **d-o** HOMO and LUMO orbital isosurfaces (at $\pm 10^{-4} e^-$) using the different structure hypotheses shown in **a**. The structures in **f** and **n** (dashed white box) show the best agreement with the measured orbitals. The two white circles indicate whether the molecule has a singly (filled) and empty circle) or a doubly (two filled circles) occupied HOMO in the neutral state.

Bibliography

- [1] Binnig, G., Rohrer, H., Gerber, C. & Weibel, E. [Tunneling through a controllable vacuum gap](#). *Appl. Phys. Lett.* **40**, 178–180 (1982).
- [2] Feynman, R. P. [There's plenty of room at the bottom](#). *Engineering and Science* **23**, 22–36 (1960).
- [3] Binnig, G., Quate, C. F. & Gerber, C. [Atomic force microscope](#). *Phys. Rev. Lett.* **56**, 930–933 (1986).
- [4] Binnig, G., Rohrer, H., Gerber, C. & Weibel, E. [7×7 reconstruction on Si\(111\) resolved in real space](#). *Phys. Rev. Lett.* **50**, 120–123 (1983).
- [5] Eigler, D. M. & Schweizer, E. K. [Positioning single atoms with a scanning tunnelling microscope](#). *Nature* **344**, 524–526 (1990).
- [6] Eigler, D. . M., Lutz, C. & Rudge, W. [An atomic switch realized with the scanning tunnelling microscope](#). *Nature* **352**, 600–603 (1991).
- [7] Crommie, M. F., Lutz, C. P. & Eigler, D. M. [Confinement of electrons to quantum corrals on a metal surface](#). *Science* **262**, 218–220 (1993).
- [8] Heinrich, A., Lutz, C., Gupta, J. & Eigler, D. [Molecule cascades](#). *Science* **298**, 1381–1387 (2002).
- [9] Lee, H. J. & Ho, W. [Single-bond formation and characterization with a scanning tunneling microscope](#). *Science* **286**, 1719–1722 (1999).
- [10] Hla, S.-W., Bartels, L., Meyer, G. & Rieder, K.-H. [Inducing all steps of a chemical reaction with the scanning tunneling microscope tip: Towards single molecule engineering](#). *Phys. Rev. Lett.* **85**, 2777–2780 (2000).
- [11] Hahn, J. & Ho, W. [Oxidation of a single carbon monoxide molecule manipulated and induced with a scanning tunneling microscope](#). *Phys. Rev. Lett.* **87**, 166102 (2001).
- [12] Repp, J., Meyer, G., Paavilainen, S., Olsson, F. E. & Persson, M. [Imaging bond formation between a gold atom and pentacene on an insulating surface](#). *Science* **312**, 1196–1199 (2006).
- [13] Joachim, C., Gimzewski, J. K., Schlittler, R. R. & Chavy, C. [Electronic transparency of a single C₆₀ molecule](#). *Phys. Rev. Lett.* **74**, 2102–2105 (1995).

- [14] Pump, F. *et al.* [Quantum transport through STM-lifted single PTCDA molecules.](#) *Appl. Phys. A* **93**, 335–343 (2008).
- [15] Lafferentz, L. *et al.* [Conductance of a single conjugated polymer as a continuous function of its length.](#) *Science* **323**, 1193–1197 (2009).
- [16] Stipe, B. C., Rezaei, M. A. & Ho, W. [Single-molecule vibrational spectroscopy and microscopy.](#) *Science* **280**, 1732–1735 (1998).
- [17] Qiu, X. H., Nazin, G. V. & Ho, W. [Vibronic states in single molecule electron transport.](#) *Phys. Rev. Lett.* **92**, 206102 (2004).
- [18] Qiu, X., Nazin, G. & Ho, W. [Vibrationally resolved fluorescence excited with submolecular precision.](#) *Science* **299**, 542–546 (2003).
- [19] Wu, S. W., Ogawa, N. & Ho, W. [Atomic-scale coupling of photons to single-molecule junctions.](#) *Science* **312**, 1362–1365 (2006).
- [20] Zhang, R. *et al.* [Chemical mapping of a single molecule by plasmon-enhanced Raman scattering.](#) *Nature* **498**, 82–86 (2013).
- [21] Repp, J., Fölsch, S., Meyer, G. & Rieder, K.-H. [Ionic films on vicinal metal surfaces: Enhanced binding due to charge modulation.](#) *Phys. Rev. Lett.* **86**, 252–255 (2001).
- [22] Heinrich, A. J., Gupta, J. A., Lutz, C. P. & Eigler, D. M. [Single-atom spin-flip spectroscopy.](#) *Science* **306**, 466–469 (2004).
- [23] Loth, S., Etzkorn, M., Lutz, C. P., Eigler, D. & Heinrich, A. J. [Measurement of fast electron spin relaxation times with atomic resolution.](#) *Science* **329**, 1628–1630 (2010).
- [24] Hirjibehedin, C. F., Lutz, C. P. & Heinrich, A. J. [Spin coupling in engineered atomic structures.](#) *Science* **312**, 1021–1024 (2006).
- [25] Loth, S., Baumann, S., Lutz, C. P., Eigler, D. M. & Heinrich, A. J. [Bistability in atomic-scale antiferromagnets.](#) *Science* **335**, 196–199 (2012).
- [26] Repp, J., Meyer, G., Stojković, S., Gourdon, A. & Joachim, C. [Molecules on insulating films: Scanning-tunneling microscopy imaging of individual molecular orbitals.](#) *Phys. Rev. Lett.* **94**, 026803 (2005).
- [27] Mohn, F. *et al.* [Reversible bond formation in a gold-atom-organic-molecule complex as a molecular switch.](#) *Phys. Rev. Lett.* **105**, 266102 (2010).
- [28] Liljeroth, P., Repp, J. & Meyer, G. [Current-induced hydrogen tautomerization and conductance switching of naphthalocyanine molecules.](#) *Science* **317**, 1203–1206 (2007).

- [29] Kumagai, T. *et al.* Controlling intramolecular hydrogen transfer in a porphycene molecule with single atoms or molecules located nearby. *Nature Chem.* **6**, 41–46 (2014).
- [30] Repp, J., Meyer, G., Olsson, F. E. & Persson, M. Controlling the charge state of individual gold adatoms. *Science* **305**, 493–495 (2004).
- [31] Gross, L. *et al.* Measuring the charge state of an adatom with noncontact atomic force microscopy. *Science* **324**, 1428–1431 (2009).
- [32] Albrecht, T. R., Grütter, P., Horne, D. & Rugar, D. Frequency modulation detection using high-Q cantilevers for enhanced force microscope sensitivity. *J. Appl. Phys.* **69**, 668–673 (1991).
- [33] Giessibl, F. J. Atomic resolution of the Si(111)-(7×7) surface by atomic force microscopy. *Science* **267**, 68–71 (1995).
- [34] Ternes, M., Lutz, C. P., Hirjibehedin, C. F., Giessibl, F. J. & Heinrich, A. J. The force needed to move an atom on a surface. *Science* **319**, 1066–1069 (2008).
- [35] Loppacher, C. *et al.* Direct determination of the energy required to operate a single molecule switch. *Phys. Rev. Lett.* **90**, 066107 (2003).
- [36] Sugimoto, Y. *et al.* Chemical identification of individual surface atoms by atomic force microscopy. *Nature* **446**, 64–67 (2007).
- [37] Kaiser, U., Schwarz, A. & Wiesendanger, R. Magnetic exchange force microscopy with atomic resolution. *Nature* **446**, 522–525 (2007).
- [38] Gross, L., Mohn, F., Moll, N., Liljeroth, P. & Meyer, G. The chemical structure of a molecule resolved by atomic force microscopy. *Science* **325**, 1110–1114 (2009).
- [39] Gross, L. *et al.* Organic structure determination using atomic-resolution scanning probe microscopy. *Nature Chem.* **2**, 821–825 (2010).
- [40] Mohn, F., Gross, L., Moll, N. & Meyer, G. Imaging the charge distribution within a single molecule. *Nature Nanotechnol.* **7**, 227–231 (2012).
- [41] Gross, L. *et al.* High-resolution molecular orbital imaging using a *p*-wave STM tip. *Phys. Rev. Lett.* **107**, 086101 (2011).
- [42] Welker, J. & Giessibl, F. J. Revealing the Angular Symmetry of Chemical Bonds by Atomic Force Microscopy. *Science* **336**, 444–449 (2012).
- [43] Moll, N., Gross, L., Mohn, F., Curioni, A. & Meyer, G. The mechanisms underlying the enhanced resolution of atomic force microscopy with functionalized tips. *New J. Phys.* **12**, 125020 (2010).

- [44] Giessibl, F. J. [High-speed force sensor for force microscopy and profilometry utilizing a quartz tuning fork](#). *Appl. Phys. Lett.* **73**, 3956–3958 (1998).
- [45] Binnig, G., Rohrer, H., Gerber, C. & Weibel, E. [Surface studies by scanning tunneling microscopy](#). *Phys. Rev. Lett.* **49**, 57–61 (1982).
- [46] Meyer, G. & Amer, N. M. [Optical-beam-deflection atomic force microscopy: The NaCl\(001\) surface](#). *Appl. Phys. Lett.* **56**, 2100–2101 (1990).
- [47] Binnig, G., Gerber, C., Stoll, E., Albrecht, T. & Quate, C. [Atomic resolution with atomic force microscope](#). *Europhys. Lett.* **3**, 1281–1286 (1987).
- [48] Pethica, J. & Oliver, W. [Tip surface interactions in STM and AFM](#). *Phys. Scri.* **1987**, 61–66 (1987).
- [49] Kitamura, S. & Iwatsuki, M. [Observation of silicon surfaces using ultrahigh-vacuum noncontact atomic force microscopy](#). *Jpn. J. Appl. Phys* **35**, L668–L671 (1996).
- [50] Stern, J., Terris, B., Mamin, H. & Rugar, D. [Deposition and imaging of localized charge on insulator surfaces using a force microscope](#). *Appl. Phys. Lett.* **53**, 2717–2719 (1988).
- [51] Nonnenmacher, M., O’Boyle, M. P. & Wickramasinghe, H. K. [Kelvin probe force microscopy](#). *Appl. Phys. Lett.* **58**, 2921–2923 (1991).
- [52] Matey, J. & Blanc, J. [Scanning capacitance microscopy](#). *J. Appl. Phys.* **57**, 1437–1444 (1985).
- [53] Dürig, U., Pohl, D. & Rohner, F. [Near-field optical-scanning microscopy](#). *J. Appl. Phys.* **59**, 3318–3327 (1986).
- [54] Williams, C. & Wickramasinghe, H. [Scanning thermal profiler](#). *Appl. Phys. Lett.* **49**, 1587–1589 (1986).
- [55] Martin, Y. & Wickramasinghe, H. K. [Magnetic imaging by force microscopy with 1000 Å resolution](#). *Appl. Phys. Lett.* **50**, 1455–1457 (1987).
- [56] Wiesendanger, R., Güntherodt, H.-J., Güntherodt, G., Gambino, R. & Ruf, R. [Observation of vacuum tunneling of spin-polarized electrons with the scanning tunneling microscope](#). *Phys. Rev. Lett.* **65**, 247–250 (1990).
- [57] Gamow, G. [Zur Quantentheorie des Atomkernes](#). *Zeitschrift für Physik* **51**, 204–212 (1928).
- [58] Wu, S. W., Nazin, G. V., Chen, X., Qiu, X. H. & Ho, W. [Control of relative tunneling rates in single molecule bipolar electrontransport](#). *Phys. Rev. Lett.* **93**, 236802 (2004).

- [59] Büttiker, M. [Coherent and sequential tunneling in series barriers](#). *IBM J. Res.Dev.* **32**, 63–75 (1988).
- [60] Bardeen, J. [Tunnelling from a many-particle point of view](#). *Phys. Rev. Lett.* **6**, 57–59 (1961).
- [61] Tersoff, J. & Hamann, D. [Theory and application for the scanning tunneling microscope](#). *Phys. Rev. Lett.* **50**, 1998–2001 (1983).
- [62] Tersoff, J. & Hamann, D. R. [Theory of the scanning tunneling microscope](#). *Phys. Rev. B* **31**, 805–813 (1985).
- [63] Mohn, F. [Probing electronic and structural properties of single molecules on the atomic scale](#). Ph.D. thesis, University of Regensburg (2012).
- [64] Torbrügge, S., Schaff, O. & Rychen, J. [Application of the kolibrisensor® to combined atomic-resolution scanning tunneling microscopy and noncontact atomic-force microscopy imaging](#). *J. Vac. Sci. Technol. B* **28**, C4E12–C4E20 (2010).
- [65] Morita, S., Wiesendanger, R. & Meyer, E. [Noncontact atomic force microscopy](#), vol. 1, chapter 2 (Springer-Verlag, Heidelberg Berlin, 2002).
- [66] Giessibl, F. J. [Forces and frequency shifts in atomic-resolution dynamic-force microscopy](#). *Phys. Rev. B* **56**, 16010–16015 (1997).
- [67] Sader, J. E. & Jarvis, S. P. [Accurate formulas for interaction force and energy in frequency modulation force spectroscopy](#). *Appl. Phys. Lett.* **84**, 1801–1803 (2004).
- [68] Sader, J. E. *et al.* [Quantitative force measurements using frequency modulation atomic force microscopy-theoretical foundations](#). *Nanotechnology* **16**, S94–S101 (2005).
- [69] Israelachvili, J. N. [Intermolecular and surface forces: revised third edition](#) (Academic press, 2011).
- [70] Giessibl, F. [Theory for an electrostatic imaging mechanism allowing atomic resolution of ionic crystals by atomic force microscopy](#). *Phys. Rev. B* **45**, 13815–13818 (1992).
- [71] Kelvin, L. [Contact electricity of metals](#). *Phil. Mag.* **46**, 82–120 (1898).
- [72] Meyer, G. [A simple low-temperature ultrahigh-vacuum scanning tunneling microscope capable of atomic manipulation](#). *Rev. Sci. Instrum.* **67**, 2960–2965 (1996).
- [73] Zöphel, S. [Der Aufbau eines Tieftemperatur-Rastertunnelmikroskops und Strukturuntersuchungen auf vicinalen Kupferoberflächen](#). Ph.D. thesis, FU Berlin (2000).

- [74] Pavlíček, N. *Scanning probe methods applied to molecular electronics*. Ph.D. thesis, University of Regensburg (2013).
- [75] Giessibl, F. J. Sensor for noncontact profiling of a surface. U.S. Patent 8,393,009 B2, filed November 21, 2011, and issued March 5, 2013.
- [76] Morita, S., Wiesendanger, R. & Giessibl, F. J. *Noncontact atomic force microscopy*, vol. 2, chapter 6 (Springer-Verlag, Heidelberg Berlin, 2009).
- [77] Mohn, F., Gross, L. & Meyer, G. *Measuring the short-range force field above a single molecule with atomic resolution*. *Appl. Phys. Lett.* **99**, 053106 (2011).
- [78] Bennewitz, R. *et al.* Ultrathin films of NaCl on Cu(111): a LEED and dynamic force microscopy study. *Surf. Sci.* **438**, 289–296 (1999).
- [79] Repp, J., Meyer, G. & Rieder, K.-H. *Snell’s law for surface electrons: refraction of an electron gas imaged in real space*. *Phys. Rev. Lett.* **92**, 036803 (2004).
- [80] Mohn, F., Schuler, B., Gross, L. & Meyer, G. *Different tips for high-resolution atomic force microscopy and scanning tunneling microscopy of single molecules*. *Appl. Phys. Lett.* **102**, 073109 (2013).
- [81] Neu, B., Meyer, G. & Rieder, K.-H. *Controlled vertical and lateral manipulation of single atoms and molecules with the scanning tunneling microscope*. *Mod. Phys. Lett. B* **09**, 963–969 (1995).
- [82] Yazdani, A., Eigler, D. M. & Lang, N. D. *Off-resonance conduction through atomic wires*. *Science* **272**, 1921–1924 (1996).
- [83] Bartels, L. *et al.* *Dynamics of electron-induced manipulation of individual CO molecules on Cu(111)*. *Phys. Rev. Lett.* **80**, 2004–2007 (1998).
- [84] Temirov, R., Soubatch, S., Neucheva, O., Lassise, A. & Tautz, F. *A novel method achieving ultra-high geometrical resolution in scanning tunnelling microscopy*. *New J. Phys.* **10**, 053012 (2008).
- [85] Kichin, G., Weiss, C., Wagner, C., Tautz, F. S. & Temirov, R. *Single molecule and single atom sensors for atomic resolution imaging of chemically complex surfaces*. *J. Am. Chem. Soc.* **133**, 16847–16851 (2011).
- [86] Oyabu, N. *et al.* *Single atomic contact adhesion and dissipation in dynamic force microscopy*. *Phys. Rev. Lett.* **96**, 106101 (2006).
- [87] Enevoldsen, G. H., Glatzel, T., Christensen, M. C., Lauritsen, J. V. & Besenbacher, F. *Atomic scale Kelvin probe force microscopy studies of the surface potential variations on the TiO₂(110) surface*. *Phys. Rev. Lett.* **100**, 236104 (2008).

- [88] Repp, J. *Rastertunnelmikroskopie und -spektroskopie an Adsorbaten auf Metall und Isolatoroberflächen*. Ph.D. thesis, FU Berlin (2002).
- [89] Guo, C.-S., Van Hove, M. A., Zhang, R.-Q. & Minot, C. Prospects for resolving chemical structure by atomic force microscopy: A first-principles study. *Langmuir* **26**, 16271–16277 (2010).
- [90] Chen, C. J. *Introduction to scanning tunneling microscopy* (Oxford University Press New York, 1993), 2nd edn.
- [91] Pavliček, N., Swart, I., Niedenführ, J., Meyer, G. & Repp, J. Symmetry dependence of vibration-assisted tunneling. *Phys. Rev. Lett.* **110**, 136101 (2013).
- [92] Criado, A., Peña, D., Cobas, A. & Guitián, E. Domino Diels–Alder cycloadditions of arynes: New approach to elusive perylene derivatives. *Chem. Eur. J.* **16**, 9736–9740 (2010).
- [93] Swart, I., Sonnleitner, T., Niedenführ, J. & Repp, J. Controlled lateral manipulation of molecules on insulating films by STM. *Nano Lett.* **12**, 1070–1074 (2012).
- [94] Gross, L. *et al.* Investigating atomic contrast in atomic force microscopy and Kelvin probe force microscopy on ionic systems using functionalized tips. *Phys. Rev. B* **90**, 155455 (2014).
- [95] König, T. *et al.* Measuring the charge state of point defects on MgO/Ag(001). *J. Am. Chem. Soc.* **131**, 17544 (2009).
- [96] Leoni, T. *et al.* Controlling the charge state of a single redox molecular switch. *Phys. Rev. Lett.* **106**, 216103 (2011).
- [97] Bocquet, F., Nony, L., Loppacher, C. & Glatzel, T. Analytical approach to the local contact potential difference on (001) ionic surfaces: Implications for Kelvin probe force microscopy. *Phys. Rev. B* **78**, 035410 (2008).
- [98] Sadewasser, S. *et al.* New insights on atomic-resolution frequency-modulation Kelvin-probe force-microscopy imaging of semiconductors. *Phys. Rev. Lett.* **103**, 266103 (2009).
- [99] Yurtsever, A., Sugimoto, Y., Fukumoto, M., Abe, M. & Morita, S. Effect of tip polarity on Kelvin probe force microscopy images of thin insulator CaF₂ films on Si(111). *Appl. Phys. Lett.* **101**, 083119 (2012).
- [100] Ma, Z. M., Kou, L., Naitoh, Y., Li, Y. J. & Sugawara, Y. The stray capacitance effect in Kelvin probe force microscopy using FM, AM and heterodyne AM modes. *Nanotechnology* **24**, 225701 (2013).

- [101] Bocquet, F., Nony, L. & Loppacher, C. Polarization effects in noncontact atomic force microscopy: A key to model the tip-sample interaction above charged adatoms. *Phys. Rev. B* **83**, 035411 (2011).
- [102] Sadeghi, A. *et al.* Multiscale approach for simulations of Kelvin probe force microscopy with atomic resolution. *Phys. Rev. B* **86**, 075407 (2012).
- [103] Hoffmann, R., Kantorovich, L. N., Baratoff, A., Hug, H. J. & Güntherodt, H.-J. Sublattice identification in scanning force microscopy on alkali halide surfaces. *Phys. Rev. Lett.* **92**, 146103 (2004).
- [104] Lantz, M. A. *et al.* Site-specific force-distance characteristics on NaCl(001): Measurements versus atomistic simulations. *Phys. Rev. B* **74**, 245426 (2006).
- [105] Ruschmeier, K., Schirmeisen, A. & Hoffmann, R. Atomic-scale force-vector fields. *Phys. Rev. Lett.* **101**, 156102 (2008).
- [106] Foster, A. S., Barth, C. & Henry, C. R. Chemical identification of ions in doped NaCl by scanning force microscopy. *Phys. Rev. Lett.* **102**, 256103 (2009).
- [107] Fremy, S. *et al.* Three-dimensional dynamic force spectroscopy measurements on KBr(001): atomic deformations at small tip-sample separations. *Nanotechnology* **23**, 055401 (2012).
- [108] Hofer, W. A., Foster, A. S. & Shluger, A. L. Theories of scanning probe microscopes at the atomic scale. *Rev. Mod. Phys.* **75**, 1287–1331 (2003).
- [109] Repp, J., Meyer, G., Paavilainen, S., Olsson, F. & Persson, M. Scanning tunneling spectroscopy of Cl vacancies in NaCl films: Strong electron-phonon coupling in double-barrier tunneling junctions. *Phys. Rev. Lett.* **95**, 225503 (2005).
- [110] Teobaldi, G. *et al.* Chemical resolution at ionic crystal surfaces using dynamic atomic force microscopy with metallic tips. *Phys. Rev. Lett.* **106**, 216102 (2011).
- [111] Smoluchowski, R. Anisotropy of the electronic work function of metals. *Phys. Rev.* **60**, 661–674 (1941).
- [112] Gross, L. *et al.* Bond-order discrimination by atomic force microscopy. *Science* **337**, 1326–1329 (2012).
- [113] Pauling, L., Brockway, L. O. & Beach, J. The dependence of interatomic distance on single bond-double bond resonance. *J. Am. Chem. Soc.* **57**, 2705–2709 (1935).

- [114] Sedlar, J., Andelić, I., Gutman, I., Vukičević, D. & Graovac, A. [Vindicating the Pauling-bond-order concept](#). *Chem. Phys. Lett.* **427**, 418–420 (2006).
- [115] David, W. *et al.* [Crystal structure and bonding of ordered C₆₀](#). *Nature* **353**, 147–149 (1991).
- [116] Hedberg, K. *et al.* [Bond lengths in free molecules of buckminsterfullerene, C₆₀, from gas-phase electron diffraction](#). *Science* **254**, 410–412 (1991).
- [117] Fagan, P. J., Calabrese, J. C. & Malone, B. [The chemical nature of buckminsterfullerene \(C₆₀\) and the characterization of a platinum derivative](#). *Science* **252**, 1160–1161 (1991).
- [118] Liu, S., Lu, Y.-J., Kappes, M. M. & Ibers, J. A. [The structure of the C₆₀ molecule: X-ray crystal structure determination of a twin at 110K](#). *Science* **254**, 408–410 (1991).
- [119] Schleyer, P. v. R. [Introduction: Aromaticity](#). *Chem. Rev.* **101**, 1115–1118 (2001).
- [120] Comstock, M. J. *et al.* [Reversible photomechanical switching of individual engineered molecules at a metallic surface](#). *Phys. Rev. Lett.* **99**, 038301 (2007).
- [121] Alemani, M. *et al.* [Electric field-induced isomerization of azobenzene by stm](#). *J. Am. Chem. Soc.* **128**, 14446–14447 (2006).
- [122] Novoselov, K. S. *et al.* [Electric field effect in atomically thin carbon films](#). *Science* **306**, 666–669 (2004).
- [123] Ugeda, M. *et al.* [Point defects on graphene on metals](#). *Phys. Rev. Lett.* **107**, 116803 (2011).
- [124] Wang, H. *et al.* [Doping monolayer graphene with single atom substitutions](#). *Nano Lett.* **12**, 141–144 (2012).
- [125] Pavliček, N. *et al.* [Atomic force microscopy reveals bistable configurations of dibenzo\[a,h\]thianthrene and their interconversion pathway](#). *Phys. Rev. Lett.* **108**, 086101 (2012).
- [126] Schuler, B. *et al.* [Adsorption geometry determination of single molecules by atomic force microscopy](#). *Phys. Rev. Lett.* **111**, 106103 (2013).
- [127] Narita, S., Morikawa, T. & Shibuya, T. [Linear relationship between the bond lengths and the pauling bond orders in fullerene molecules](#). *J. Mol. Struct. (Theochem.)* **532**, 37–40 (2000).
- [128] Bühl, M. & Hirsch, A. [Spherical aromaticity of fullerenes](#). *Chem. Rev.* **101**, 1153–1184 (2001).

- [129] Larsson, J. A. *et al.* Orientation of individual C₆₀ molecules adsorbed on Cu(111): low-temperature scanning tunneling microscopy and density functional calculations. *Phys. Rev. B* **77**, 115434 (2008).
- [130] Schull, G., Dappe, Y. J., González, C., Bulou, H. & Berndt, R. Charge injection through single and double carbon bonds. *Nano Lett.* **11**, 3142–3146 (2011).
- [131] Sun, Z., Boneschanscher, M. P., Swart, I., Vanmaekelbergh, D. & Liljeroth, P. Quantitative atomic force microscopy with carbon monoxide terminated tips. *Phys. Rev. Lett.* **106**, 046104 (2011).
- [132] Weymouth, A. J., Hofmann, T. & Giessibl, F. J. Quantifying molecular stiffness and interaction with lateral force microscopy. *Science* **343**, 1120–1122 (2014).
- [133] Goddard, R., Haenel, M. W., Herndon, W. C., Krueger, C. & Zander, M. Crystallization of large planar polycyclic aromatic hydrocarbons: The molecular and crystal structures of hexabenzob[bc,ef,hi,kl,no,qr] coronene and benzo[1,2,3-bc:4,5,6-b'c'] dicoronene. *J. Am. Chem. Soc.* **117**, 30–41 (1995).
- [134] Moll, N. *et al.* Image distortions of a partially fluorinated hydrocarbon molecule in atomic force microscopy with carbon monoxide terminated tips. *Nano Lett.* **14**, 6127–6131 (2014).
- [135] Neu, M. *et al.* Image correction for atomic force microscopy images with functionalized tips. *Phys. Rev. B* **89**, 205407 (2014).
- [136] Boneschanscher, M. P., Hamalainen, S. K., Liljeroth, P. & Swart, I. Sample corrugation affects the apparent bond lengths in atomic force microscopy. *ACS Nano* **8**, 3006–3014 (2014).
- [137] Guillermet, O. *et al.* STM and AFM high resolution intramolecular imaging of a single decastarphene molecule. *Chem. Phys. Lett.* **511**, 482–485 (2011).
- [138] Oteyza, D. G. d. *et al.* Direct imaging of covalent bond structure in single-molecule chemical reactions. *Science* **340**, 1434–1437 (2013).
- [139] Zhang, J. *et al.* Real-space identification of intermolecular bonding with atomic force microscopy. *Science* **342**, 611–614 (2013).
- [140] Hapala, P. *et al.* Mechanism of high-resolution stm/afm imaging with functionalized tips. *Phys. Rev. B* **90**, 085421 (2014).
- [141] Guo, C.-S., Van Hove, M. A., Ren, X. & Zhao, Y. High-resolution model for noncontact atomic force microscopy with a flexible molecule on the tip apex. *J. Phys. Chem. C* **119**, 1483–1488 (2015).

- [142] Matsuo, D. *et al.* Fluoro-substituted phenyleneethynylenes: acetylenic n-type organic semiconductors. *Chem. Lett.* **39**, 1300–1302 (2010).
- [143] Kawai, S. *et al.* Obtaining detailed structural information about supramolecular systems on surfaces by combining high-resolution force microscopy with *ab initio* calculations. *ACS Nano* **7**, 9098–9105 (2013).
- [144] Moll, N., Gross, L., Mohn, F., Curioni, A. & Meyer, G. A simple model of molecular imaging with noncontact atomic force microscopy. *New J. Phys.* **14**, 083023 (2012).
- [145] Schneiderbauer, M., Emmrich, M., Weymouth, A. J. & Giessibl, F. J. CO tip functionalization inverts atomic force microscopy contrast via short-range electrostatic forces. *Phys. Rev. Lett.* **112**, 166102 (2014).
- [146] Schwarz, A., K hler, A., Grenz, J. & Wiesendanger, R. Detecting the dipole moment of a single carbon monoxide molecule. *Appl. Phys. Lett.* **105**, 011606 (2014).
- [147] Schuler, B. *et al.* Contrast formation in Kelvin probe force microscopy of single π -conjugated molecules. *Nano Lett.* **14**, 3342–3346 (2014).
- [148] Mistry, A. *et al.* The synthesis and STM/AFM imaging of ‘Olympicene’ benzo[cd]pyrenes. *Chem. Eur. J.* **21**, 2011–2018 (2015).
- [149] Henze, S., Bauer, O., Lee, T.-L., Sokolowski, M. & Tautz, F. Vertical bonding distances of PTCDA on Au(111) and Ag(111): Relation to the bonding type. *Surf. Sci.* **601**, 1566–1573 (2007).
- [150] Zegenhagen, J. Surface structure determination with X-ray standing waves. *Surf. Sci. Rep.* **18**, 202–271 (1993).
- [151] Woodruff, D. P. Normal incidence X-ray standing wave determination of adsorbate structures. *Prog. Surf. Sci.* **57**, 1–60 (1998).
- [152] Weiss, P. S. & Eigler, D. M. Site dependence of the apparent shape of a molecule in scanning tunneling microscope images: Benzene on Pt(111). *Phys. Rev. Lett.* **71**, 3139–3142 (1993).
- [153] Repp, J., Meyer, G., Rieder, K.-H. & Hyldgaard, P. Site determination and thermally assisted tunneling in homogenous nucleation. *Phys. Rev. Lett.* **91**, 206102 (2003).
- [154] Lagoute, J., Kanisawa, K. & F lsch, S. Manipulation and adsorption-site mapping of single pentacene molecules on Cu(111). *Phys. Rev. B* **70**, 245415 (2004).
- [155] Wegner, D. *et al.* Adsorption site determination of a molecular monolayer via inelastic tunneling. *Nano Lett.* **13**, 2346–2350 (2013).

- [156] Zhao, A. *et al.* [Controlling the Kondo effect of an adsorbed magnetic ion through its chemical bonding](#). *Science* **309**, 1542–1544 (2005).
- [157] Tkatchenko, A. *et al.* [Van der Waals interactions between organic adsorbates at organic/inorganic interfaces](#). *MRS Bull.* **35**, 435 (2010).
- [158] Ruiz, V. G., Liu, W., Zojer, E., Scheffler, M. & Tkatchenko, A. [Density-functional theory with screened van-der-Waals interactions for the modeling of hybrid inorganic-organic systems](#). *Phys. Rev. Lett.* **108**, 146103 (2012).
- [159] Tkatchenko, A. & Scheffler, M. [Accurate molecular van-der-Waals interactions from ground-state electron density and free-atom reference data](#). *Phys. Rev. Lett.* **102**, 073005 (2009).
- [160] Bürker, C. *et al.* [Exploring the bonding of large hydrocarbons on noble metals: Diindoperylene on Cu\(111\), Ag\(111\), and Au\(111\)](#). *Phys. Rev. B* **87**, 165443 (2013).
- [161] Liu, W. *et al.* [Benzene adsorbed on metals: Concerted effect of covalency and van der Waals bonding](#). *Phys. Rev. B* **86**, 245405 (2012).
- [162] Perdew, J., Burke, K. & Ernzerhof, M. [Generalized gradient approximation made simple](#). *Phys. Rev. Lett.* **77**, 3865–3868 (1996).
- [163] Koch, N. *et al.* [Adsorption-induced intramolecular dipole: correlating molecular conformation and interface electronic structure](#). *J. Am. Chem. Soc.* **130**, 7300–7304 (2008).
- [164] Liu, W., Schuler, B., Moll, N., Gross, L. & Tkatchenko, A. [Identical binding energies and workfunctions for distinct adsorption structures: Olympicones on the Cu\(111\) surface](#) (submitted).
- [165] Yildirim, H. & Kara, A. [Effect of van-der-Waals interactions on the adsorption of olympicene radical on Cu\(111\): Characteristics of weak physisorption versus strong chemisorption](#). *J. Phys. Chem. C* **117**, 2893–2902 (2013).
- [166] Aviram, A. & Ratner, M. A. [Molecular rectifiers](#). *Chem. Phys. Lett.* **29**, 277–283 (1974).
- [167] Joachim, C., Gimzewski, J. & Aviram, A. [Electronics using hybrid-molecular and mono-molecular devices](#). *Nature* **408**, 541–548 (2000).
- [168] Elbing, M. *et al.* [A single-molecule diode](#). *Proc. Natl. Acad. Sci. U.S.A.* **102**, 8815–8820 (2005).
- [169] Pfattner, R. *et al.* [Photo-induced intramolecular charge transfer in an ambipolar field-effect transistor based on a \$\pi\$ -conjugated donor-acceptor dyad](#). *J. Mater. Chem. C* **1**, 3985–3988 (2013).

- [170] Sariciftci, N. *et al.* Photoinduced electron transfer and long lived charge separation in a donor-bridge-acceptor supramolecular ‘diad’ consisting of ruthenium(II) tris(bipyridine) functionalized C₆₀. *Chem. Phys. Lett.* **247**, 510–514 (1995).
- [171] Barth, C. & Henry, C. R. Surface double layer on (001) surfaces of alkali halide crystals: A scanning force microscopy study. *Phys. Rev. Lett.* **98**, 136804 (2007).
- [172] Pawlak, R. *et al.* Local detection of nitrogen-vacancy centers in a nanodiamond monolayer. *Nano Lett.* **13**, 5803–5807 (2013).
- [173] Tao, C. *et al.* Spatial resolution of a type II heterojunction in a single bipolar molecule. *Nano Lett.* **9**, 3963–3967 (2009).
- [174] Pop, F. *et al.* Tetrathiafulvalene-benzothiadiazoles as redox-tunable donor-acceptor systems: synthesis and photophysical study. *Chem. Eur. J.* **19**, 2504–2514 (2013).
- [175] Amacher, A. *et al.* Electronic tuning effects via cyano substitution of a fused tetrathiafulvalene-benzothiadiazole dyad for ambipolar transport properties. *J. Mater. Chem. C* **4**, 2873–2878 (2014).
- [176] Hargittai, I., Brunvoll, J., Kolonits, M. & Khodorkovsky, V. Tetrathiafulvalene: gas-phase molecular structure from electron diffraction. *J. Mol. Struct.* **317**, 273–277 (1994).
- [177] Viruela, R., Viruela, P., Pou-Amérigo, R. & Ortí, E. Flexibility of TTF. A theoretical study. *Synth. Met.* **103**, 1991–1992 (1999).
- [178] Burke, S. *et al.* Determination of the local contact potential difference of PTCDA on NaCl: a comparison of techniques. *Nanotechnology* **20**, 264012 (2009).
- [179] Bader, R. F. W. *Atoms in molecules* (Wiley Online Library, 1990).
- [180] Lotze, V., Krane, N., Chen, X., Pascual, J. I. & Franke, K. J. Intramolecular dipole of merocyanine probed by local contact potential difference measurements in 3D (2014). Presented at the NC-AFM 2014.
- [181] Schuler, B. *et al.* From perylene to a 22-ring aromatic hydrocarbon in one-pot. *Angew. Chem. Int. Ed.* **53**, 9004–9006 (2014).
- [182] Novoselov, K. S. *et al.* A roadmap for graphene. *Nature* **490**, 192–200 (2012).
- [183] Allen, M. J., Tung, V. C. & Kaner, R. B. Honeycomb carbon: a review of graphene. *Chem. Rev.* **110**, 132–145 (2009).

- [184] Fujii, S. & Enoki, T. [Nanographene and graphene edges: electronic structure and nanofabrication](#). *Acc. Chem. Res.* **46**, 2202–2210 (2012).
- [185] Chen, L., Hernandez, Y., Feng, X. & Müllen, K. [From nanographene and graphene nanoribbons to graphene sheets: chemical synthesis](#). *Angew. Chem. Int. Ed.* **51**, 7640–7654 (2012).
- [186] Wu, J., Pisula, W. & Müllen, K. [Graphenes as potential material for electronics](#). *Chem. Rev.* **107**, 718–747 (2007).
- [187] Hanssen, K. Ø. *et al.* [A combined atomic force microscopy and computational approach for the structural elucidation of Breitfussin A and B: Highly modified halogenated dipeptides from *Thuiaria breitbartii*](#). *Angew. Chem. Int. Ed.* **124**, 12404–12407 (2012).
- [188] Nicolaou, K. & Snyder, S. A. [Chasing molecules that were never there: Misassigned natural products and the role of chemical synthesis in modern structure elucidation](#). *Angew. Chem. Int. Ed.* **44**, 1012–1044 (2005).
- [189] Elyashberg, M., Williams, A. J. & Blinov, K. [Structural revisions of natural products by computer-assisted structure elucidation \(case\) systems](#). *Nat. Prod. Rep.* **27**, 1296–1328 (2010).
- [190] Jaspars, M. [Computer assisted structure elucidation of natural products using two-dimensional NMR spectroscopy](#). *Nat. Prod. Rep.* **16**, 241–248 (1999).
- [191] Sirenko, B. I. (ed.). *Arctic Biodiversity Workshop*, p.49. Alaska Sea Grant College Program, Fairbanks, Alaska (K. Iken, B. Konar, 2003).
- [192] Repiskỳ, M., Komorovskỳ, S., Malkina, O. L. & Malkin, V. G. [Restricted magnetically balanced basis applied for relativistic calculations of indirect nuclear spin–spin coupling tensors in the matrix Dirac–Kohn–Sham framework](#). *Chem. Phys.* **356**, 236–242 (2009).
- [193] Komorovskỳ, S., Repiskỳ, M., Malkina, O. L. & Malkin, V. G. [Fully relativistic calculations of NMR shielding tensors using restricted magnetically balanced basis and gauge including atomic orbitals](#). *J. Chem. Phys.* **132**, 154101 (2010).
- [194] Pandey, S. K., Guttormsen, Y., Haug, B. E., Hedberg, C. & Bayer, A. [A concise total synthesis of breitbartin a and b](#). *Org. Lett.* **17**, 122–125 (2015).
- [195] Gough, M. & Rowland, S. [Characterization of unresolved complex mixtures of hydrocarbons in petroleum](#). *Nature* **344**, 648–650 (1990).
- [196] Mullins, O. C., Sheu, E. Y., Hammami, A. & Marshall, A. G. *Asphaltenes, Heavy Oils, and Petrochemicals*, vol. 1 (Springer, 2007).

- [197] Groenzin, H. & Mullins, O. C. [Asphaltene molecular size and structure](#). *J. Phys. Chem. A* **103**, 11237–11245 (1999).
- [198] Jorge Ancheyta, M. S. R., Fernando Trejo. *Asphaltenes: Chemical Transformation during Hydroprocessing of Heavy Oils* (CRC Press, 2010).
- [199] Larter, S. *et al.* [Molecular indicators of secondary oil migration distances](#). *Nature* **383**, 593–597 (1996).
- [200] Head, I. M., Jones, D. M. & Larter, S. R. [Biological activity in the deep subsurface and the origin of heavy oil](#). *Nature* **426**, 344–352 (2003).
- [201] Aitken, C. M., Jones, D. & Larter, S. [Anaerobic hydrocarbon biodegradation in deep subsurface oil reservoirs](#). *Nature* **431**, 291–294 (2004).
- [202] Sheng, J. *Modern Chemical Enhanced Oil Recovery: Theory and Practice* (Gulf Professional Publishing, 2010).
- [203] Wargadalam, V. J., Norinaga, K. & Iino, M. [Size and shape of a coal asphaltene studied by viscosity and diffusion coefficient measurements](#). *Fuel* **81**, 1403–1407 (2002).
- [204] Bergmann, U. *et al.* [Carbon K-edge X-ray raman spectroscopy supports simple, yet powerful description of aromatic hydrocarbons and asphaltenes](#). *Chem. Phys. Lett.* **369**, 184–191 (2003).
- [205] Mullins, O. C. [The modified Yen model](#). *Energy Fuels* **24**, 2179–2207 (2010).
- [206] Sabbah, H., Morrow, A. L., Pomerantz, A. E. & Zare, R. N. [Evidence for island structures as the dominant architecture of asphaltenes](#). *Energy Fuels* **25**, 1597–1604 (2011).
- [207] Karimi, A. *et al.* [Quantitative evidence for bridged structures in asphaltenes by thin film pyrolysis](#). *Energy Fuels* **25**, 3581–3589 (2011).
- [208] Mullins, O. C. [The asphaltenes](#). *Annu. Rev. Anal. Chem.* **4**, 393–418 (2011).
- [209] Schuler, B., Meyer, G., Peña, D., Mullins, O. C. & Gross, L. [Unraveling the molecular structures of asphaltenes by atomic force microscopy](#) (submitted).
- [210] Ruiz-Morales, Y. [Molecular orbital calculations and optical transitions of PAHs and asphaltenes](#). In *Asphaltenes, Heavy Oils, and Petroleomics*, 95–137 (Springer, 2007).
- [211] Mango, F. D. [The stability of hydrocarbons under the time–temperature conditions of petroleum genesis](#). *Nature* **352**, 146–148 (1991).
- [212] Pomerantz, A. E., Hammond, M. R., Morrow, A. L., Mullins, O. C. & Zare, R. N. [Two-step laser mass spectrometry of asphaltenes](#). *J. Am. Chem. Soc.* **130**, 7216–7217 (2008).

- [213] Cai, J. *et al.* [Atomically precise bottom-up fabrication of graphene nanoribbons.](#) *Nature* **466**, 470–473 (2010).
- [214] Gomes, K. K., Mar, W., Ko, W., Guinea, F. & Manoharan, H. C. [Designer Dirac fermions and topological phases in molecular graphene.](#) *Nature* **483**, 306–310 (2012).
- [215] Riss, A. *et al.* [Local electronic and chemical structure of oligo-acetylene derivatives formed through radical cyclizations at a surface.](#) *Nano Lett.* **14**, 2251–2255 (2014).
- [216] Stoermer, R. & Kahlert, B. [Über das 1- und 2-Brom-cumaron.](#) *Ber. Dtsch. Chem. Ges.* **35**, 1633–1640 (1902).
- [217] Wenk, H. H., Winkler, M. & Sander, W. [One century of aryne chemistry.](#) *Angew. Chem., Int. Ed.* **42**, 502–528 (2003).
- [218] Roberts, J. D., Simmons, H. E., Carlsmith, L. A. & Vaughan, C. W. [Rearrangement in the reaction of chlorobenzene-1-¹⁴C with potassium amide.](#) *J. Am. Chem. Soc.* **75**, 3290–3291 (1953).
- [219] Kitamura, T. [Synthetic methods for the generation and preparative application of benzyne.](#) *Aust. J. Chem.* **63**, 987–1001 (2010).
- [220] Godfrey, P. D. [Microwave spectroscopy of benzyne.](#) *Aust. J. Chem.* **63**, 1061–1065 (2010).
- [221] Radziszewski, J. G., Hess, B. A. & Zahradnik, R. [Infrared spectrum of o-benzyne: Experiment and theory.](#) *J. Am. Chem. Soc.* **114**, 52–57 (1992).
- [222] Warmuth, R. [o-benzyne: Strained alkyne or cumulene? NMR characterization in a molecular container.](#) *Angew. Chem. Int. Ed.* **36**, 1347–1350 (1997).
- [223] Jiao, H., Schleyer, P. v. R., Warmuth, R., Houk, K. N. & Beno, B. R. [Theoretical studies of the structure, aromaticity, and magnetic properties of o-benzyne.](#) *Angew. Chem. Int. Ed.* **36**, 2761–2764 (1997).
- [224] Laing, J. W. & Berry, R. S. [Normal coordinates, structure, and bonding of benzyne.](#) *J. Am. Chem. Soc.* **98**, 660–664 (1976).
- [225] Pavliček, N. *et al.* [On-surface generation and imaging of arynes by atomic force microscopy](#) (submitted).
- [226] Hämäläinen, S. K. *et al.* [Intermolecular contrast in atomic force microscopy images without intermolecular bonds.](#) *Phys. Rev. Lett.* **113**, 186102 (2014).

- [227] Johnson, K., Sauerhammer, B., Titmuss, S. & King, D. A. [Benzene adsorption on Ir\(100\) studied by low-energy electron diffraction I–V analysis: Evidence for formation of tilted benzyne.](#) *J. Chem. Phys.* **114**, 9539–9548 (2001).
- [228] Franc, G. & Gourdon, A. [Covalent networks through on-surface chemistry in ultra-high vacuum: state-of-the-art and recent developments.](#) *Phys. Chem. Chem. Phys.* **13**, 14283–14292 (2011).
- [229] Palma, C.-A. & Samorì, P. [Blueprinting macromolecular electronics.](#) *Nat. Chem.* **3**, 431–436 (2011).
- [230] Perepichka, D. F. & Rosei, F. [Extending polymer conjugation into the second dimension.](#) *Science* **323**, 216–217 (2009).
- [231] Grill, L. *et al.* [Nano-architectures by covalent assembly of molecular building blocks.](#) *Nat. Nanotechnol.* **2**, 687–691 (2007).
- [232] Sun, Q. *et al.* [On-surface formation of one-dimensional polyphenylene through bergman cyclization.](#) *J. Am. Chem. Soc.* **135**, 8448–8451 (2013).
- [233] Jones, R. R. & Bergman, R. G. [p-benzyne. generation as an intermediate in a thermal isomerization reaction and trapping evidence for the 1,4-benzenediyl structure.](#) *J. Am. Chem. Soc.* **94**, 660–661 (1972).
- [234] Kötting, C., Sander, W., Kammermeier, S. & Herges, R. [Matrix isolation of 3,4-benzocyclodeca-3,7,9-triene-1,5-diyne.](#) *Eur. J. Org. Chem.* **1998**, 799–803 (1998).
- [235] Oncel, N. [Atomic chains on surfaces.](#) *J. Phys.: Condens. Matter* **20**, 393001 (2008).
- [236] Nilius, N., Wallis, T. M. & Ho, W. [Development of one-dimensional band structure in artificial gold chains.](#) *Science* **297**, 1853–1856 (2002).
- [237] Blumenstein, C. *et al.* [Atomically controlled quantum chains hosting a Tomonaga-Luttinger liquid.](#) *Nature Phys.* **7**, 776–780 (2011).
- [238] Nadj-Perge, S. *et al.* [Observation of Majorana fermions in ferromagnetic atomic chains on a superconductor.](#) *Science* **346**, 602–607 (2014).
- [239] Crain, J. N. & Pierce, D. T. [End states in one-dimensional atom chains.](#) *Science* **307**, 703–706 (2005).
- [240] Barke, I. *et al.* [Low-dimensional electron gas at semiconductor surfaces.](#) *Solid State Commun.* **142**, 617–626 (2007).
- [241] Fölsch, S., Yang, J., Nacci, C. & Kanisawa, K. [Atom-by-atom quantum state control in adatom chains on a semiconductor.](#) *Phys. Rev. Lett.* **103**, 096104 (2009).

- [242] Wang, S., Wang, W. & Lin, N. Resolving band-structure evolution and defect-induced states of single conjugated oligomers by scanning tunneling microscopy and tight-binding calculations. *Phys. Rev. Lett.* **106**, 206803 (2011).
- [243] Repp, J., Liljeroth, P. & Meyer, G. Coherent electron-nuclear coupling in oligothiophene molecular wires. *Nature Phys.* **6**, 975–979 (2010).
- [244] Olsson, F. *et al.* Localization of the Cu(111) Surface State by Single Cu Adatoms. *Phys. Rev. Lett.* **93**, 206803 (2004).
- [245] Fölsch, S., Martínez-Blanco, J., Yang, J., Kanisawa, K. & Erwin, S. C. Quantum dots with single-atom precision. *Nat. Nanotechnol.* **9**, 505–508 (2014).
- [246] Koenraad, P. M. & Flatté, M. E. Single dopants in semiconductors. *Nature Mat.* **10**, 91–100 (2011).
- [247] Schofield, S. *et al.* Quantum engineering at the silicon surface using dangling bonds. *Nature Commun.* **4**, 1649 (2013).
- [248] Lorke, A., Kotthaus, J. & Ploog, K. Coupling of quantum dots on GaAs. *Phys. Rev. Lett.* **64**, 2559–2561 (1990).
- [249] Hameau, S. *et al.* Strong electron-phonon coupling regime in quantum dots: Evidence for everlasting resonant polarons. *Phys. Rev. Lett.* **83**, 4152–4155 (1999).
- [250] Haider, M. B. *et al.* Controlled coupling and occupation of silicon atomic quantum dots at room temperature. *Phys. Rev. Lett.* **102**, 046805 (2009).
- [251] Sun, Z., Swart, I., Delerue, C., Vanmaekelbergh, D. & Liljeroth, P. Orbital and charge-resolved polaron states in cdse dots and rods probed by scanning tunneling spectroscopy. *Phys. Rev. Lett.* **102**, 196401 (2009).
- [252] Leturcq, R. *et al.* Franck–Condon blockade in suspended carbon nanotube quantum dots. *Nature Phys.* **5**, 327–331 (2009).
- [253] Seufert, K. *et al.* Controlled interaction of surface quantum-well electronic states. *Nano Lett.* **13**, 6130–6135 (2013).
- [254] Andresen, S. E. *et al.* Charge state control and relaxation in an atomically doped silicon device. *Nano Lett.* **7**, 2000–2003 (2007).
- [255] Mujica-Martinez, C. A., Nalbach, P. & Thorwart, M. Organic π -conjugated copolymers as molecular charge qubits. *Phys. Rev. Lett.* **111**, 016802 (2013).
- [256] Lent, C. S., Tougaw, P. D., Porod, W. & Bernstein, G. H. Quantum cellular automata. *Nanotechnology* **4**, 49–57 (1993).

- [257] Nilius, N., Wallis, T. & Ho, W. [Influence of a heterogeneous \$\text{Al}_2\text{O}_3\$ surface on the electronic properties of single pd atoms.](#) *Phys. Rev. Lett.* **90**, 046808 (2003).
- [258] Nilius, N., Wallis, T., Persson, M. & Ho, W. [Distance dependence of the interaction between single atoms: Gold dimers on NiAl \(110\).](#) *Phys. Rev. Lett.* **90**, 196103 (2003).
- [259] Sonleitner, T., Swart, I., Pavlíček, N., Pöllmann, A. & Repp, J. [Molecular symmetry governs surface diffusion.](#) *Phys. Rev. Lett.* **107**, 186103 (2011).
- [260] Zielasek, V., Hildebrandt, T. & Henzler, M. [Surface color centers on epitaxial NaCl films.](#) *Phys. Rev. B* **62**, 2912–2919 (2000).
- [261] Simon, B. [The bound state of weakly coupled schrödinger operators in one and two dimensions.](#) *Ann. Phys.* **97**, 279–288 (1976).
- [262] Schuler, B. *et al.* Effect of electron–phonon interaction on the formation of one-dimensional electronic states in coupled Cl vacancies (submitted).
- [263] Miller, A. D. *et al.* [Electron solvation in two dimensions.](#) *Science* **297**, 1163–1166 (2002).
- [264] Haruta, M. [Size-and support-dependency in the catalysis of gold.](#) *Catal. Today* **36**, 153–166 (1997).
- [265] Olsson, F. E., Paavilainen, S., Persson, M., Repp, J. & Meyer, G. [Multiple charge states of Ag atoms on ultrathin NaCl films.](#) *Phys. Rev. Lett.* **98**, 176803 (2007).
- [266] Sterrer, M. *et al.* [Control of the charge state of metal atoms on thin MgO films.](#) *Phys. Rev. Lett.* **98**, 096107 (2007).
- [267] Steurer, W. *et al.* [Manipulation of the charge state of single Au atoms on insulating multilayer films.](#) *Phys. Rev. Lett.* **114**, 036801 (2015).
- [268] Sterrer, M. *et al.* [Identification of color centers on MgO\(001\) thin films with scanning tunneling microscopy.](#) *J. Phys. Chem. B* **110**, 46–49 (2006).
- [269] Steurer, W. *et al.* Influence of strain on the adsorption site of Au anions on epitaxial NaCl films (submitted).
- [270] Henzl, J., Mehlhorn, M., Gawronski, H., Rieder, K.-H. & Morgenstern, K. [Reversible cis–trans isomerization of a single azobenzene molecule.](#) *Angew. Chem. Int. Ed.* **45**, 603–606 (2006).
- [271] Choi, B.-Y. *et al.* [Conformational molecular switch of the azobenzene molecule: A scanning tunneling microscopy study.](#) *Phys. Rev. Lett.* **96**, 156106 (2006).

- [272] Wang, Y., Kröger, J., Berndt, R. & Hofer, W. A. [Pushing and pulling a sn ion through an adsorbed phthalocyanine molecule](#). *J. Am. Chem. Soc.* **131**, 3639–3643 (2009).
- [273] Sweetman, A. *et al.* [Toggling bistable atoms via mechanical switching of bond angle](#). *Phys. Rev. Lett.* **106**, 136101 (2011).
- [274] Auwärter, W. *et al.* [A surface-anchored molecular four-level conductance switch based on single proton transfer](#). *Nature Nanotechnol.* **7**, 41–46 (2012).
- [275] Uhlmann, C., Swart, I. & Repp, J. [Controlling the orbital sequence in individual Cu-phthalocyanine molecules](#). *Nano Lett.* **13**, 777–780 (2013).
- [276] Sugimoto, Y. *et al.* [Atom inlays performed at room temperature using atomic force microscopy](#). *Nat. Mater.* **4**, 156–159 (2005).
- [277] Sugimoto, Y. *et al.* [Complex patterning by vertical interchange atom manipulation using atomic force microscopy](#). *Science* **322**, 413–417 (2008).
- [278] Scivetti, I. & Persson, M. [The electrostatic interaction of an external charged system with a metal surface: a simplified density functional theory approach](#). *J. Phys.: Condens. Matter* **25**, 355006 (2013).
- [279] Scivetti, I. & Persson, M. [A simplified density functional theory method for investigating charged adsorbates on an ultrathin, insulating film supported by a metal substrate](#). *J. Phys.: Condens. Matter* **26**, 135003 (2014).
- [280] Piva, P. G. *et al.* [Field regulation of single-molecule conductivity by a charged surface atom](#). *Nature* **435**, 658–661 (2005).
- [281] Wang, Y. *et al.* [Switching single azopyridine supramolecules in ordered arrays on au\(111\)](#). *J. Am. Chem. Soc.* **132**, 1196–1197 (2010).
- [282] Schofield, S. *et al.* [Atomically precise placement of single dopants in Si](#). *Phys. Rev. Lett.* **91**, 136104 (2003).
- [283] McFarland, E. W. & Metiu, H. [Catalysis by doped oxides](#). *Chem. Rev.* **113**, 4391–4427 (2013).
- [284] Kawai, S. *et al.* [Atom manipulation on an insulating surface at room temperature](#). *Nature Commun.* **5**, 4403 (2014).
- [285] Li, Z. *et al.* [Self-doping of ultrathin insulating films by transition metal atoms](#). *Phys. Rev. Lett.* **112**, 026102 (2014).
- [286] [CPMD](#), IBM Corporation and MPI für Festkörperforschung Stuttgart, www.cpmd.org/.
- [287] Hamann, D. [Generalized norm-conserving pseudopotentials](#). *Phys. Rev. B* **40**, 2980–2987 (1989).

- [288] Troullier, N. & Martins, J. L. [Efficient pseudopotentials for plane-wave calculations](#). *Phys. Rev. B* **43**, 1993–2006 (1991).

List of Abbreviations

AFM	atomic force microscopy, atomic force microscope
AM-AFM	amplitude-modulation atomic force microscopy
Aryne	10,11-didehydronaphtho[1,2,3,4- <i>ghi</i>]perylene
CPMD	Car–Parrinello molecular dynamics
CTC	charge-transfer complex
DBA	9,10-dibromoanthracene
DBNP	dibenzonaphthoperylene
DFT	density functional theory
DINP	10,11-diiodonaphtho[1,2,3,4- <i>ghi</i>]perylene
DIP	diindenoperylene
Diradical	9,10-didehydroanthracene
Diyne	3,4-benzocyclodeca-3,7,9-triene-1,5-diyne
FFPB	4-(4-(2,3,4,5,6-pentafluorophenylethynyl)-2,3,5,6-tetrafluorophenylethynyl) phenylethynylbenzene
FM-AFM	frequency-modulation atomic force microscopy
HBC	hexabenzocoronene
HOMO	highest occupied molecular orbital
IS	interface state
Ketone	6H-benzopyrene-6-one

KPFM	Kelvin probe force microscopy
LCPD	local contact potential difference
LDOS	local density of states
LIS	localized interface-state
LUMO	lowest unoccupied molecular orbital
MS	mass spectrometry
NaCl: Au	implanted Au atom in the NaCl crystal at a Cl site
NaCl(2ML)/Cu(111)	two-monolayer thick (100)-terminated NaCl islands grown on a Cu(111) surface
NC-AFM	noncontact atomic force microscopy
NIR	negative ion resonance
NMR	nuclear magnetic resonance
NP	naphtho[1,2,3,4- <i>ghi</i>]perylene
Olympicene	6H-benzopyrene
PBE	Perdew–Burke–Ernzerhof
PAH	polyaromatic hydrocarbon
PIR	positive ion resonance
PLL	phase-locked loop
Radical	Chapter 7.3: benzopyrene; Chapter 9.1.2: 9-dehydro-10-bromoanthracene
SPM	scanning probe microscopy, scanning probe microscope
STM	scanning tunneling microscopy, scanning tunneling microscope

List of Abbreviations

STS	scanning tunneling spectroscopy
TNP	trinaphthoperylene
TTF	tetrathiafulvalene
TTF-PYZ ₍₂₎	tetrathiafulvalene-(di)pyrazine
TTF-TDZ ₍₂₎	tetrathiafulvalene-(di)thiadiazole
UHV	ultrahigh vacuum
vdW	van der Waals
VS	(Cl) vacancy state
XSW	x-ray standing wave

Contributions to this work

A substantial part of the work presented in this thesis was created in collaboration with different people: First and foremost, all members or former members of the atomic manipulation team at IBM Research – Zurich: Leo Gross, Gerhard Meyer, Niko Pavliček, Wolfram Steurer, Fabian Mohn, Shadi Fatayer, and Nikolaj Moll our “group theoretician”. Specifically, all projects in part III were discussed within the group. For this reason, the personal pronoun ‘I’ was omitted in favor of the ‘we’ in this thesis, as it was truly a joint group effort. My special appreciation goes to Leo Gross and Gerhard Meyer, who always took their time for scientific discussions and educated me with their deep expertise and offered help in case of technical problems with the setup or software. Nikolaj Moll is here also gratefully acknowledged for introducing me to DFT.

In the following it will be listed in which way different people were involved in the measurements, theoretical modeling or molecule synthesis in the various projects:

Sections 6.1 and 6.2 Measurements on the DBA molecules were performed together with Fabian Mohn and on the DINP jointly with Niko Pavliček.

Section 6.3 KPFM measurements of the Au and Cl tip were performed by Leo Gross and Fabian Mohn. Nikolaj Moll calculated the different tip models.

Chapter 7.1 Fabian Mohn measured the C₆₀ molecule. The HBC molecule was jointly measured with Leo Gross, who also evaluated the data. Nikolaj Moll provided theory support. Alejandro Criado and Diego Peña synthesized the DBNP molecule.

Section 7.2 Nikolaj Moll simulated the AFM maps and evaluated the effect of the CO tip tilting.

Chapter 7.3 Wei Liu and Alexandre Tkatchenko performed the DFT+vdW^{surf} calculations. Anish Mistry and David Fox synthesized the olympicene molecules.

Chapter 7.4 Molecules provided by Shi-Xia Liu and Silvio Decurtins.

Section 8.1 Sara Collazos and Diego Peña synthesized the TNP molecule.

Section 8.2 Molecules collected and purified by Kine Hanssen and Johan Isaksson. NMR measurements by the group of Marcel Jaspars. CASE calculations by Kirill Blinov.

Section 8.3 Samples provided by Oliver Mullins. Project proposed by Diego Peña.

Section 9.1.1 Most of the measurements were performed by Niko Pavliček. Sara Collazos and Diego Peña synthesized the DINP and NP molecules. Simulated AFM map by Nikolaj Moll.

Section 9.1.2 Simulated AFM maps and reaction energy calculations by Nikolaj Moll.

Section 9.2 Mats Persson and Sami Pavilainen developed the electron-phonon coupling model.

Section 9.3.2 Wolfram Steurer discovered the Au^+ on thick NaCl films. Ivan Scivetti and Mats Persson did the DFT calculations with the perfect conductor model.

Acknowledgments

Apart from the previous paragraph where the immediate scientific contributions of different people to the thesis are listed, I would like to take here the opportunity to thank those who have accompanied me along this journey. I would like to thank:

- First and foremost Leo Gross and Gerhard Meyer for being excellent supervisors, supportive and relaxing colleagues and creating an environment where it was always a pleasure to come to work.
- All other members of the team: Nikolaj Moll, Wolfram Steurer, Niko Pavliček, Fabian Mohn and Shadi Fatayer for all the discussions we had in the Lab, during the lunch or “zNueni” breaks, be it scientifically or personally.
- Jascha Repp for supervising my thesis and discussing the “tough” subjects and Dominique Bougeard for his willingness to co-referee this thesis.
- The magnetic rest of the Physics of Nanoscale Systems group and especially my manager Rolf Allenspach for his personal support and fostering a friendly group atmosphere.
- My Science & Technology Pre-Doc fellows for giving relief to my work-day life with entertaining discussions or ping-pong battles.
- The IBM soccer team for a great time during the training sessions, matches and the after-training-beer.
- The European Research Council for financial support within the ERC advanced grant CEMAS and EU project PAMS.
- My deep gratitude goes particularly to my parents and my girlfriend for their cordial support and motivation during my PhD and beyond.

Bruno Schuler

Personal Data

Born 26.08.1987 – Lachen, Switzerland

E-mail bruno.schuler@gmail.com

Chronology

- Since 2012 **Ph. D.**, IBM Research–Zurich,
Supervisor: Prof. Dr. Jascha Repp, University of Regensburg, Germany.
Characterizing and Identifying single Molecules by Scanning Probe Microscopy using Functionalized Tips
- 2010–2012 **MSc. ETH in Physics**, ETH Zurich.
Master thesis: “Prospects and challenges in molecular structure identification by atomic force microscopy”, IBM Research–Zurich
- 2007–2010 **BSc. ETH in Physics**, ETH Zurich.
- 2006–2007 **Military Service**, Army medical corps, Airolo.
- 2002–2006 **Matura**, Kantonsschule Ausserschwyz, Nuolen.

Articles

1. **Schuler, B.**, Fatayer, S., Mohn, F., Moll, N., Pavliček, N., Meyer, G., Peña, D., Gross, L., *Reversible Bergman cyclization by atom manipulation observed via atomic force microscopy*. (submitted).
2. **Schuler, B.**, Meyer, G., Peña, D., Mullins, O. C., Gross, L., *Unraveling the molecular structures of asphaltenes by atomic force microscopy*. (submitted).
3. **Schuler, B.**, Persson, M., Paavilainen, S., Pavliček, N., Gross, L., Meyer, G., Repp, J., *Effect of electron-phonon interaction on the formation of one-dimensional electronic states in coupled Cl vacancies*. (submitted).
4. Pavliček, N., **Schuler, B.**, Collazos, S., Moll, N., Pérez, D., Guitán, E., Meyer, G., Peña, D., Gross, L., *On-surface generation and imaging of arynes by atomic force microscopy*. (submitted).
5. Steurer, W., **Schuler, B.**, Pavliček, N., Gross, L., Scivetti, I., Persson, M., Meyer, G., *Toggling the local electric field with an embedded adatom switch*. (submitted).
6. Steurer, W., **Schuler, B.**, Pavliček, N., Repp, J., Gross, L., Scivetti, I., Persson, M., Meyer, G., *Influence of strain on the adsorption site of Au anions on epitaxial NaCl films*. (submitted).
7. Liu, W., **Schuler, B.**, Moll, N., Gross, L., Tkatchenko, A., *Identical binding energies and workfunctions for distinct adsorption structures: Olympicones on the Cu(111) surface*. (submitted).
8. Mistry, A., Moreton, B., **Schuler, B.**, Mohn, F., Meyer, G., Gross, L., Williams, A., Scott, P., Costantini, G., Fox, D. J., *The Synthesis and STM/AFM Imaging of 'Olympicene' benzo[cd]pyrenes*. Chem. Eur. J. **21**, 2011 (2015).
9. Gross, L., **Schuler, B.**, Mohn, F., Moll, N., Pavliček, N., Steurer, W., Scivetti, I., Kotsis, K., Persson, M., Meyer, G., *Investigating atomic contrast in atomic force microscopy and Kelvin probe force microscopy on ionic systems using functionalized tips*. Phys. Rev. B **90**, 155455 (2014).

10. Moll, N., **Schuler, B.**, Kawai, S., Xu, F., Peng, L., Orita, A., Otera, J., Curioni, A., Neu, M., Repp, J., *Image Distortions of a Partially Fluorinated Hydrocarbon Molecule in Atomic Force Microscopy with Carbon Monoxide Terminated Tips*. Nano Lett. **14**, 6127 (2014).
11. **Schuler, B.**, Liu, S.-X., Geng, Y., Decurtins, S., Meyer, G., Gross, L., *Contrast Formation in Kelvin Probe Force Microscopy of Single π -Conjugated Molecules*. Nano Lett. **14**, 3342 (2014).
12. **Schuler, B.**, Collazos, S., Gross, L., Meyer, G., Pérez, D., Guitián, E., Peña, D., *From Perylene to a 22-Ring Aromatic Hydrocarbon in One-Pot*. Angew. Chem. Int. Ed. **53**, 9004 (2014).
13. **Schuler, B.**, Liu, W., Tkatchenko, A., Moll, N., Meyer, G., Mistry, A., Fox, D., Gross, L., *Adsorption Geometry Determination of Single Molecules by Atomic Force Microscopy*. Phys. Rev. Lett. **111**, 106103 (2013).
14. Mohn, F., **Schuler, B.**, Gross, L., Meyer, G., *Different tips for high-resolution atomic force microscopy and scanning tunneling microscopy of single molecules*. Appl. Phys. Lett. **102**, 073109 (2013).
15. **Schuler, B.**, Mohn, F., Moll, N., Gross, L., Meyer, G., *Chemische Bindungen visualisiert*. Phys. Unsere Zeit **44**, 6 (2013).
16. Gross, L., Mohn, F., Moll, N., **Schuler, B.**, Criado, A., Guitián, E., Peña, D., Gourdon, A., Meyer, G., *Bond-Order Discrimination by Atomic Force Microscopy*. Science **337**, 1326 (2012).
17. Hanssen, K. Ø., **Schuler, B.**, Williams, A. J., Demissie, T. B., Hansen, E., Andersen, J. H., Svenson, J., Blinov, K., Repisky, M., Mohn, F., *A Combined Atomic Force Microscopy and Computational Approach for the Structural Elucidation of Breitfussin A and B: Highly Modified Halogenated Dipeptides from Thuiaria breifussi*. Angew. Chem. Int. Ed. **124**, 12404 (2012).

Book Chapters

1. Gross, L., **Schuler, B.**, Mohn, F., Moll, N., Repp, J., Meyer, G., in, "Noncontact Atomic Force Microscopy", ed. by S. Morita, R. Wiesendanger, E. Meyer (Springer, 2015), chapter Atomic Resolution on Molecules with Functionalized Tips (*in press*).
2. **Schuler, B.**, Gross, L., Jaspars, M., in, "Organic Structure Analysis", ed. by M. Jaspars (Oxford University Press New York, 2015), chapter Prospects and Challenges in Molecular Structure Identification by Atomic Force Microscopy (*in press*).

Patent

1. Gross, L., Meyer, G., **Schuler, B.**, Steurer, W., US Patent 2015/0121576 (2014).

Talks

1. **Schuler, B.**, Meyer, G., Peña, D., Mullins, O. C., Gross, L., *Molecular structure of asphaltenes by atomic force microscopy*, presented at the International Conference on Petroleum Phase Behavior and Fouling, Playa del Carmen, Mexico (June 2015).
2. **Schuler, B.**, Persson, M., Paavilainen, S., Pavliček, N., Gross, L., Meyer, G., Repp, J., *Delocalizing small polarons in coupled Cl vacancies*, presented at the International Workshop on Atomic Scale Wires, Krakow, Poland (Sept. 2014).
3. **Schuler, B.**, Gross, L., Pavliček, N., Steurer, W., Repp, J., Meyer, G., *Low-temperature STM/AFM at the atomic scale*, presented at the Science and Technology Pre-Doc Day, IBM Research - Zurich, Switzerland (Sept. 2014).
4. **Schuler, B.**, Liu, S.-X., Geng, Y., Decurtins, S., Meyer, G., Gross, L., *Contrast formation in Kelvin Probe Force Microscopy on single molecules*, presented at the International Conference on noncontact AFM, Tsukuba, Japan (Aug. 2014).

5. **Schuler, B.**, Liu, S.-X., Geng, Y., Decurtins, S., Meyer, G., Gross, L., *Contrast formation in Kelvin Probe Force Microscopy on single molecules*, presented at the MolCHSurf IX, Bern, Switzerland (June 2014).
6. **Schuler, B.**, Liu, W., Tkatchenko, A., Moll, N., Meyer, G., Mistry, A., Fox, D., Gross, L., *Adsorption Geometry Determination of single Molecules by Atomic Force Microscopy*, presented at the International Conference on noncontact AFM, College Park, USA (Aug. 2013).
7. **Schuler, B.**, Gross, L., Mohn, F., Steurer, W., Meyer, G., *Scanning Probe Microscopy at IBM Research - Zurich*, presented at the IBM Smarter Planet Tour, TU Dresden, Germany (May 2013), Invited Talk.
8. **Schuler, B.**, Gross, L., Mohn, F., Moll, N., Meyer, G., *Molecular Structure Elucidation by Atomic Force Microscopy*, presented at the Annual Meeting of the German Physical Society, University of Regensburg, Germany (Mar. 2013).
9. **Schuler, B.**, Gross, L., Mohn, F., Moll, N., Criado, A., Guitán, E., Peña, D., Gourdon, A., Meyer, G., *Bond-order Discrimination by AFM*, presented at the ARTIST winter workshop, Les Houches, France (Jan. 2013), Invited Talk.
10. **Schuler, B.**, Gross, L., Mohn, F., Meyer, G., *Prospects and Challenges for Atomic Force Microscopy in Molecular Structure Recognition*, presented at the Annual Meeting of the Swiss Physical Society, ETH Zurich, Switzerland (June 2012).
11. **Schuler, B.**, Gross, L., Mohn, F., Meyer, G., *Prospects and Challenges in Molecular Structure Identification by Atomic Force Microscopy*, presented at the MolCHSurf VII, Bern, Switzerland (June 2012).
12. **Schuler, B.**, Gross, L., Mohn, F., Meyer, G., *Molecular Structure Identification by Atomic Force Microscopy*, presented at the Science and Technology Pre-Doc Day, IBM Research - Zurich, Switzerland (May 2012).
13. **Schuler, B.**, Gross, L., Mohn, F., Meyer, G., *Low-temperature Scanning Probe Microscopy at IBM Research - Zurich*, presented at the Kwantum Spin Up/Down, IBM Forum Brussels, Belgium (May 2012), Invited Talk.

Posters

1. **Schuler, B.**, Meyer, G., Peña, D., Mullins, O. C., Gross, L., *Unraveling the molecular structure of asphaltenes by atomic-resolution atomic force microscopy*, presented at the International Conference on Petroleum Phase Behavior and Fouling, Playa del Carmen, Mexico (June 2015).
2. **Schuler, B.**, Mohn, F., Gross, L., Moll, N., Meyer, G., *Applications of atomic-resolution imaging of single molecules with noncontact AFM*, presented at the Ralph Eichler Symposium, ETH Zurich, Switzerland (Dec. 2014).
3. **Schuler, B.**, Liu, W., Tkatchenko, A., Moll, N., Meyer, G., Mistry, A., Fox, D., Gross, L., *Adsorption Geometry Determination of single Molecules by Atomic Force Microscopy*, presented at the WE Heraeus Seminar: Interactions with the Nanoworld: Local Probes with High Time, Energy and Force Resolution, Bad Honnef, Germany (Nov. 2013).
4. **Schuler, B.**, Liu, W., Tkatchenko, A., Moll, N., Meyer, G., Mistry, A., Fox, D., Gross, L., *Adsorption Geometry Determination of single Molecules by Atomic Force Microscopy*, presented at the Swiss Nano Convention, Basel, Switzerland (May 2013).
5. **Schuler, B.**, Gross, L., Mohn, F., Moll, N., Meyer, G., *Adsorption Geometry and Chemical Structure Investigations of single Molecules with noncontact AFM using Functionalized Tips*, presented at the Annual Meeting of the German Physical Society, University of Regensburg, Germany (Mar. 2013).